A Detailed Field study of a Silicic Tuff ring in Southwest Tenerife, Deposited During Small, Phonolitic Eruptions.

BOWERS, OLIVER

A Detailed Field study of a Silicic Tuff ring in Southwest Tenerife, Deposited During Small, Phonolitic Eruptions.

Oliver Bowers

Abstract

Caldera del Rey is a small, double-crater, silicic tuff ring situated on Tenerife's southern coastline, located close to the diffuse southern rift zone. The Caldera del Rey formation displays extensive exposures of the proximal and medial deposits of the tuff ring that grew as a result of interactions between trachy-phonolitic magma and shallow groundwater within an underlying basaltic aquifer. Detailed fieldwork, laboratory work and the analysis and correlation of 39 sections through the deposits show that the eruption repeatedly alternated between eruption styles. The formation is divided into an upper and lower sequence that both initiated with a period of pumice fall from eruption plumes of almost subplinian dimensions. Over time the eruptive processes transitioned towards dominantly wetter phreatomagmatic eruptions. As the eruptions reached the climactic stage, numerous powerful, single-surge pyroclastic density currents dispersed radially up to 4 km from the vent. The depletive currents show various downcurrent lithofacies transitions that record transformations of the depositional flow-boundary zone with distance. In some cases, transformations from granular fluid-based to fully dilute currents occurred as a result of loss of granular fluid by deposition. The ash aggregation deposits share the same couplet structure seen in other ignimbrite sheets formed elsewhere on Tenerife, with variations from this occurring due to the rapid, pulsatory nature of phreatomagmatic eruptions. Tuff ring explosive activity so close to densely populated urban areas is rarely recognised, but it remains a possibility that should be factored into hazard assessments.

A detailed field study of a silicic tuff ring in southwest Tenerife, deposited during small, phonolitic eruptions.

Oliver Bowers

MScR Volcanology

Department of Earth Sciences

University of Durham

2019

Table of Contents

Table of Tables

Table of Figures

Acknowledgements

I would firstly like to thank my supervisor Dr Rich Brown for his patience, continued support and unparalleled wisdom throughout this project. I would also like to thank Alexis Schwartz for his help during fieldwork. A big thanks to my parents for the opportunities they provided me. Thank you to Richard and Lynda for their help in handing in the thesis. Thanks to the Jeffs for all the laughs. Finally, thank you to Kels for all her incredible support and love.

Chapter 1: Literature Review

1.1 Introduction

The literature contains numerous accounts of basaltic and trachybasaltic tuff ring forming eruptions (e.g. Waters and Fisher, 1971; Kienle et al., 1980; Yamamoto et al., 1991; Sohn, 1996). Similarly, the vast majority of documented maar-diatremes were created by eruptions with mafic and ultramafic magmas (White and Ross, 2011). However, relatively few silicic tuff ring and maar examples are recorded (e.g. Sheridan and Updike, 1975; Brooker et al., 1993; Colella and Hiscott, 1997; Brown et al., 2007; Cano-Cruz and Carrasco-Núñez, 2008; Austin-Erickson et al., 2011). Therefore, this thesis aims to provide a detailed study of a monogenetic silicic eruption.

The thesis will also focus on the transitions between wetter and drier phreatomagmatic eruptions, and the evolution in eruption dynamics, which have been previously identified in tuff rings and maars elsewhere (Lorenz, 1986; White and Ross, 2011).

1.2 Tuff Rings and Maars

Phreatomagmatism is a common eruption style in which magma is explosively fragmented due to interaction with external water, irrespective of the magma composition (Zimanowski et al., 2015). Magma typically encounters ground or surface water during its ascent.

The eruptions usually produce small monogenetic hydrovolcanoes. The morphology of these volcanoes is controlled by the dominant depositional processes (Sohn, 1996). Steep-sided tuff cones are found where tephra is predominantly deposited by fallout, with minimal lateral emplacement. Low-relief tuff rings and maars are constructed where most of the tephra is emplaced laterally (Sohn, 1996). They all consist of a crater, surrounding tephra ring and a diatreme under the crater (Lorenz, 1986; White and Ross, 2011). A full spectrum of crater diameters exists from a few tens of metres to 2-3 kilometres (Ross et al., 2017).

Diatremes are the sub-crater portions of maar-diatreme and tuff ring volcanoes. They are typically a cone-shaped body that gradually tapers downwards, composed of mostly pyroclastic rocks, surrounded by the country rock (Ross et al., 2017). Stratified pyroclastic deposits and post-eruptive sediments that usually dip inwards are commonly preserved in the upper levels of the diatreme (White, 1991). Juvenile clasts and lithic fragments are found within the pyroclastic rocks in the diatreme (Ross et al., 2017). Diatremes can have horizontal diameters of tens of metres to a few thousand metres and can extend hundreds of metres to a few thousand metres below the surface (Valentine et al., 2017). The eruptive activity is dominated by the shallowest explosions (Lorenz, 1986), with the diatreme itself acting as a heterogeneous aquifer (Valentine et al., 2017).

Tuff rings are typically composed of a wide central crater (<3 km) with low-relief crater rims (<100 m) that are built from outward-dipping ejecta that accumulates at or above the pre-existing surface (Cas and Wright, 1987) (Figure 1.1A). They are formed by explosive eruptions at or near the surface with generally shallow diatremes (Ross et al., 2017).

Maar-diatremes develop from higher levels of excavation to produce deep craters, up to 500 m deep, that are situated below the pre-existing ground surface (Lorenz, 1973; Vespermann and Schmincke, 2000) (Figure 1.1B). They are commonly characterised by deep diatremes (Ross et al., 2017) filled with pyroclastic material with a high abundance of accidental lithic fragments (Lorenz, 1986). Maar-forming eruptions have an explosive character that usually results from hydrovolcanic explosions that occur deep within aquifers (e.g. Zimanowski et al., 1991; Austin-Erickson et al., 2008; Valentine and White, 2012).

The dominant eruptive style of tuff ring- and maar-forming eruptions is typically phreatomagmatic. However, many examples have magmatic phases (White and Ross, 2011) and rapid fluctuations between wetter and drier phases are common (e.g. Ukinrek, Alaska, Self et al., 1980; Crater Hill, New Zealand, Houghton et al., 1996).

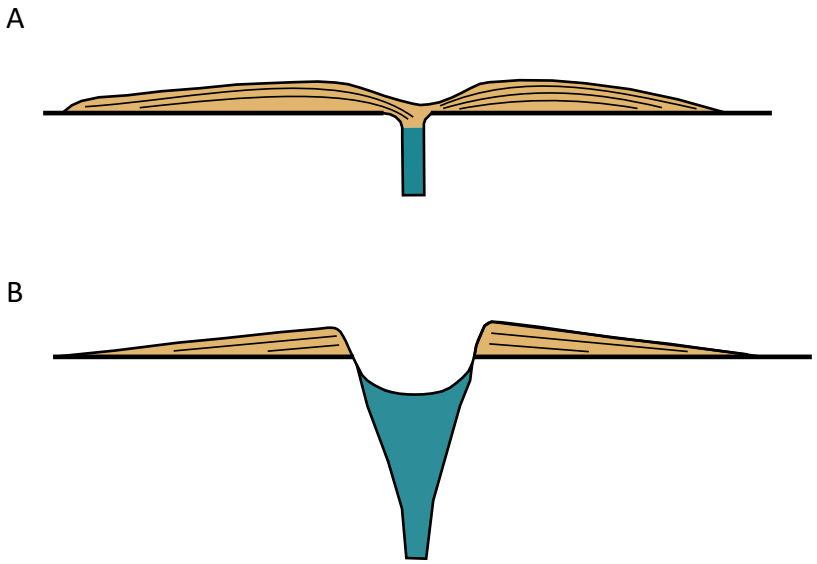

Figure 1.1 *Structure and morphology of small hydrovolcanic landforms –* ***(A)*** *Tuff rings are built above the level of the pre-existing surface.* ***(B)*** *Maar-diatremes excavate into the substrate and their crater lies below the level of the pre-existing surface. Edited from Wohletz and Sheridan (1983).*

In both tuff rings and maars, the tephra rings generally contain well-bedded deposits that formed mainly from radially dispersed low-concentration dilute pyroclastic density currents (PDCs) and fallout (Kokelaar, 1986). Granular fluid-based pyroclastic density currents are typically rarer (e.g. White 1991; White and Schmincke, 1999). The PDCs are characteristically generated from transient fountaining of the tephra that is normally ejected in upwards directed jets. These jets, which usually have heights less than 1 km, are either the result of single pulses or unsteadily sustained for only short durations. The resultant currents have runout distances of between 0.5 and 3 km (Brown et al., 2007).

Taalian eruptions are those where low-concentration pyroclastic density currents dominate and occur through an aquifer, where the supply of water is usually limited (Kokelaar, 1986). They are named after the 1965 eruptions at Taal Volcano, Philippines (see Moore et al., 1966; Moore, 1967; Waters and Fisher, 1971). In this case the eruptions are commonly powerful and may operate near maximum thermodynamic efficiency. The associated ejecta rings of Taalian eruptions normally have low profiles and are widely distributed (e.g. Wohletz and Sheridan, 1983). These density currents can travel up to 4-5 km from the vent (Moore, 1967).

Surtseyan eruptions occur through open water (Kokelaar, 1983) and therefore have relatively high water:magma ratios (Moore, 1985). They are named after the 1963-1965 submarine and emergent eruptions that formed the island of Surtsey, Iceland

(Thorarinsson, 1967). In comparison to Taalian eruptions they typically eject tephra to lower altitudes and at lower velocities, due to excess water quenching the system (Brown et al., 2007).

Stratified-tuff and lapilli-tuff lithofacies dominate in small hydrovolcanic volcanoes, with many of the deposits containing low-angle cross-bedding, dunes, ripples and planar-bedding (e.g. Sheridan and Updike 1975; Sohn and Chough, 1989; Colella and Hiscott 1997; Vasquez and Ort, 2006; Ross et al., 2011). Ash aggregates are commonly intercalated as lapilli horizons (e.g. Fisher and Waters, 1970; Buchel and Lorenz, 1993). Bed thickness typically ranges from millimetre to metre scale (Ross et al., 2017). Post-eruptive crater infill is common (White and Ross, 2011). Ejecta rings consist of tens to hundreds of beds, which suggests a pulsatory eruptive style (Ross et al., 2017).

1.2.1 Ash Aggregation

Ash aggregation is a common process in many hydrovolcanoes (e.g. McPhie, 1986; De Rita et al., 2002; Freda et al., 2005) and hydrostatic adhesion is the dominant mechanism (Mueller et al., 2016; Van Eaton et al., 2012). The aggregates can be separated into two broad categories: simple aggregates and complex aggregates. Simple aggregates typically lack structure and come in the form of particle clusters (Carey and Sigurdsson, 1982) and structureless aggregates (ash pellets – Thordarson, 2004). Alternatively, complex aggregates occur as either coated ash pellets or accretionary lapilli (Figure 1.2). Coated pellets are commonly spherical to sub-spherical and have a thin laminated fine-ash exterior and are produced as ash pellets pass through the ash-choked atmosphere elutriated above a PDC (Van Eaton et al., 2013). Accretionary lapilli contain multiple concentric layers surrounding a coarser core, with fragile ultra-fine outer rims and are produced when ash pellets descend through the turbulent levels of the PDCs (Brown et al., 2010). Ash aggregation is also an important process within co-PDC plumes (Brown et al., 2010).

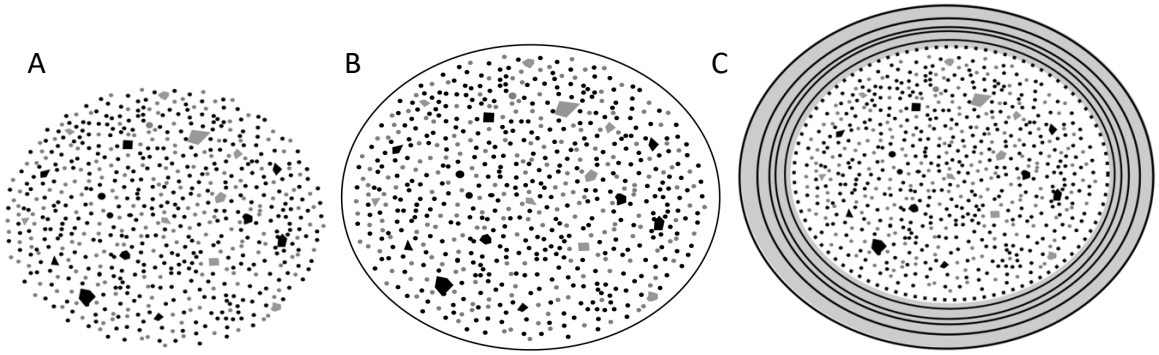

Figure 1.2 *Diagram showing the types of the ash aggregates found within this study.* ***(A)*** *Ash pellets* ***(B)*** *Coated ash pellets* ***(C)*** *Accretionary Lapilli.*

1.2.2 Silicic Tuff Rings

The similarities between felsic hydrovolcanoes and the more common ultramafic and mafic counterparts are numerous (White and Ross, 2011). The morphological features and overall structure are thought to be similar with the ejecta ring and diatreme structure comparable (Ross et al., 2017). The crater and diatreme dimensions and depths observed are generally similar to those of mafic and ultramafic compositions (White and Ross, 2011). The ejecta rings have similar thicknesses and distributions, and features such as dune bedforms and low-angle cross-bedding are common in both ultramafic/mafic and felsic examples (Ross et al., 2017). The lithofacies are also similar, with pyroclastic fall deposits and pyroclastic density current deposits common. The poorly sorted, relatively coarse, heterolithic diatreme deposits of felsic volcanoes are very similar to their ultramafic and mafic counterparts (Ross et al., 2017).

Ultramafic/mafic hydrovolcanoes often, but not always, evolve into scoria cones or lava lakes when the aquifer is exhausted or the eruptive rate increases (e.g. Lorenz, 1986; White, 1991; White and Ross, 2011). Felsic hydrovolcanoes can show an analogous evolution with late stage evolution towards lower water content phreatomagmatic eruptions, magmatic explosive eruptions and/or lava dome formation (Ross et al., 2017).

Additionally, felsic hydrovolcanoes are observed in groups (e.g., Cerro de Pasco, Peru, Baumgartner et al., 2008, 2009; Montana Tunnels, Montana, Sillitoe et al., 1985). This is also the case for many monogenetic volcanoes (e.g. Nemeth and Kereszturi, 2015). The pumice clasts originating from both ultramafic/mafic and felsic eruptions have similar

ranges in vesicularities and degassing histories, with often dense and poorly vesiculated pumice clasts (Ross and White, 2012).

Despite numerous similarities between felsic and ultramafic/mafic hydrovolcanoes, there are also important differences. Firstly, the explosive interaction of felsic magmas differs from ultramafic/mafic magmas (discussed below). Secondly, the dykes that feed felsic diatremes may be larger than those related to ultramafic/mafic diatremes (Ross et al., 2017). The wider conduits are needed for the more viscous felsic magma to ascend to the surface (Carrasco-Núñez and Ort, 2012). Thirdly, the composition of the magma can have an impact on the textures of the juvenile pyroclasts with variations in mineralogy and flow banding observed.

1.3 Magmatic and Phreatomagmatic Fragmentation

The explosive fragmentation of magma during volcanic eruptions results in the formation of pyroclasts. Explosive fragmentation can occur through two primary mechanisms. Magmatic eruptions result from prompt decompression that causes the rapid exsolution of dissolved magmatic gases (Cashman and Scheu, 2015). Moreover, phreatomagmatic eruptions initiate from the interaction of hot magma with external water sources (Zimanowski et al., 2015). Magmatic and phreatomagmatic fragmentation are not mutually exclusive mechanisms. Phases of one mechanism can occur during sustained phases of the other mechanism (e.g. Moore, 1967; Austin-Erikson et al., 2011)

1.3.1 Magmatic Fragmentation

Magma is comprised of three separate phases: gas/volatiles (e.g. H_2O, CO_2, S), a silicate melt and crystals. The behaviour and quantity of the gas phase is the dominant control on eruption style. This is because explosive eruptions are driven by the rapid expansion of the gas phase during decompression (Cashman and Scheu, 2015). Magmatic eruptions are generated when magma is allowed to rise, decompress and exsolve gas in a process called vesiculation. The vesiculation process facilitates the magma passing up the conduit (Fowler et al., 2010). It is during ascent that a gas-particle mixture is created from the fragmentation of the vesiculated magma. This accelerates up the conduit and is emitted into the atmosphere (Rust and Cashman, 2011).

1.3.2 Phreatomagmatic Fragmentation

Phreatomagmatic fragmentation is triggered by the interaction of magma with external water. The external water is rapidly heated upon contact with magma, which causes a volumetric expansion (Zimanowski et al., 2015). Thermal energy is converted into both mechanical and kinetic energy during phreatomagmatic eruptions. Phreatomagmatic eruptions typically form deposits with a fine grainsize and a greater distribution of pyroclasts. This is because increases in mechanical energy, caused by the greater eruption efficiency, leads to greater fragmentation of the magma (Zimanowski et al., 2015).

Phreatomagmatic eruptions are a type of molten fuel coolant interaction (MFCI), where the magma is the fuel and water the coolant. The highly explosive dynamics of phreatomagmatic eruptions results from the direct contact between the fuel and the coolant (Austin-Erikson et al., 2011). The viscosity of the magma, which is controlled by the magma composition, plays an important role in this mechanism. Therefore, felsic magmas are expected to interact differently compared to mafic and ultramafic magmas (Ross et al., 2017).

This mechanism has been studied in great detail for mafic melts, through both field observations (e.g. Houghton et al., 1999; Hooten and Ort, 2002) and laboratory experiments (e.g. Büttner et al., 1999, 2002; Dellino et al., 2004; Mastin, 2007). However, whilst silicic phreatomagmatism occurs (e.g. Sheridan and Updike, 1975; Heiken and Wohletz, 1987; Houghton et al., 1987; Sheridan et al., 1987), the dynamics have not been closely examined or described in detail.

MFCI occurs as a four-step process (Morrissey et al., 2000). In the case of low viscosity mafic magmas, it is generally accepted that coarse mixing is the first step, which occurs when the two liquids mingle with a thin vapour film separating them. This likely occurs through the dispersion of water or wet sediment into the magma (Zimanowski et al. 1997). After a period of seconds to minutes, this is followed by vapour film destabilisation which allows direct contact between the magma and the liquid. The two liquids hydraulically couple which results in increased heat transfer, with the melt cooling and the water heating (Zimanowski, 1998). The third stage of the process is the fine fragmentation of the magma.

This results from brittle failure of the magma due to shock waves exceeding the bulk modulus (Austin-Erikson et al., 2011). The fourth stage is very rapid expansion and explosions that last seconds to minutes (Zimanowski, 1998).

Hydrodynamic mixing efficiency, which controls the coarse mixing stage, relies on a limited viscosity contrast between the magma and the aquifer (Zimanowski and Büttner, 2002). Therefore, the MFCI processes for the interaction of water and relatively low-viscosity fluids, such as basalt (10–100 Pa s), is very well established. However, the processes of coarse mixing with a felsic magma, such as a rhyolite (100–1000 Pa s), is more difficult due to the large viscosity contrast (Zimanowski, 1998).

Laboratory experiments allow the interaction of rhyolite with water and provide evidence as to the processes occurring in a natural setting (Austin-Erikson et al., 2008). Cracking of the magma, resulting from the injection of compressed air, allowed liquid water to come into direct contact with the hot magma, encouraging rapid heat transfer (Austin-Erikson et al., 2008).

Austin-Erickson et al. (2008, 2011) suggest a potential mechanism occurring in natural settings. A felsic dyke rising in an existing diatreme at shallow depths will have highly viscous margins that fracture and heal repeatedly because of flow-related strain (Tuffen et al., 2003; Rust et al., 2004). These temporary fractures may allow the infiltration of external water, or fluidised sediment, into the felsic magma, and in turn allow phreatomagmatic explosions to occur.

1.4 Emplacement Processes

1.4.1 Pyroclastic Density Currents and the Flow-Boundary Approach

The lithofacies interpreted in this study utilise the concept of progressive aggradation (Branney and Kokelaar, 2002). According to this concept, pyroclastic density currents are variably sustained, density-stratified and contain particle and gas phases. They deposit within a ‘flow-boundary zone’ which incorporates the uppermost part of the deposit and the lowermost part of the current. The velocity and concentration profiles of the flow-boundary zones have a large control on the characteristics of the deposits. The depositional

mechanisms of the flow-boundary zone can be significantly different to the conditions higher in the current. Thus, the lithofacies reflect the spatial and temporal evolution of the lower flow-boundary.

Two types of 'end member' pyroclastic density currents are proposed that cover a broad spectrum and all transitions can occur between these. Fully dilute currents are low-concentration, density stratified, and particles are dominantly supported by the effects of turbulence of the fluid phase (dusty gas). They ordinarily produce parallel and cross-stratified layering. Alternatively, granular fluid-based currents are high-concentration and support particles via collisional momentum transfer and/or fluid escape. Turbulence is typically suppressed, and traction reduced near the lower flow-boundary zone (Branney and Kokelaar, 1997). They often produce massive and diffuse-bedded deposits.

Branney and Kokelaar (2002) proposed four intergradational 'end-member' types of flow-boundary: direct fallout-dominated, traction-dominated, granular flow-dominated and fluid escape-dominated (Figure 1.3).

Direct fallout-dominated flow-boundaries deposit clasts from suspension via fallout with negligible fluid-escape and clast-interaction interfaces and little lateral transport (Figure 1.3B). A sharp rheological contrast is present between the current and the deposit. Direct fallout can occur from umbrella clouds and from dilute pyroclastic density currents with low velocities and tractional processes. During steady fallout massive deposits can aggrade.

In traction-dominated flow-boundaries a marked step is observed at the flow boundary for both the concentration and velocity profiles where there is a sharp interface between the current and the deposit (Figure 1.3C). Clasts are supported and transported by fluid turbulence, saltation and traction. This type of flow-boundary tends to produce relatively well sorted deposits that show cross-stratifications and planar stratifications.

Granular flow-dominated flow-boundaries occur when grain interactions dictate clast support due to high concentrations and shear rates (Figure 1.3D). Hindered settling is important at these high concentrations. Under steady conditions, massive deposits gradually aggrade. Current unsteadiness and non-uniformity produce diffuse bedding and stratification.

Fluid escape-dominated flow-boundaries develop from high clast concentrations and low shear rates (Figure 1.3E). Particles are supported by the effects of escaping dusty gas which is expelled upwards as a result of deposition. There is little contrast between the uppermost part of the deposit and the lowermost part of the current. The velocity profile decreases gradually through the flow-boundary zone as the concentration gradually increases. This type of flow boundary typically produces poorly sorted, massive and loosely packed deposits.

To determine the changing behaviour of an entire current, each lithofacies must first be interpreted regarding the processes at the flow-boundary zone. Analysing the vertical and lateral changes allows one to elucidate how the flow-boundary evolved through time and space (Branney and Kokelaar, 2002).

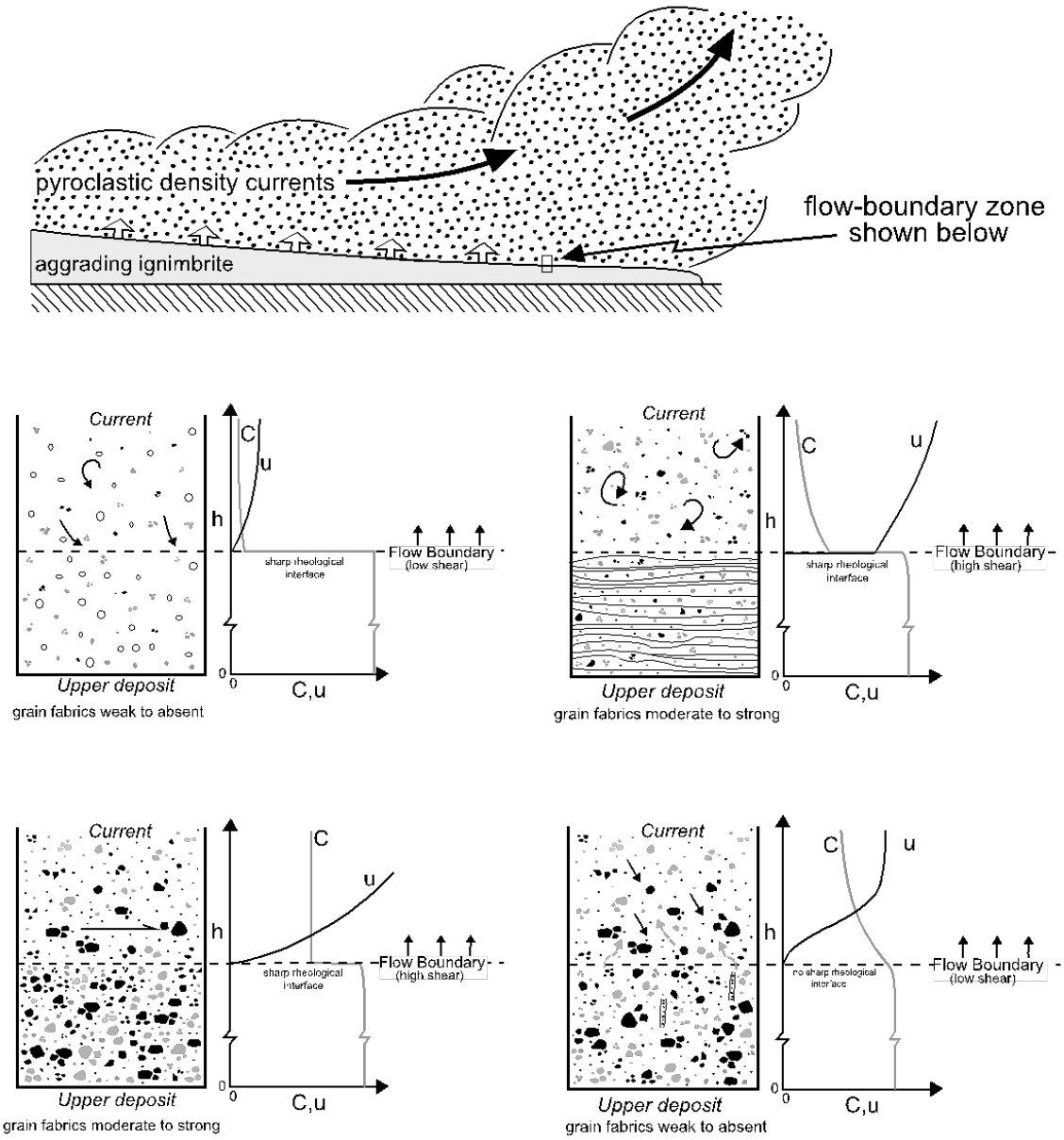

Figure 1.3 *Flow-boundary zone 'end-members' during steady conditions with schematic concentration and velocity profiles (modified from Branney and Kokelaar, 2002).* ***(A)*** *Location of the flow-boundary zone that contains the lowermost part of the current and the uppermost part of the deposit.* ***(B)*** *Direct fallout-dominated flow–boundary zone.* ***(C)*** *Traction-dominated flow-boundary zone.* ***(D)*** *Granular flow-dominated flow-boundary zone. Boundary depicts sense of shear.* ***(E)*** *Fluid escape-dominated flow-boundary zone. Complete gradations can occur between flow-boundary types.*

1.5 Geological Setting

1.5.1 Tenerife History

Tenerife is the largest island within the Canary Island archipelago, situated in the northeast of the Atlantic Ocean. The archipelago consists of seven intra-plate ocean islands which each represent different stages of their volcanic evolution (Carracedo, 1999). Tenerife, the

centremost island, is at the peak of its volcanic development (Carracedo, 1999; Carracedo et al., 1998). The unique location of the islands over old oceanic crust, close to a passive continental margin, allows the islands to remain above sea level for a significant amount of time. This encourages a long magmatic history which, in turn, supports magma differentiation in large volumes (Carracedo et al., 2007; Nelson et al., 2005). This separates the Canary Islands from other intraplate ocean islands which typically form over faster-moving and more flexible crust (Carracedo et al., 2007).

The earliest records of subaerial volcanism occurring on Tenerife are preserved in three, deeply eroded independent basaltic massifs of Miocene to Pliocene age (Ancochea et al., 1999; Ancochea et al., 1990). The Anaga massif is situated in the northeast of the islands, the Teno in the northwest and the Roques del Conde in the south (Ancochea et al., 1990). These deposits were termed the 'Old Basaltic Series' by Fuster et al. (1968). The coalescence of these three large shield volcanoes built the foundations of the island (Carracedo et al., 2007). The ages of the deposits range between 11.6 and 3.3 Ma (Ancochea et al., 1999). They formed as a result of several independent volcanic cycles that predominantly produced basalts, with smaller quantities of trachytes and phonolites (Ancochea et al., 1990).

Following the Old Basaltic Series, volcanism shifted to the centre of the island where a new composite volcano, called Las Cañadas, was constructed (Bryan et al., 1998). The deposits of Las Cañadas have partially covered the remnants of the eroded basaltic shields (Ancochea et al., 1990). The earliest eruptions, between 3.5–2 Ma, were dominantly basaltic and effusive. The later eruptions, between 2.3–0.18 Ma, generated more evolved and explosive products (Brown, 2001; Ancochea et al., 1999; Martí et al., 1994). These deposits are typically basaltic, trachybasaltic, trachytic and phonolitic (Ancochea et al., 1990) and the pyroclastic products are exceptionally exposed in the southern flanks of the island (Brown et al., 2003; Dávila Harris, 2009).

A large nested summit caldera has developed as a result of subsidence occurring during numerous large-scale ignimbrite forming eruptions (Brown et al., 2003). Following the last caldera-forming event, 200 Ka, the stratocones of Teide and Pico-Viejo have since formed (Carracedo et al., 2007). Three rift zones are found on the island that all radiate from the summit caldera. The most prominent rifts are the northeast and northwest trending rifts.

A more diffuse rift zone is found trending towards the south of the island (Dávila Harris, 2009). Sustained activity along these rift zones, coupled with growth of the central volcano, has created a bimodal distribution in the composition of the eruptive products. More differentiated magmas in the central areas have produced dominantly phonolitic and explosive products, whereas in the distal sections of the rift, basaltic eruptions typically occur (Carracedo et al., 2007).

1.6 Caldera del Rey

Caldera del Rey is a monogenetic silicic tuff ring found in southwest Tenerife, 2 km north of Playa de las Américas (Figure 1.4). The volcano is of similar age to older deposits of the Bandas del Sur group exposed on the southwest flanks of the Las Cañadas Volcano, together with other localised flank and rift eruptions. The tuff ring is situated parallel to Tenerife's diffuse southern rift zone, trending at 035°, a direction of regional importance in the Canarian Archipelago (Paradas and Fernández, 1984 and reference therein). The volcano erupted trachy-phonolitic magma (Dávila Harris, 2009; Figure 1.5). $^{40}Ar/^{39}Ar$ dating gives an age of 0.953 ± 0.01 Ma for the eruption (Dávila Harris, 2009).

The distinctive double depression found at Caldera del Rey is the result of two overlapping craters which have excavated into the basaltic substrate of the Roques del Conde, a preserved remnant of the 'Old Basaltic Series' (Fuster et al., 1968). The two-fold eruption firstly created a smaller crater in the south, followed by a larger crater in the north. The formation of the northern crater destroyed the northern part of the older southern crater and gave Caldera del Rey a distinctive pear shape appearance (Figure 1.4).

The southern and northern craters have maximum diameters of approximately 750 m and 1360 m respectively. The deposits of Caldera del Rey predominantly built the surrounding tephra-ring. However, in the northern point of the northern crater, the rim is locally made up of layered basalts of the Roques del Conde. The eroded rims of the southern and northern craters, relative to the base of the craters, reach maximum thicknesses of 40 m and 100 m respectively. The bases of the craters have since filled with alluvium, and are currently cultivated, meaning the true depth of the substrate is unknown and the diatremes are not exposed.

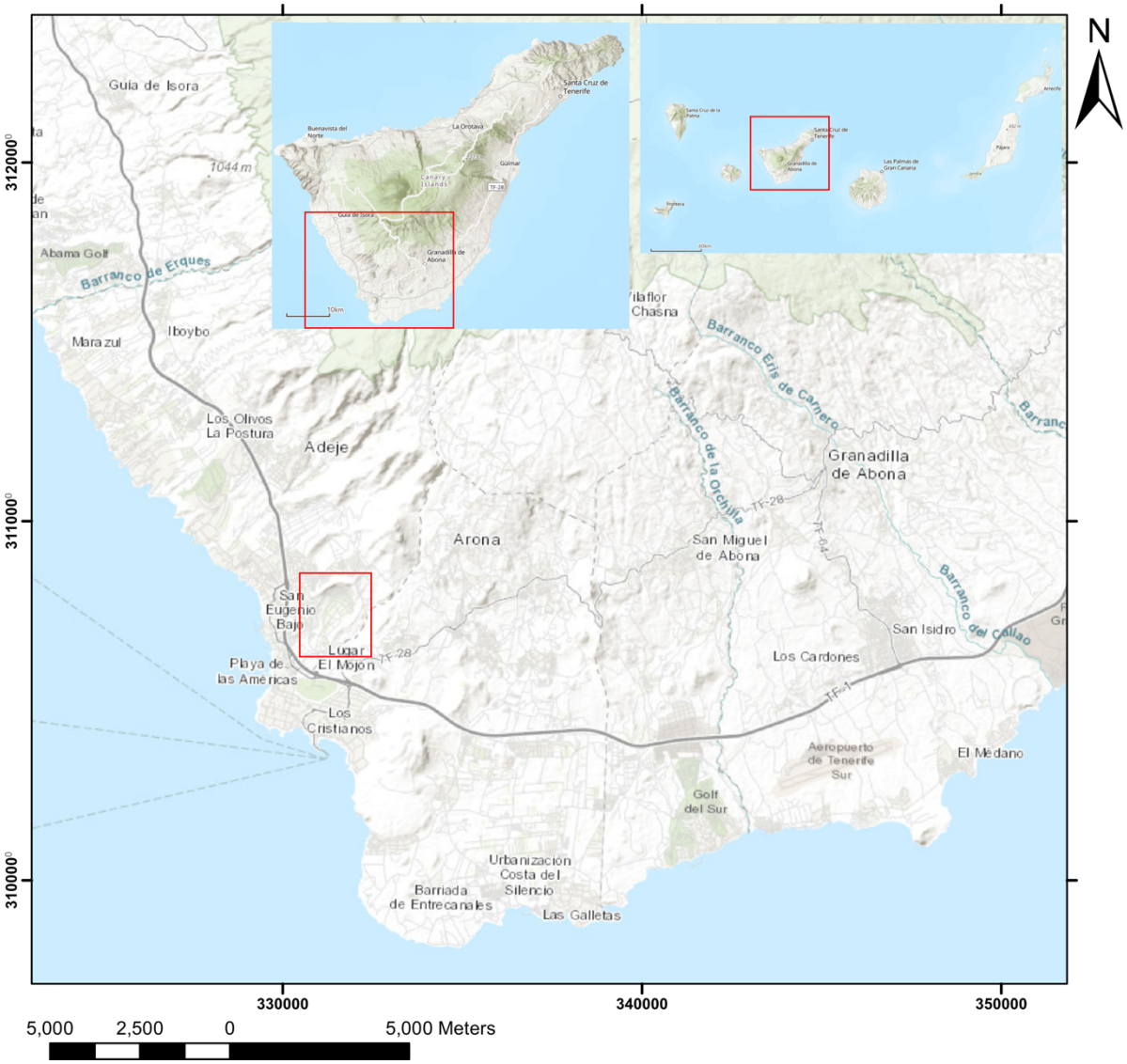

Figure 1.4 *Aerial photograph and location map of Caldera del Rey.*

The deposits that construct the slopes of Caldera del Rey generally have fairly shallow quaquaversal dips of between 5-10° that radiate away from the craters. However, the pre-existing topography of the area has a controlling factor on the dip. Where the deposits are rested up against the topographic barrier of the Roques del Conde to the north, the dips reach up to 52°. Furthermore, paleo-valleys to the west of Caldera del Rey significantly disturb the azimuth and angle of the surrounding dipping beds. The centroclinal dips are generally greater than the quaquaveral dips, reaching up to 40°. These are rarely preserved and are best appreciated in a cut section through the southern crater. Erosion and collapse of the crater, causing it to widen, is likely the reason the inward dipping layers are not preserved (Paradas and Fernández, 1984).

The deposits from Caldera del Rey cover a surface area of approximately 4.5 km^2. The deposits are predominantly found in the areas immediately surrounding the tuff ring and in localised patches. However, a thin distal deposit of ash-fallout layers, measuring 75 cm thick, is found north of Montaña Guaza, 4 km from source. The impacts of erosion, urban developments, sediment reworking and younger overlying eruptions has reduced the present-day exposure of the deposits, compared to the exposure at the time of eruption.

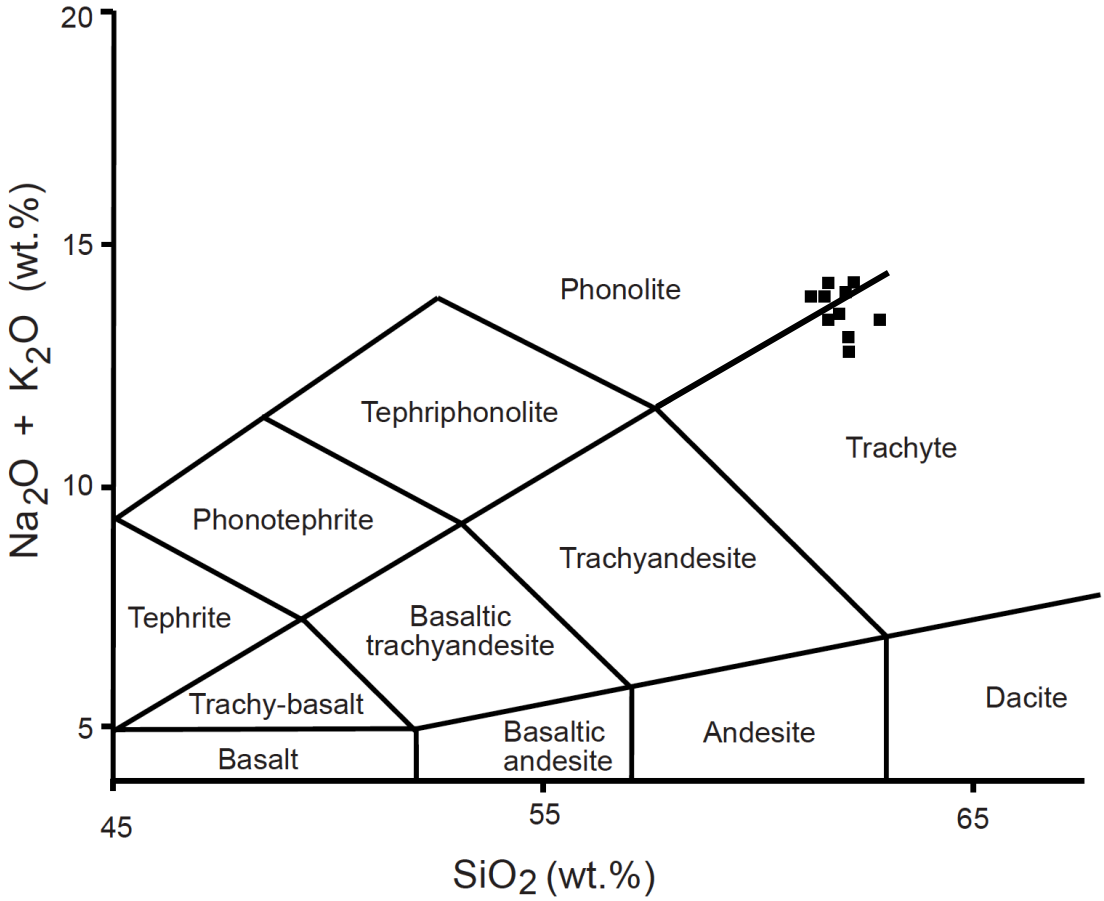

Figure 1.5 *Total-alkali vs silica (TAS) classification plot (Le Bas, 1986) for the Caldera del Rey formation. Edited from Dávila Harris (2009).*

1.6.1 Previous Work

The first recordings of Caldera del Rey and the associated deposits are present in work by Hausen (1956) and Fuster et al. (1968), which give a brief description within the wider history of Tenerife's volcanism. It is also mentioned, without detailed descriptions, as an example of maar and tuff ring volcanism (Araña and López Ruiz, 1974; Araña and Carracedo, 1979). The first detailed study of the tuff ring was undertaken by Paradas and Fernández (1984). This was followed by brief accounts from Fúster et al. (1994), Bryan et al. (1998) and Huertas et al. (2002). However, the deposits were not placed in the correct

stratigraphic context until Dávila Harris (2009). The initial understanding was predominantly hampered by imprecise radiometric dating of the deposits (Fúster et al., 1994; Huertas et al., 2002). Additionally, the deposits were incorrectly correlated with other accretionary lapilli-bearing deposits and phonolitic pumice-fall deposits from the Las Cañadas volcano (Bryan et al., 1998).

The initial study by Paradas and Fernández (1984) placed the deposits in relative stratigraphic order with the surrounding deposits of Montaña del Mojon and Montaña Guaza. It was Fúster et al. (1994) who labelled the deposits on the southwest flanks of the Las Cañadas volcano as the 'Cañadas Formation', which included the Caldera del Rey deposits within the 'Adeje-type ignimbrites'. A K/Ar age of 1.54 ± 0.28 Ma, calculated from feldspar concentrates taken from ignimbrites, was proposed (Fúster et al., 1994).

Later work by Bryan et al. (1998) described two different deposits, found around Aldea Blanca, thought to have originated from separate Caldera del Rey eruptions. The older deposits, the 'Caldera del Rey pumice members', consisted of two pale grey phonolitic, accretionary lapilli-rich, pumice-fall deposits (CRP-1 and CRP-2), with a collective thickness of 4.3 m. The younger of the deposits, the 'Caldera del Rey ignimbrite member', was described as a 10 m thick, massive, cream coloured, pumice-rich ignimbrite that is exposed north of Moñtana Guaza. The deposits were believed to be younger than the 0.569 Ma Granadilla member, but older than the 0.316 Ma Poris member (Bryan et al., 1998) and placed within Cycle 3 of Bryan et al. (1998).

However, the dates suggested by Bryan et al. (1998) contrasted with those proposed by Huertas et al. (2002) which gave a plateau age of 1.13 ± 0.04 Ma, using $^{40}Ar/^{39}Ar$ from an anorthoclase crystal taken from an ignimbrite deposit. The deposits were placed within the 'Las Américas Phase'. The age proposed is constrained by field relationships that place the deposits stratigraphically lower than the neighbouring 0.88 Ma Las Américas ignimbrite (Huertas et al., 2002). The deposits also correlate with phreatomagmatic deposits overlying the Adeje ignimbrites and are believed to be related to PH2 (Huertas et al., 2002), not PH1, as first proposed by Fúster et al. (1994).

The interpretation of the 'Caldera del Rey ignimbrite member' in the area surrounding Aldea Blanca, as suggested by Bryan et al. (1998), contains two main issues. Firstly, the

pyroclastic surge deposits lie approximately 10 km east of Caldera del Rey, over rugged terrain. Secondly, the deposits described by Bryan et al. (1998) could not correlate to the deposits of Huertas et al. (2002) as proven by field relationships from neighbouring younger deposits (Huertas et al., 2002). Brown et al. (2003) re-designated the deposits as part of the Poris Formation. However, Dávila Harris (2009) later determined them to belong to the Tosca formation.

Similarly, the 'Caldera del Rey pumice members' of Bryan et al. (1998), which were first described by Paradas and Fernández (1984), were inferred to originate from Caldera del Rey. However, isopach and isopleth data, produced for the first time by Brown et al. (2003), indicate that the deposits have a source within the Las Canadas Caldera, dispersed on a south-southwest axis. The name 'Caldera del Rey pumice members' was dropped and replaced by the 'Aldea Blanca pumice fall deposits' (Brown et al., 2003).

The most recent recordings of the Caldera del Rey deposits were produced by Dávila Harris (2009). A new age of 0.953 ± 0.01 Ma is presented and is well constrained by the younger, neighbouring Montaña Guaza phonolite dome, dated at 0.926 ± 0.02 Ma (Carracedo et al., 2007). For the first time the succession was sub-divided into 6 stratigraphic divisions, varying from member CR-A to CR-F.

1.7 Thesis Research Aims

This project has the following research aims and objectives: (a) to confirm and, where necessary, develop a new detailed stratigraphic framework; (b) to describe and interpret the eruptive history of each of the eruption members, subunits and flow-units; (c) to produce a detailed geological map on a member scale; (d) to uncover the depositional processes for each pyroclastic density current eruption using a progressive aggradation model.

Chapter 2: Methodology

2.1 Fieldwork

The aim of this project was to understand the eruptive and emplacement processes of the pyroclastic lithofacies that were produced during the Caldera del Rey eruption in southwest Tenerife. This was achieved by characterising and interpreting the lithofacies through detailed fieldwork. In proximal areas the exposure is generally excellent with outcrops continuing over 100s metres. However, in distal areas the outcrop exposure is limited due to urbanisation and burial from younger deposits. This restricts understanding of the dispersion and eruptive volumes of the Caldera del Rey eruption in these areas.

This study is the product of 7 weeks of fieldwork in Tenerife over two field seasons between October 2018 and May 2019. The conclusions drawn in this thesis are primarily from field observations. Field data was recorded through detailed lithological descriptions, geological mapping and centimetre scale sedimentary logging. The lateral and vertical facies variations observed within the various members were primarily deciphered in the field by multiple detailed logs and photographs.

2.1.1 Acquisition of Field Data

A total of 39 sections were logged, equivalent to over 275 m, primarily through road cuts and barrancos in the areas surrounding Caldera del Rey. The logging of sections involved the recording of data, measuring thicknesses, photographing and sampling where appropriate. 72 localities of interest were recorded. At these localities, sections were logged, sketches drawn, and descriptions recorded. The grid references used within the text are given in metres and refer to UTM grid zone 28, northern hemisphere. Aerial photographs were used for aids during mapping. In total, 1380 field photos were taken over both field seasons, some of which are included as figures within this study.

2.1.2 Sampling

A total of 15 rock samples and 500 pumice clasts were taken from the various members of the Caldera del Rey formation. Sampling of lithic clast populations was conducted in the field, with a minimum of 500 clasts recorded for each individual member. Ballistic projectile data was recorded throughout both field seasons. This involved recording the size of the clasts and the length and depth of the sags where present. Additionally, the clast lithology, the eruption member and the grid reference locations were recorded. 783 measurements were taken in order to determine how the size of the ballistic blocks and the sags varied with distance from the source.

2.1.3 Lithostratigraphy

The Caldera del Rey formation follows the scheme of the upper Bandas del Sur group (Bryan et al., 1998). The formation corresponds to the deposits of an entire eruption, whereas the members relate to individual phases of the eruption that vary in eruption processes. Some members have been further subdivided into units that are traceable across the region. Certain sections could be divided into flow-units that were deposited from a single current at that location. Palaeosols and sediments are recorded due to their importance in recording time gaps between periods of volcanism.

2.1.4 Lithofacies

During this study, a lithofacies approach was utilised to describe and interpret the pyroclastic deposits from Caldera del Rey. Facies analysis is a technique that has been used by geologists previously and is discussed in more detail by Anderton (1985) and Reading (1996). Facies studies on volcanic rocks have been previously discussed by Suthren (1985) and Cas and Wright (1987). Facies are defined as a body of rock that can be characterised by certain features including colour, grainsize, internal structure, geometry, texture and composition (Anderton, 1985). Individual lithofacies are used to objectively describe a rock unit that has a particular depositional process, or a combination of processes (Reading, 1978).

The lithofacies defined in this study are described using non-genetic terminology and reflect the structure, grainsize and geometry of the deposits found in the field. Through detailed logging in the field, multiple lithofacies have been defined. This allows units within members to be divided into lithofacies, depicted as lithofacies codes (following Branney and Kokelaar, 2002; see Table 2.1). Detailed interpretations of the emplacement process were achieved by defining commonly occurring lithofacies and the relationships between different lithofacies.

2.1.5 Terminology

The term 'pyroclastic' is used to describe tephra that has been fragmented by explosive volcanism and subsequently deposited by primary pyroclastic processes. This includes sedimentation by pyroclastic density currents, ash fall and ballistic emplacement.

Code	Lithofacies
mLT	Massive lapilli tuff
dbLT	Diffuse-bedded lapilli tuff
dsLT	Diffuse-stratified lapilli tuff
bLT	Bedded lapilli tuff
sLT	Stratified lapilli tuff
xsLT	Cross-stratified lapilli tuff
xsT	Cross-stratified tuff/ash
mT	Massive tuff/ash
mTacc	Massive tuff with accretionary lapilli
mTpel	Massive tuff with pellets
//sT	Parallel-stratified tuff/ash
mL	Massive Lapilli
bL	Bedded Lapilli

Abbreviation	Meaning
T	Tuff/ash
LT	Lapilli tuff/lapilli ash
L	Lapilli
l	Lithic-rich
m	Massive
s	Stratified
//s	Parallel-stratified
b	Bedded
xs	Cross-stratified
p	Pumice-rich
acc	Accretionary lapilli
pel	Pellets

Table 2.1 *Summarised codes and abbreviations for the non-genetic lithofacies used in this study (modified from Branney and Kokelaar, 2002).*

2.2 Laboratory Work

2.2.1 Pumice Density and Vesicularity

The densities of pumice clasts were measured by using a water immersion technique first developed by Houghton and Wilson (1989). The densities were converted to vesicularities which provided information regarding the relative timing of fragmentation and the role of external water during explosive eruptions.

This method applies Archimedes' principle to determine the densities of the pumice clasts. The pumice clasts were weighed in air and in water and the difference between these two values is the same as the mass of water displaced by the clasts. Assuming that the density of the water is 1 g/cm^3, this is also the volume of the water displaced, which is equivalent to the volume of the clast.

Sample Collection

A minimum of 100 pumice clasts were collected for each member. The samples were selected from the same horizons in an attempt to retrieve pumice clasts that were ejected simultaneously. The pumice clasts were sampled in proximal regions to remove the effects of aeolian fractionation of denser clasts compared to lighter clasts in pumice fall deposits (Fisher and Schmincke, 1984). Additionally, juvenile clast densities vary with size (e.g. Walker, 1981). Therefore, clasts between 32 and 16 mm were collected to provide a large range of sizes that are typically common in proximal locations.

Sample Preparation

Firstly, the samples were sieved through 32 mm and 16 mm sieves to ensure the pumice clasts were within the acquired size fraction. 100 samples were used for each member. The pumice clasts were then washed in an ultrasonic washer to remove any excess material. The pumice clasts were reasonably clean once the beaker contained little to no residue. The samples were then dried in foil containers at 70°C in an oven for 24 hours. Following this, the pumice clasts were ranked by decreasing size and numbered from 1-100.

Sample Weighing

The samples were firstly weighed in air and recorded in a table. The pumice clasts were then wrapped in an impermeable film (parafilm). The amount of parafilm used was recorded and subtracted from the weight of the submerged clast. To ensure the pumice clasts were fully submerged, they were placed within a ballast of a known weight and the joint weight of the ballast and wrapped pumice clasts were recorded. The weight of the submerged pumice clasts was calculated by subtracting the weight of the film and the ballast. The apparatus used to measure the submerged weight is shown in Figure 2.1.

Sample Analysis

The following equation was used to calculate the density of each individual pumice clasts:

$$\rho_{BULK}=\frac{\omega_A}{\omega_{A-(\omega_W-\omega_F-\omega_B)}}$$

Where ρ_{BULK}, refers to the bulk density of the pumice clast, ω_A, Pumice clast weight in air, ω_W, Pumice clast weight in water, ω_F, the weight of the film in water, and ω_B, the weight of the ballast in water.

The vesicularity value for each clast was converted from the density value using the dense rock equivalent (DRE) density for a phonolitic composition (Seifert et al., 2013). The following equation was used:

$$Vesicularity\ (\%) = \frac{100\ (\rho_{DRE} - \rho_{BULK})}{\rho_{DRE}}$$

Where ρ_{BULK}, refers to the bulk density of the pumice clast, ρ_{DRE}, the dense rock equivalent density.

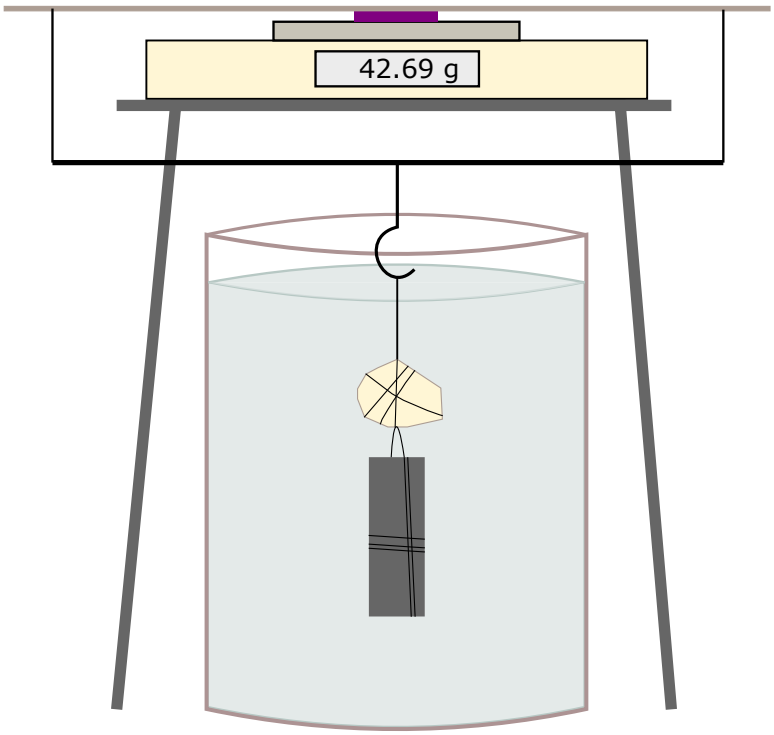

Figure 2.1 *Apparatus set-up used to weigh submerged pumice clast – Pumice clast, wrapped in parafilm, is freely suspended in the water using a ballast and metal wire of a constant and known weight and volume. The pumice clast is attached to a coat hanger that connects to a metal ruler through wire. The metal ruler is secured to the scales. Water is topped up periodically to the same level. Scales are zeroed prior to the pumice clast being hung to the coat hanger. The apparatus was tested using a cylinder of a known volume to ensure it was in correct working order.*

2.3 Data Analysis

2.3.1 Construction of Isopach and Isopleth Maps

The variations in the member thickness and clast size moving away from the vent were measured in the field through detailed logging. Isopach maps were produced from the member thickness variations for thicknesses of 15, 10, 5, 2 and 1 metre. Isopleth maps were produced from the clast size variations for lithic and pumice clasts. The average maximum size of the clast was used and isopleth contours of 5, 3, 2 and 1 cm in diameter were estimated. Ellipses were used for the shape of the contours, however, in the case of the isopleth maps where this was not possible, the contours were drawn free hand.

The isopach and isopleth maps were hand drawn, which is common practise when producing these maps (Engwell et al., 2015). However, this method can carry a large degree of uncertainty. A number of factors can control the quality of hand-drawn contours, including errors in field measurements, the quantity and spatial distribution of data points

and assumptions of deposition processes occurring (Engwell et al., 2015). Hand-drawn maps also rely on the judgement of the scientist, which can be highly variable (Klawonn et al., 2014). Issues associated with urbanisation, lack of exposure and the loss of distal deposits offshore meant that data was scarce and often clustered, which significantly hampered the production of isopach and isopleth maps. Additionally, uncertainties in the rate of thinning of the members, further complicated by aggregation processes varying with distance from source (Carey and Sigurdsson, 1982), meant it was not possible to extrapolate the thicknesses of the members. Due to the lack of preservation of distal deposits, the distal trends presented are likely a reflection of the proximal trends, which themselves are liable to large uncertainties associated with the nonlinear processes of near vent dispersal (Bonadonna and Costa, 2012; Engwell et al., 2015).

Tephra volume estimates are derived from the hand-drawn isopach maps, which is important in understanding eruption parameters. The accuracy of the volume estimates is dependent on the method used to draw the contours and the quality and quantity of field data. The empirical method used within this study is the most widely applied technique (e.g. Thorarinsson, 1954; Walker, 1980; Pyle, 1989; Bonadonna and Houghton, 2005). Whilst there is no standardised method for producing isopach maps, an intrinsically less subjective approach to creating isopach contours is to apply mathematical interpolation to the tephra thickness data (e.g. Bursik and Sieh, 2013; Engwell et al., 2015). However, the number of measurements is a major control on the uncertainty of volume estimates, regardless of the method used to produce the isopach maps. A mathematical interpolation approach would require a greater number of data points, over a greater area, than those collected, and is therefore beyond the limitations of this study.

The isopach and isopleth maps produced carry a large degree of uncertainty, and this uncertainty is carried forward when estimating the erupted tephra volumes, given that the area and thicknesses contours of the isopach maps is fundamental in this calculation.

2.3.2 Estimating Eruption Parameters

The volume of the tephra fallout deposits was calculated using the exponential thinning method of Pyle (1989). The model assumes that the thickness of the deposit decays exponentially away from the vent:

$$T = T_0 e^{-KA^{1/2}}$$

Where T, refers to the deposit thickness, T_0, initial thickness at the vent, A, area of the deposit and K, a thinning constant.

This can be simplified into a linear equation:

$$lnT = lnT_0 - KA^{1/2}$$

The thickness half-distance, b_T, is the distance over which the measured thickness from the vent decreases by half. It describes the morphology of the deposit, from cone-like to sheet-like.

$$b_T = \frac{\ln(2)}{K\sqrt{\pi}}$$

Using the parameters T_0 and b_T, the bulk tephra volume is estimated:

$$V = 13.08 T_0 b_T^2$$

The exponential thinning model uses information about the eruptive process and was preferred to simply finding the volume of the isopachs as there is a higher chance this would lead to underestimations due to the close proximity of the ocean.

Firstly, the area of each individual isopach of a given thickness was established. Following this, a plot of the square root of the calculated area($\sqrt{a}$) against the natural logarithm of the isopach thickness ($\ln[thickness]$) was produced. The square root of the isopach area is used instead of the distance from the vent. This is to average out the effects of the wind on tephra dispersal.

The value for the parameters K and $\ln(T_0)$ can be estimated from the slope and the intercept of the plot respectively. Using the estimated parameters K and $\ln(T_0)$, the values of b_T and the bulk tephra volume were determined.

The erupted mass (M) of the deposits was then calculated assuming the deposits to have a phonolitic composition (Seifert et al., 2013).

$$M = \rho V$$

Where the mass is denoted by M, deposits density, ρ, and volume, V.

The Volcanic Explosivity Index (VEI) for the eruption can be calculated using the equation:

$$VEI = Log_{10}(M) - 7$$

In order to calculate the dense rock equivalent (DRE) volume, the bulk tephra volume (V) is multiplied by the ratio of average bulk density of the deposit (ρ_D) to the volcanic rock density (ρ_R).

$$DRE\ volume = V(\rho_D{:}\rho_R)$$

To determine the average eruption rate (Q) the duration of the eruption is required. The eruption duration is calculated from the deposit thickness divided by the average deposition rate.

$$Eruption\ duration = \frac{Deposit\ thickness}{Average\ depositon\ rate}$$

The deposit thickness is measured in the field. The average deposition rate was estimated at 0.3 $m\ hr^{-1}$. This was estimated from historical eruptions. The 1973 eruption of Heimaey produced a deposition rate between 0.5 and 0.33 $m\ hr^{-1}$ for deposits 200-300 m from the vent. Similarly, the AD 79 Vesuvius eruption yielded deposition rates of 0.12-0.15 $m\ hr^{-1}$ directly downwind, 4.7 km from the source (Francis and Oppenheimer, 2004).

The deposition rate from a plume in any one place is controlled by many parameters, namely the eruption type, magma composition and viscosity, proximity to vent and wind speed. Vesuvius, a trachyte/phonolitic eruption, is closer in magma composition to Caldera del Rey than Heimaey, which represents a basaltic eruption. Therefore, it would be expected that the deposition rate would be closer to Vesuvius. However, the Heimaey example represents an eruption type closer to that of Caldera del Rey, and at a similar proximity to the vent. As a result, an eruption rate was deemed likely to be closer to Heimaey than Vesuvius. Whilst lots of consideration was given to predict an accurate eruption rate, the estimation still carries a high degree of uncertainty, which is also carried forward to the eruption rate and eruption column height.

Using the calculated eruption duration and the DRE volume, the average eruption rate is calculated.

$$Q = \frac{DRE\ volume}{Eruption\ duration}$$

The eruption column height (H_T) was estimated using the following equation from Carey and Sigurdsson (1987).

$$H_T = 1.67(Q)^{0.259}$$

2.3.3 Classifying Pyroclastic Deposits

Pyle (1989) developed a scheme which uses isopach and isopleth data to determine the style and size of an eruption. A plot of the thickness half-distance (b_T) against the half-

distance ratio ($b_c\ /b_T$) contains different fields that embody the most important types of volcanic activity and allows pyroclastic deposits to be distinguished. The fields are divided by contours of the clast size half-distance (b_C). This parameter closely relates to the height of the eruption column.

Theoretical models predict that the clast size has an exponential dependence with the distance from the vent (Pyle, 1989). The slopes of lithic and pumice clasts are similar, but not equal. This reflects the greater influence of the wind on lower-density pumice clasts compared to denser lithic fragments. Lower-density clasts have a greater maximum entrainment size and, for a given size, will be dispersed across a greater area than higher density particles.

The area of each isopleth, for both pumice and lithic clasts, was estimated and plotted on a graph of the square root of the area($\sqrt{a}$) against the natural logarithm of the isopleth clast size ($\ln [clast\ size]$).

The thinning constants, K_L and K_P, were calculated from the gradient of the slope. These values were used to estimate the clast size half-distance (b_C) for both the lithic and pumice clasts. This is a measure of the average distance from the vent at which the clast size reaches half of the initial size. The clast size half-distance is controlled by the height of the column and the intensity of the eruption.

$$b_c = \frac{\ln (2)}{K\sqrt{\pi}}$$

A plot of the thickness half-distance (b_T) against the half-distance ratio ($b_c\ /b_T$) was produced that graphically categorised the eruption based on the data from the lithic and pumice clasts. Plotting the thickness half-distance (b_T) against the half distance ratio ($b_c\ /b_T$) acts to smooth out any differences that may arise from variations in magnitude (Francis and Oppenheimer, 2004). The half-distance ratio ($b_c\ /b_T$) is a measure of the degree of fragmentation or the entrained grainsize. A deposit with a low value will likely be finer-grained (Pyle, 1989).

2.3.4 Volcanic Ballistic Projectiles

The initial velocities (V_o) for the smallest, largest and average ballistic projectile were estimated using the following equation:

$$R = \frac{V_o}{g} Sin(2\theta)$$

Where R, refers to the horizontal distance from the vent, V_o, the initial velocity at the vent, g, acceleration due to gravity, and θ, the angle of ejection. An ejection angle of 60° was assumed for the estimated velocities. Acceleration due to gravity was taken as 9.81 m s^{-2}.

The volume (V) for the different sized ballistic projectiles was calculated by assuming the blocks to be cube shaped. From this, the mass of the ballistic projectiles was estimated, assuming the density of basalt to be 2.7 g/cm^3 (Sparks et al., 1980).

$$m = \rho V$$

Where m, is the mass of the object, ρ, the density, and V, the volume.

2.3.5 Methodology Limitations

Isopach and isopleth construction was hindered by a lack of data points. Measuring the entire member thickness in the field was challenging due to the lack of exposure. Similarly, distal deposits were lost to the ocean and meant that proximal deposits were predominantly studied. This created further challenges because the high abundance of ballistic clasts meant it was difficult to determine the maximum clasts size of the umbrella cloud derived material. Whilst the proximal deposits are fairly well constrained, the actual isopach and isopleth contours for the distal deposits may significantly differ from those estimated.

Some of the eruption parameters were derived from the thinning constant (K) and the initial thickness at the vent (T_0). These two parameters were extrapolated from a graph that contained a small number of data points. This was because only a limited number of isopach and isopleth contours were drawn. Similarly, the estimated volume of the deposits is extrapolated from the areas where the deposits are thickest to where they are at their thinnest. The bulk of the volume of the deposits is found within these smaller thicknesses for which the exposure is limited. Therefore, the extrapolations agree close to source for

the greatest thicknesses. However, they may diverge considerably when extrapolated to smaller thicknesses.

The initial velocities calculated for the ballistic projectiles assumes a constant ejection angle of 60°. This is an over-simplification given that a variety of ejection angles are expected. Furthermore, in the case where blocks are influenced by an eruption plume and later decoupled, the ejection angle may vary considerably from the assumed angle. The method does not account for drag forces or any discrepancies in the elevation. Additionally, the size of the clast is not used as a parameter in calculating the velocity. Instead, the method uses the horizontal range based on the observation that the size of the ballistic projectiles decreases with distance from the vent. The assumption that the ballistic projectiles were perfect cubes is another over-simplification.

Chapter 3: Results

3.1 Caldera del Rey Formation

The Caldera del Rey formation comprises thick successions of pumice-rich fall deposits and lithic-rich ignimbrites of a trachy-phonolite composition (Dávila Harris, 2009; Paradas and Fernández, 1984). The products of the eruption are deposited around Costa Adeje and Las Américas, southwest Tenerife (Figure 3.1).

The deposits at Caldera del Rey can be divided into a lower and upper sequence, originating from the older southern crater and the younger northern crater respectively. The lower sequence comprises of two members: CDR Member A and CDR Member B. Likewise, the upper sequence is made up of CDR Members C – E. (Figure 3.2). For the first time the individual members of Caldera del Rey have been mapped at a 1:20,000 scale (Figure 3.1).

The Caldera del Rey formation was previously sub-divided into 6 stratigraphic units, Members CR A-F, by Dávila Harris (2009). However, after careful field observations it was determined that Member CR-A does not belong to the Caldera del Rey formation. Hence, the formation is now subdivided into 5 members, with the names of the members shifting so that the member formerly known as Member CR-B is now represented by CDR Member A. Additionally, the stratigraphic boundaries between the members were re-structured where necessary, and thus the members presented here may not directly relate to the deposits outlined by Dávila Harris (2009). This is particularly relevant for the boundary between CDR Members C and D (Figure 3.2).

The newly defined type locality for the Caldera del Rey formation is found directly northeast of Siam Park, within Las Américas (GR: 0330509 3106651). The section lies between 675 m and 550 m west of the centre of the southern crater. At this locality, proximal deposits of CDR Members A-D, dipping shallowly to the southwest, are clearly exposed by road cuts. The profile of the road allows one to easily walk stratigraphically up the sequence.

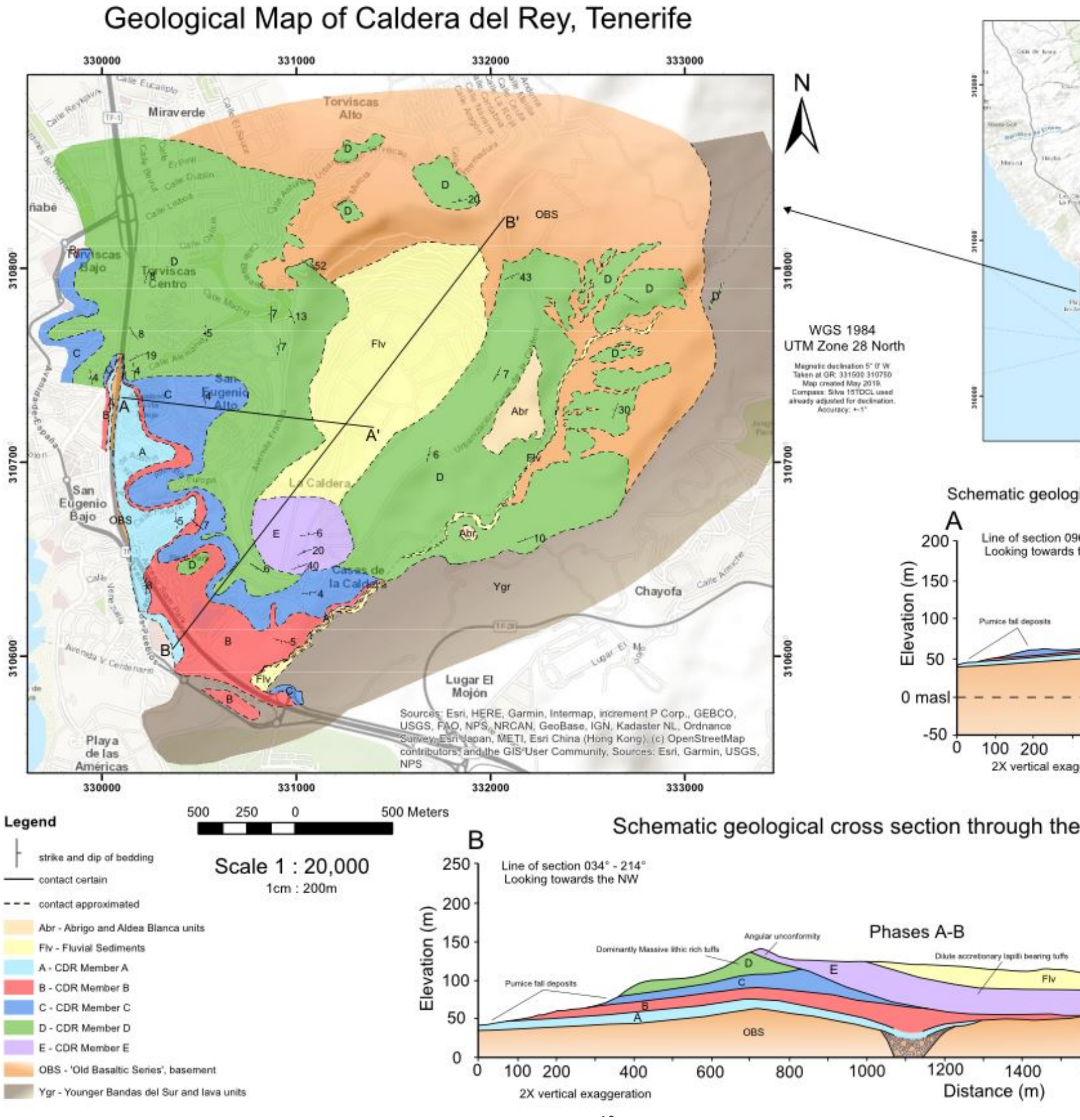

Figure 3.1 *Geological map and accompanying schematic cross-section for the Caldera del Rey formation.*

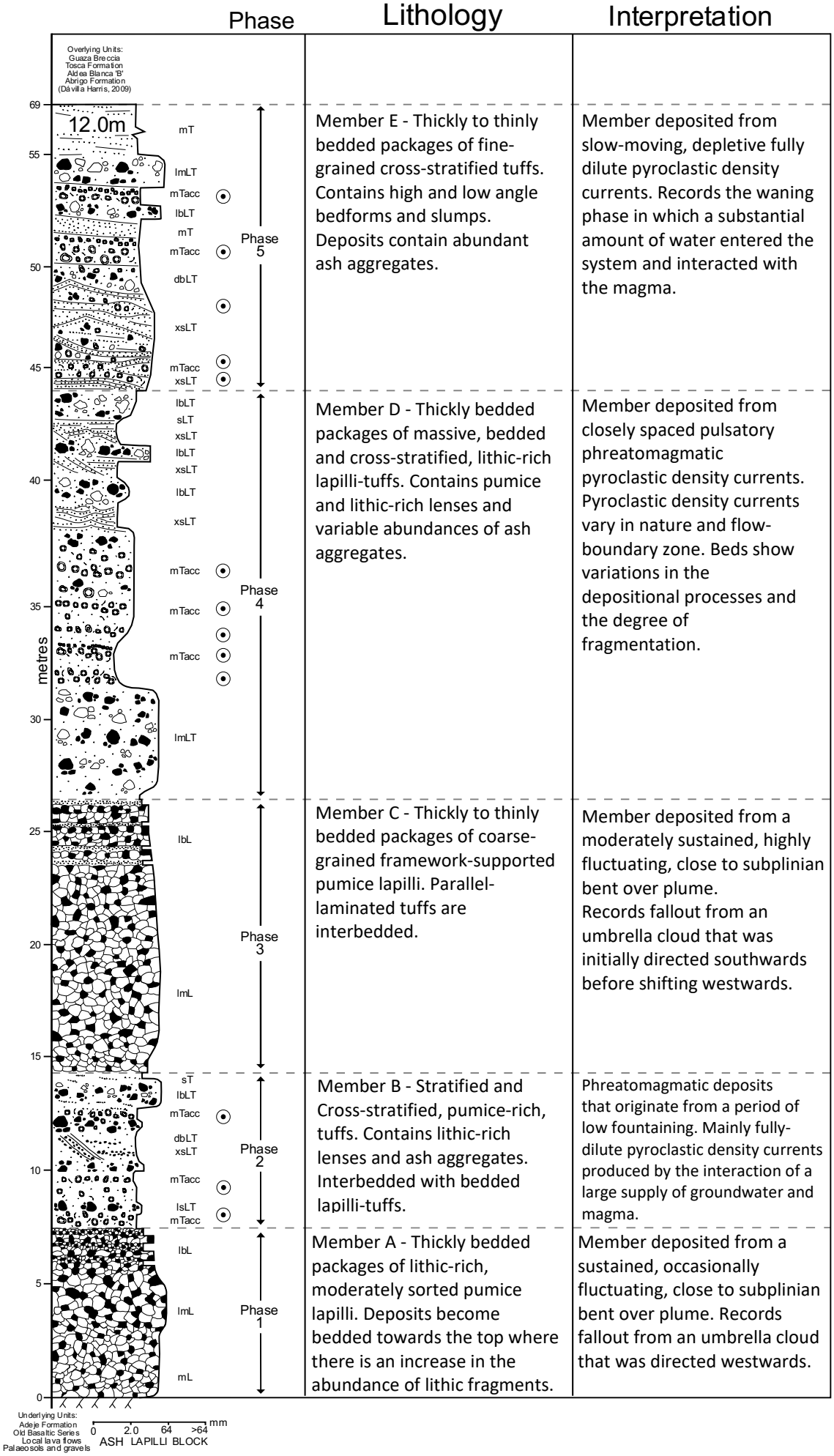

Figure 3.2 *Generalised vertical column for the Caldera del Rey formation.*

At proximal locations the formation sits upon an aphanitic basaltic lava flow that grades into a thick well-developed palaeosol, of variable thickness between 0.1 m and 1 m, containing fragments of the basaltic lava it sits on upon. This often passes into a ~0.6 m thick, massive, pale brown coloured, fine grained bed which was formerly determined to represent the start of the Caldera del Rey eruption sequence (Member CR-A of Dávila Harris, 2009). The lower 20 cm of the bed is lithic rich, containing angular clasts of basaltic lava up to 15 cm in size. The sediment has a sandy texture, similar to the fluvial sediments found within the Barranco del Rey. Locally, the upper 10 cm of the bed transitions from a pale brown colour into an orange colour, suggesting the formation of a palaeosol in places. It is for these reasons that the bed is determined to represent re-worked sediments, likely from local pyroclastic material. Similarly, the formation of a soil indicates a time-gap between the formation of this bed and the onset of the eruption.

In other proximal locations the formation rests upon the southern slopes of the Roques del Conde, made up of horizontally bedded lava flows. Towards the west of Caldera del Rey, and in the Costa Adeje region, the lower contact of the formation unconformably overlies phonolite lava and the Adeje formation. In distal locations, the formation overlies fluvial gravels north of Montaña Guaza and lies upon a local lava flow and soil where exposed by Barranco del Rey, to the northeast of Caldera del Rey.

The overlying deposits often lie unconformably due to periods of erosion and the main emplacement directions of some of the members. In proximal locations the formation is predominantly overlain by the Aldea Blanca 'B' pumice fall deposits (Brown et al., 2003) and occasionally the Abrigo formation to the east. In the distal exposures east of Caldera del Rey, the formation is overlain by a 0.926 ± 0.02 Ma (K/Ar; Carracedo et al., 2007) phonolite autobreccia originating from the Guaza dome. In other distal localities the formation is overlain by sedimentary gravels and the Tosca formation, which sits upon thinly stratified facies (Dávila Harris, 2009). Exposures to the northeast of Caldera del Rey are overlain by local lava flows from flank eruptions that have somewhat baked the sediments below.

Table 3.1 and Figure 3.3, Figure **3.4** and Figure **3.5** below outline the main lithofacies encountered in the deposits of Caldera del Rey. The lithofacies are defined from primary lithological descriptors and subdivided into lithofacies based on a combination of features that include bedding and composition. The lithofacies abbreviations follow the scheme of Branney and Kokelaar (2002).

3.1.1 Caldera del Rey Pumice Clasts

The pumice clasts of the Caldera del Rey formation are typically yellow coloured, range from coarse ash to block sized and can be rounded to angular in shape. They occur in matrix to clast supported quantities and vary in density and vesicularity. However, they maintain some features that are consistent within all of the members.

The phenocryst population comprises translucent elongated sanidine phenocrysts that are mostly 10 mm in diameter (up to 17 mm) and make up 5% of the pumice clasts. Black elongated amphibole phenocrysts are generally 5 mm (up to 10 mm) and make up 5–10% of the pumice clasts.

The pumice clasts are often altered to clays, most likely zeolites, that give the pumice clasts a powdered texture and distinct yellow colour (Hernandez et al., 1993). This predominantly affects the exteriors of the clast creating an altered rim that is typically <1 mm thick (up to 3-4 mm). Where the pumices are absent, the rim is often intact with powdered remnants of the original pumice.

Lithofacies	Description	Interpretation
Massive lapilli tuff (mLT); lithic-rich (lmLT) Figure 3.3 C, D, J	*Lithology: v*ariable proportions of lithic and pumice lapilli, matrix-supported in poorly sorted, fine to coarse-grained tuff matrix; lithic lapilli accounts for <5-50% of the lithofacies; Pumice lapilli accounts for <5-45% of the lithofacies; Lithic fragments, angular to sub-rounded, <50 cm in diameter, typically 3-20 cm, generally composed of various basaltic lavas and ignimbritic material; Pumice clasts, sub-rounded, <30mm, typically 2-10 cm *Sub-facies:* lithic-rich massive lapilli-tuff (lmLT); as mLT, 30-60% lithic lapilli *Structure:* massive to diffuse stratified; stratification plane-parallel or discontinuous defined by grainsize and lithic concentrations; non-graded *Geometry:* dm-thick, laterally continuous bodies	Rapid progressive aggradation from a high-concentration fluid escape-dominated depositional flow-boundary of a PDC, indicated by massive nature, absence of tractional structures and poor sorting (Branney and Kokelaar, 2001); diffuse bedding results from local current unsteadiness, non-uniformity and the development of granular-flow dominated flow-boundaries; lmLT as mLT, higher lithic content reflects increase in supply at source.
Diffuse-bedded lapilli tuff (dbLT); lithic-rich (ldbLT) Figure 3.3 A, B, C, K	*Lithology:* as massive lapilli tuff (mLT) *Sub-facies:* ldbLT as lmLT *Structure:* discontinuous, sub-parallel and undulating diffuse bedding defined by cm-thick lithic horizons or by thin (<2 cm) fine-grained layers. *Geometry:* individual beds persistent over 2-6 m before dying out. Lithofacies pass laterally into mLT, lmLT, ldbLT, bLT, xsLT, xsT; dm-thick packages interbedded with mLT and bLT	Similar composition and lack of internal traction structures indicate deposition processes similar to massive lapilli tuff (mLT); diffuse bedding results from current unsteadiness, perhaps in granular flow-dominated flow boundaries; discontinuous nature and lateral thickness variations reflect current non-uniformity.
Diffuse-stratified lapilli tuff (dsLT) Figure 3.3 A, B, D, F, G, I	*Lithology:* Similar to massive lapilli tuff (mLT) *Structure:* diffuse, discontinuous, parallel to sub-parallel, cm scale stratification, in sets 4 cm to 50 cm thick; defined by alternating horizons of fine-grained, lapilli-sized and lithic-rich deposits; *Geometry:* grade vertically and/or laterally in to mLT, dbLT and sLT	Rapid progressive aggradation from flow boundary zone; unsteadiness during deposition, perhaps in granular flow-dominated flow boundary zone, indicated by diffuse stratification and disordered structure.
Bedded lapilli tuff (bLT); Lithic-rich (lbLT) Figure 3.3 K	*Lithology:* similar to massive lapilli tuff (mLT) *Sub-facies:* lbLT as lmLT *Structure:* well bedded, internally massive; beds typically <30cm thick with parallel to sub-parallel boundaries; upper and lower boundaries of internal layers can be sharp *Geometry:* occur in discrete tabular beds, and in stacked beds up to ~3 m; more laterally persistent than dbLT; grade vertically and/or laterally in to mLT and dbLT	General interpretation as for mLT; stratification records local traction-sedimentation; lbLT as bLT, higher lithic content reflects increase in supply at source.

Table 3.1 *Summarised description and interpretation of lithofacies in the Caldera del Rey formation.*

Lithofacies	Description	Interpretation
Stratified lapilli tuff (sLT); Stratified tuff (sT) Figure 3.3 H, I, J	*Lithology*: alternating moderately sorted fine-grained layers and more poorly-sorted coarser-grained layers; matrix supported sub-angular to sub-rounded pumice and lithic lapilli *Sub-facies:* sT as sLT, thin sharp-bounded mm thick laminae *Structure:* parallel to sub-parallel strata <1-5 cm thick in sets 4 cm to 60 cm; very low-angle truncations are present *Geometry:* generally fairly laterally persistent over 10s–100s m; interstratified with and pass laterally and vertically into dbLT, dsLT and bLT	Tractional sedimentation from the low-concentration flow boundary zone of fully dilute PDCs; allows efficient elutriation and winnowing of low-density pumice and fine ash, indicated by well-developed stratification and sorting of layers.
Cross-stratified lapilli tuff (xsLT); Cross-stratified tuff (xsT) Figure 3.3 C, D, E, F, G	*Lithology:* similar to stratified lapilli tuff (sLT) *Sub-facies:* cross-stratified tuff (xsT) finer-grained *Structure:* low-angle cross-stratification; mm-cm thick strata; planar or concave downwards forset laminae that dip ~5-20°, occasionally truncated on their stoss-side; stoss-side laminae are sometimes preserved; bedform amplitudes up to 1 m, typically 10-30 cm; wavelengths persistent over several metres; low-angle truncations and pinch and swell structures are common; ripples present on occasions (wavelengths of m's, amplitudes of cm's) *Geometry:* cm-dm thick packages that pass vertically into dbLT, dsLT and sLT.	Deposition from traction-dominated flow-boundaries of fully dilute PDCs; current unsteadiness and passage of successive currents recorded by low-angle truncations; upcurrent-dipping strata record the plastering of moist ash against topographic irregularities.
Massive tuff (mT)	*Lithology:* fine-grained, moderately sorted, matrix-supported tuff; minor pumice and lithic lapilli (<5%) *Structure:* internally massive to diffusively stratified, lateral thickness variations common *Geometry:* mantles topography; 1–20 cm thick; pass laterally into sT, mTacc and mTpel.	Deposition from fluid escape-dominated flow boundaries of PDCs, indicated by massive nature and absence of tractional structures.
Massive accretionary lapilli tuff (mTacc) Figure 3.5 B, C	*Lithology:* similar to massive tuff (mT), contains scattered, matrix to clast-supported, multi-rimmed accretionary lapilli (up to ~1.5 cm in diameter, typically 3–5 mm); rim fragments common *Structure:* usually internally massive units; vertically and laterally variable proportions of accretionary lapilli, fragments and matrix; beds variably persistent up to ~4 km *Geometry:* occur as individual beds or in stacked sets m's in scale; passes vertically into mTpel and laterally into mT	Deposition processes as mT, accretionary lapilli horizons signify possible fallout into the current from the overlying co-ignimbrite ash clouds; fragmented aggregates likely form from the fracturing of lithified ash aggregates either on impact or during transport.

Table 3.1 *(Continued)*

Lithofacies	Description	Interpretation
Massive pellet tuff (mTpel) Figure 3.5 A, C	*Lithology:* similar to massive accretionary lapilli tuff (mTacc), contains small (1-5 mm diameter), clast-supported to framework supported coated pellets and ash pellets *Structure:* variably internally massive and normally graded; laterally variable proportions of ash aggregates and matrix; beds variably persistent up to ~ 4 km *Geometry:* can occur above mTacc, although not exclusively; passes laterally into mT	Laterally persistent horizons may reflect fallout from co-ignimbrite ash cloud; where framework supported ash pellets are found, likely represent the fall out of a co-ignimbrite ash cloud that does not pass through an underlying current.
Parallel-laminated tuff (//sT) Figure 3.4 D	*Lithology:* matrix-supported, moderately sorted, fine-grained tuff; Pumice and lithic lapilli are rare (<10 %); sometimes contains matrix-supported to clast–supported concentrations of simple ash aggregates *Structure:* parallel laminations at mm scale; Laminations occasionally undulate; beds typically 1-2 cm thick, up to 5cm; variably persistent up to 1-2 km. *Geometry:* beds often drape topography with little thickness variations, occasionally thickness variations of 1-2cm; commonly occur vertically above mL, mLT, dbLT, bLT	Where the deposits drape the topography with no thickness changes then an ashfall origin is likely; deposits may also originate from a fallout-dominated flow-boundary zone of a dilute, low-velocity rolling ash cloud (Branney and Kokelaar, 2002).
Massive lapilli (mL); bedded lapilli (bL); Pumice-rich (pmL) Figure 3.4 A, B, C, D	*Lithology:* clast-supported, pumice and lithic lapilli, moderately sorted; pumice clasts <20 cm diameter, sub angular to angular, regularly impact-fractured; varying proportions (<35%) of lithic lapilli, <15 cm *Sub-facies:* bedded lapilli (bL) as massive lapilli (mL); Pumice-rich (pmL) <90% pumice lapilli *Structure:* massive with occasional diffuse stratification and parallel stratification, defined by grainsize and lithic abundance *Geometry:* sheet form, mantles topography; laterally persistent over km scale;	Sorting, composition, mantling bedding and lateral extent suggests pumice-fall deposition; unsteadiness in the eruption column and shower bedding in reflected by grainsize stratification.

Composition: T, tuff; LT, lapilli tuff; L, lapilli; l, lithic-rich; acc, accretionary lapilli-bearing; pel, pellet-bearing; *Structure:* m, massive; db, diffuse-bedded; ds, diffuse-stratified; b, bedded; s, stratified; xs, cross-stratified; //s, parallel-laminated;
Scheme follows that devised by Branney and Kokelaar (2002).

Table 3.1 *(Continued)*

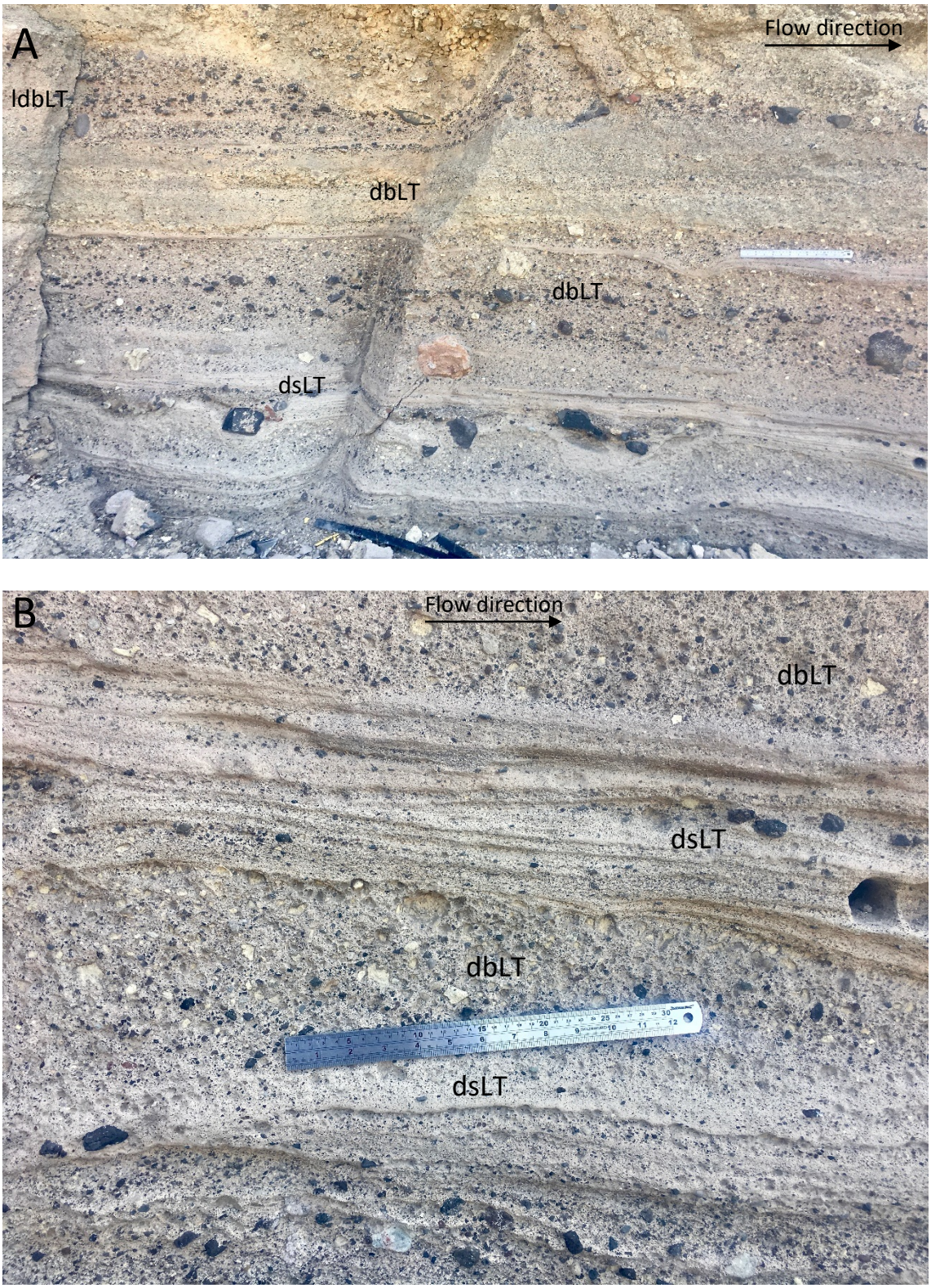

Figure 3.3 *Lithofacies of the Caldera del Rey formation with a PDC origin -* ***(A)*** *dbLT – Diffuse bedding defined by size and concentration of pumice and lithic lapilli. Beds range from trains of single clasts to units 10cm thick. The lithofacies are interbedded with dsLT that are lighter cream coloured and finer grained. Note the erosional top contact. Flow direction is from left to right. 30 cm rule is for scale. (GR: 0330736 3107765).* ***(B)*** *dsLT – Diffuse stratification as seen in Fig.3.4A. Diffuse stratification is marked by changes in grainsize and lithic content, exaggerated by the effect of denudation. Passes laterally into xsLT and vertically intodbLT. 30 cm rule is for scale.*

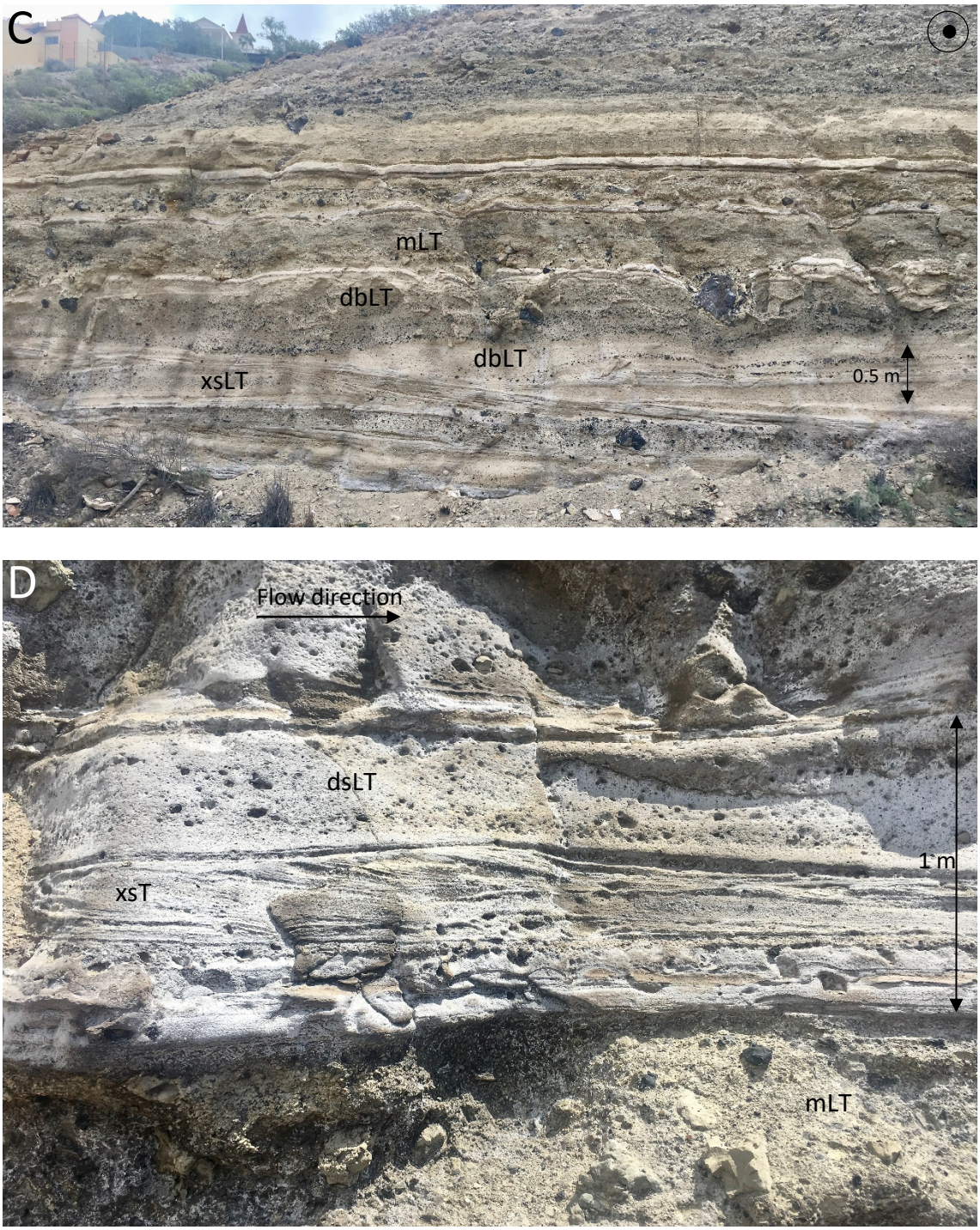

Figure 3.3 *(Continued) -* ***(C)*** *dbLT; xsLT – Base of outcrop shows diffuse-bedded lapilli tuffs that pass laterally into cross-stratified lapilli tuffs. Diffuse bedding predominantly marked by trains of lithic lapilli. Passes vertically into dbLT with lithic units <5 cm thick and mLT. Flow direction is out of the page. (GR: 0330508 3106679)* ***(D)*** *xsT – cross-stratified tuff with low angle forset laminae. Passes vertically into dsLT. Flow direction is from left to right. (GR: 0330353 3107939).*

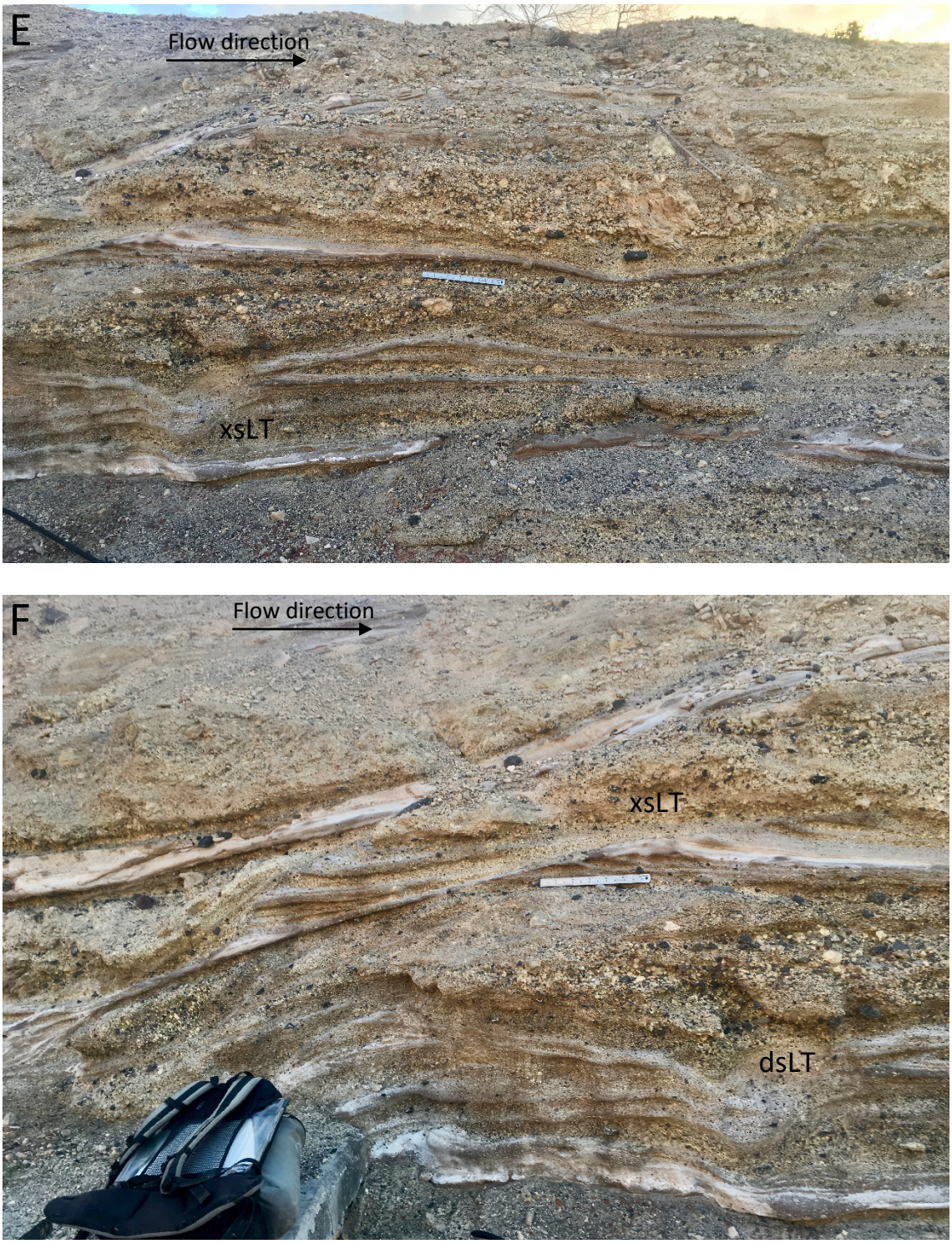

Figure 3.3 *(Continued) -* ***(E)*** *and* ***(F)*** *xsLT – Medial deposits of cross-stratified lapilli tuffs. Forset laminae have low dip angles. Stoss-side laminae are rarely preserved. Flow direction is from left to right. Note the upcurrent dipping strata reflects the plastering of moist ash against the previous deposits. 30 cm rule for scale. (GR: 0330290 3107935).*

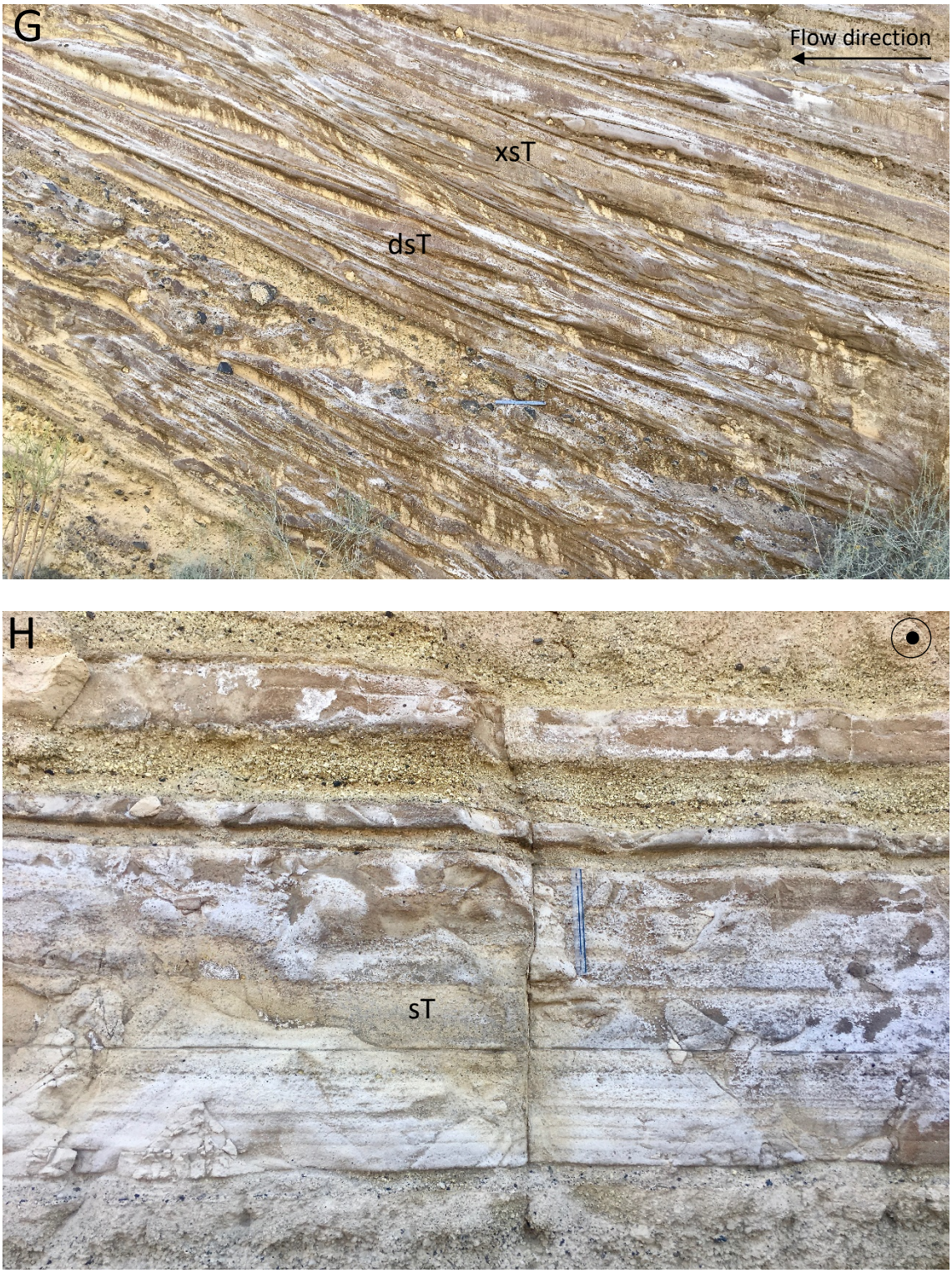

Figure 3.3 *(Continued) -* ***(G)*** *xsT); dsT - proximal, crater infilling, diffuse- stratified tuffs and cross-stratified tuffs. Beds show lateral impersistence and thickness changes. Note alternations between lighter coloured, coarser grained units and darker coloured, finer grained units. 30 cm rule for scale. (GR: 0331057 3106420).* ***(H)*** *sT – Thick layer of sT. Stratification is marked by changes in lithic content and subtle grainsize variations. 30 cm rule for scale. (GR: 0329793 3107997).*

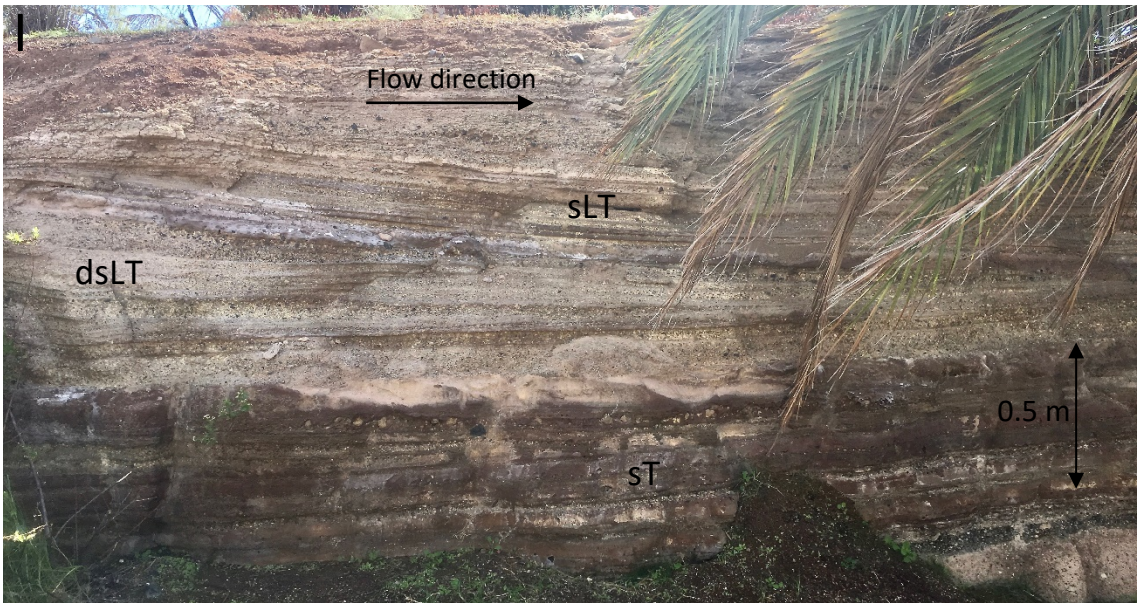

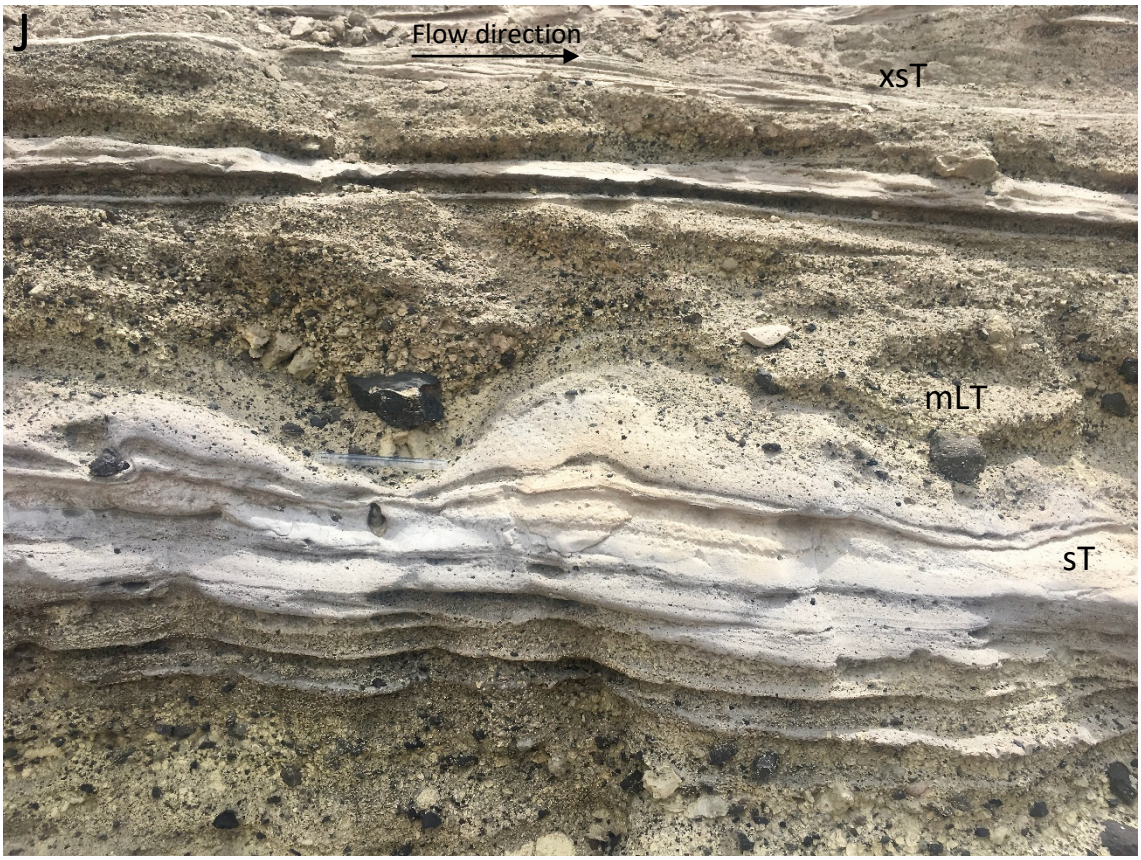

Figure 3.3 *(Continued) -* ***(I)*** *sLT); sT; dsLT – Medial sLT, sT and dsLT. Flow direction is from left to right. Deposits are found vertically above thick, mT. (GR: 0330082 3107958).* ***(J)*** *sT; mLT – Interbedded fine-grained sT with a coarser, lithic-rich mLT. Passes vertically into a xsT. Flow direction is from left to right. 30 cm rule for scale. (GR: 0330308 3107925).*

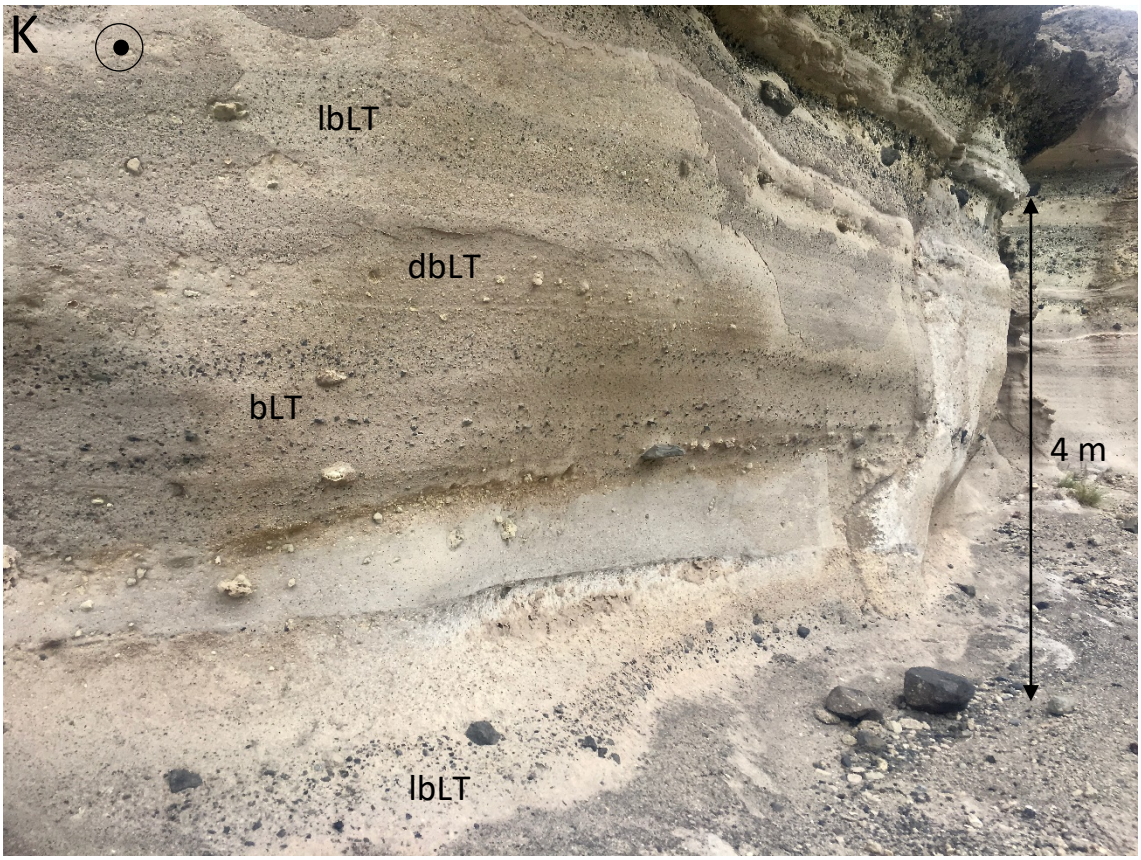

Figure 3.3 *(Continued) -* ***(K)*** *bLT; dbLT - bLT and dbLT within a fine-grained matrix. Bedding is defined by grainsize and lithic content. Diffuse bedding predominantly marked by trains of single lapilli sized clasts. (GR: 0332363 3107396)*

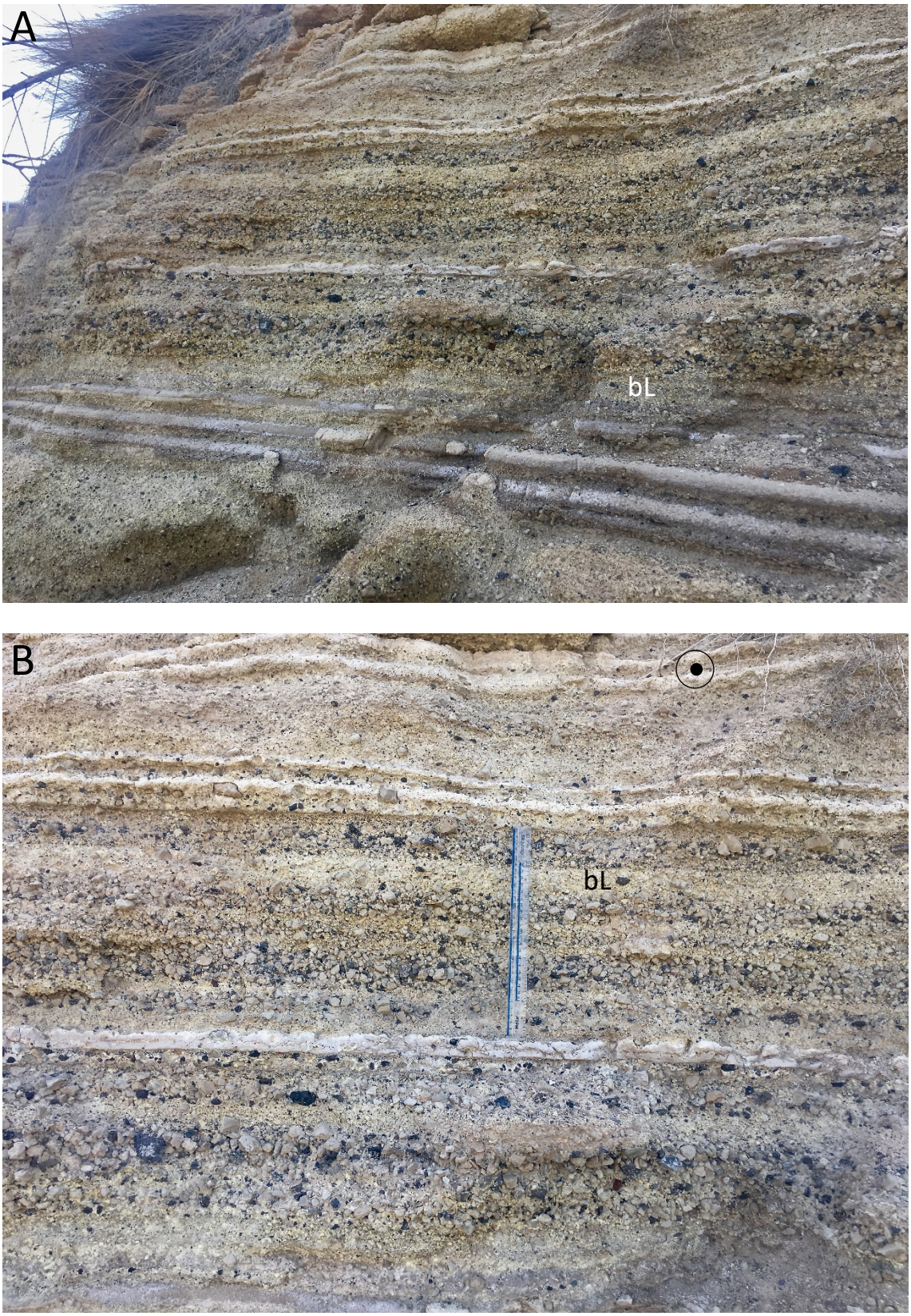

Figure 3.4 *Lithofacies of the Caldera del Rey formation with a fallout origin* ***- (A)*** *and* ***(B)*** *bL - Medial deposits of finely bedded, well sorted, pumice fall units. Bedding is defined by changes in grainsize and lithic content. Likely originated from a plume of almost subplinian dimensions. (B) shows in detail the units towards the top of (A). 30 cm rule for scale. (GR: 0329862 3108103).*

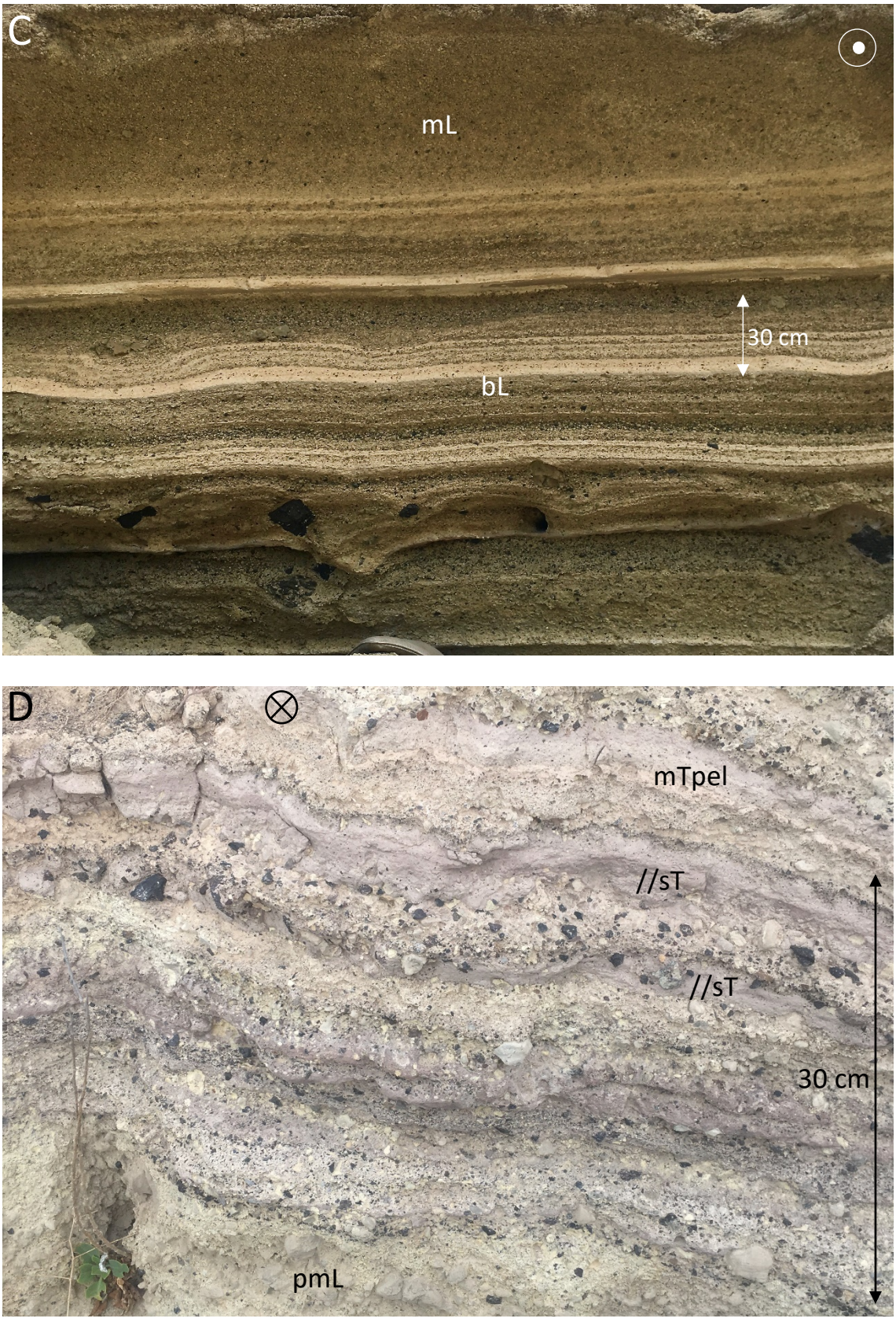

Figure 3.4 *(Continued) -* ***(C)*** *bL; mL - Medial deposits of finely bedded pumice fall units that pass vertically into a massive, moderately sorted pumice fall unit. Angular, framework-supported pumice lapilli with usually subordinate angular lithic lapilli. Likely originate from a subplinian column. (GR: 0330492 3106977)* ***(D)*** *//sT – Thin beds of very fine-grained //sT interbedded with beds of pmL. mTpel closely resemble the parallel-stratified tuffs //sT. (GR: 0330518 3106609).*

Figure 3.5 *Ash aggregation lithofacies of the Caldera del Rey formation -* ***(A)*** *mTpel - laterally continuous lenses of framework supported coated pellets and ash pellets, within a massive, fine ash matrix. The pellets, when coated, have a single rim of finer ash. Note the increased resistant to weathering of the finer rims compared to the hollowed cores. Ruler shows cm's. (GR: 0330495 3106674).* ***(B)*** *mTacc - Variable proportions of accretionary lapilli within a massive and/or bedded fine-grained tuff matrix. The rims of the accretionary lapilli and complex, containing multiple coatings that fine outwards. Rule shows cm's on left hand side. (GR: 0330596 3107709).*

Figure 3.5 *(continued) -* ***(C)*** *mTpel; mTacc - Accretionary lapilli within a fine-grained massive tuff. Ash aggregates fine upwards and increase in concentration, where they transition from dominantly accretionary lapilli to dominantly coated ash pellets. Rule shows cm's on right hand side. (GR: 0330954 3107624).*

3.2 CDR Member A

Member A is composed of a coarse-grained, moderately sorted, thickly bedded (<2 m), pumice fall deposit with a maximum preserved thickness of ~11 m (Figure 3.6). It is composed of lapilli sized pumice and lithic clasts with rare obsidian lapilli. The pumice is generally framework-supported and lacks a matrix. Member A predominantly outcrops in the south and southwest areas of the mapped area (Figure 3.1). The member outcrops over 0.2 km^2. Dips between 4° and 10° that slope towards the southwest are recorded for this member.

The deposits of Member A typically drape the pre-existing topography and maintain a constant thickness when infilling depressions.

The member unconformably overlies basaltic lavas, re-worked sediments and palaeosols, phonolitic lava flows, and an ignimbrite of the Adeje Formation. The upper boundary with Member B is sharp.

The pumice clasts are generally angular to sub-angular and typically make up 80-90% of the deposit. The clasts are mostly lapilli-sized and average 1–3 cm in diameter. However, their size ranges between coarse ash to block size (up to 40 cm in diameter). Pumice clasts are typically low density (Chapter 3.9) and have vesicles that are visible to the naked eye. Dense pumice class occur in much lower quantities (<10 %). The pumice clasts are poorly sorted in proximal locations. However, with distance from the vent the grainsize decreases and the clasts become better sorted. Pumice clasts exhibit fracture and joint bound surfaces.

Lithic fragments are angular and comprise 10-20 % of the deposit. The lithic fragments are generally ash to lapilli sized and are found up to 3-4 cm in diameter. The lithic fragments are predominantly composed of mafic lavas, of which aphanitic basalt is the most dominant (Figure 3.7). Lithic fragments of an orange coloured ignimbrite, belonging to the Adeje formation, are found in high abundance in this member, making up 10% (Figure 3.7).

Figure 3.6 *CDR Member A* ***- (A)*** *Vertical exposure opposite the Las Américas bus station, showing the basal contact and overlying contact with Member B. Represented by Log no. 3 (Figure 3.8). (GR: 0330241 3106276).* ***(B)*** *Ballistic block (aphanitic basalt) found within the upper bedded regions of Log no. 2 (Figure 3.8). (GR: 0330079 3106813).*

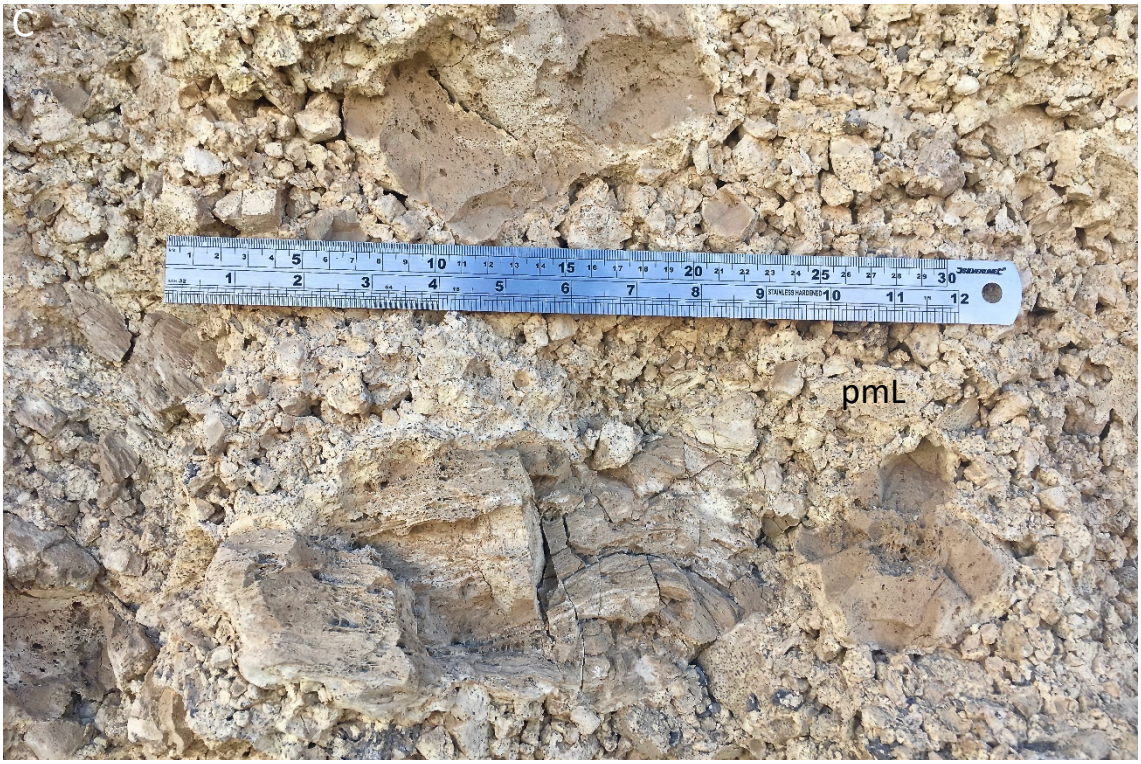

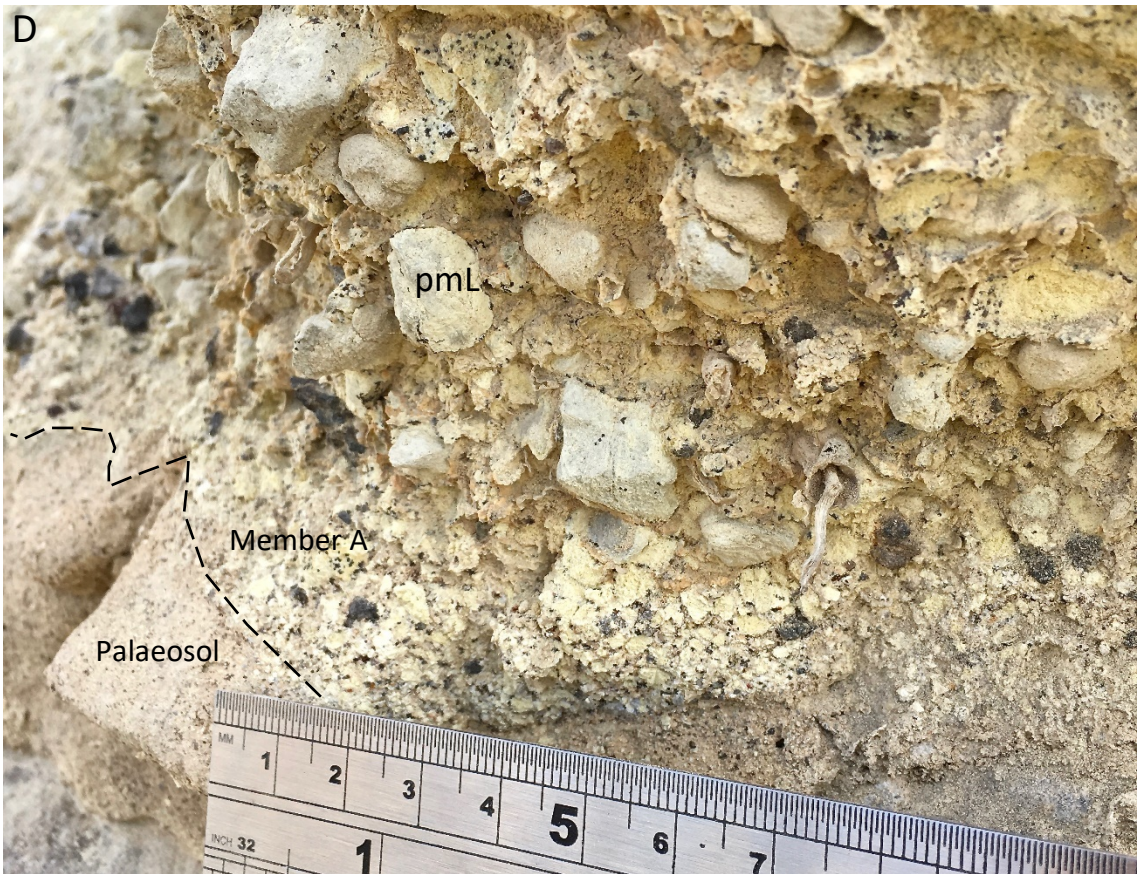

Figure 3.6 *(Continued) -* ***(C)*** *Pumice blocks surrounded by smaller framework-supported pumice clasts. Taken at an outcrop 750 m from source. (GR: 0330425 3106755).* ***(D)*** *Finer-grained base of Member A that passes into the main body. Rule shows 30 cm. (GR: 0330092 3107421).*

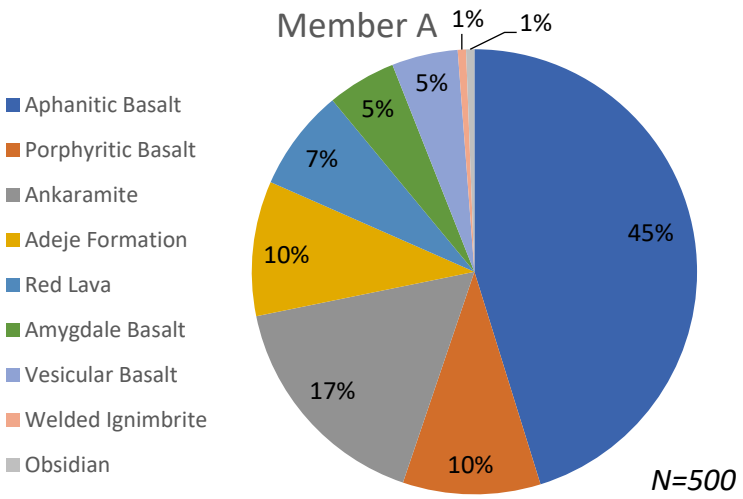

Figure 3.7 *Pie chart showing the abundance of lithic fragments of various compositions within Member A.*

3.2.1 Units

Member A has three sub-units that are characteristic of the structure of the deposit and can be traced across the region (Figure 3.8):

Unit 1 consists of a coarse-grained pumice-rich fall deposit (mL). The unit is typically massive. Unit 1 contains a 4 cm thick base composed of well-sorted pumice (80%) and lithics (20%) clasts measuring 3-4 mm in diameter. This passes gradationally into the main body of the unit. The unit has a maximum thickness of at least 5.7 m close to source (GR: 0330425 3106755). Where the unit lies on the main dispersal axis, 0.98 km from source, it has a thickness of 3.9 m (Figure 3.8). Moving across the main dispersal axis the unit thins to just over 1 m thick (Figure 3.8). Unit 1 passes gradationally into unit 2.

Unit 2 is a coarse-grained, massive, pumice fall deposit (mL). The maximum average size of the lithic fragments is approximately 6 cm, rising from 4.85 cm in unit 1. The unit has a maximum thickness of 3.2 m close to source. Unit 2 has a thickness of 0.9 m on the main dispersal axis at 0.98 km from source (Figure 3.8). The thickness varies across the main dispersal axis, ranging from 1 m to 2.5 m thick (Figure 3.8). There is a transitional boundary between unit 2 and unit 3.

Unit 3 comprises a coarse-grained, bedded pumice fall deposit (bL). The unit is thinly bedded, containing beds 2 to 10 cm thick. In comparison to the other units, there is an increase in the size and abundance of ballistic projectiles in unit 3. Ballistic blocks, commonly composed of mafic lavas, can reach up to 1.4 m in diameter (GR: 0330394 3106697). The unit has a maximum thickness of 1.5 m close to source (Figure 3.8). Unit 3 has a thickness of 1.4 m on the main dispersal axis; moving across the main dispersal axis the unit thins to 0.5 m thick (Figure 3.8). There is a sharp top contact between this unit and the overlying member.

3.2.2 Distal Deposits

The distal outcrops of Member A are lithologically similar to proximal deposits. At a small outcrop near Barranco de Torviscas, 1.77 km from source (GR: 0329803 3107998), the entirety of Member A is exposed. The member has an overall thickness of 1.1 m. Units 1 and 2 are a combined 0.8 m thick, with unit 3 0.3 m thick. The deposits are fairly well sorted and contain pumice clasts with an average maximum size of 2 cm.

Isopach data indicates that Member A was erupted from the southern crater and dispersed to the west (275°) (Chapter 4.1). The member is at its thickest and coarsest in line with this axis. Moving off this axis the deposits can thin by as much as 4.7 m over 0.66 km. Similarly, the grainsize also decreases from an average maximum size of 6 cm to 5.1 cm over this distance. Additionally, the member generally thins, fines and becomes better sorted with distance from the source.

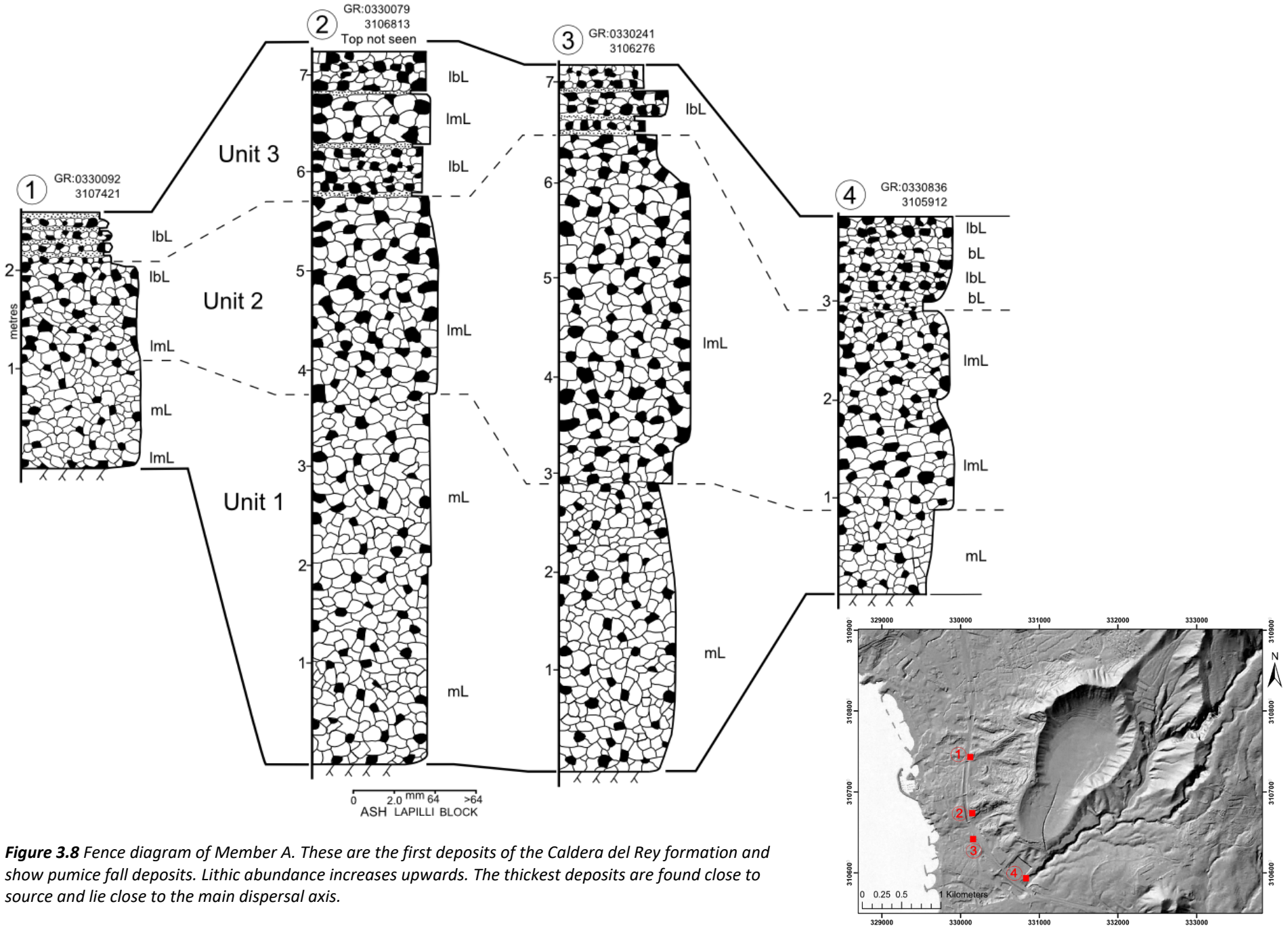

Figure 3.8 *Fence diagram of Member A. These are the first deposits of the Caldera del Rey formation and show pumice fall deposits. Lithic abundance increases upwards. The thickest deposits are found close to source and lie close to the main dispersal axis.*

3.3 CDR Member B

Member B is composed of pyroclastic density current deposits with a maximum preserved thickness of ~10 m. It generally consists of stratified and cross-stratified, fine-grained and coarse-grained tuffs (Figure 3.9). The deposits are commonly moderately sorted and contain ash and lapilli sized pumice and lithic fragments within a fine-ash matrix. It is typically a weathered pale cream colour and thickly (80 cm) to thinly (5 cm) bedded. Member B is dispersed in the southern and western areas of Caldera del Rey (Figure 3.1). The member outcrops over 0.36 km^2. Bedding dips are 5° and 7° towards the southwest.

The deposits of Member B generally maintain a constant thickness and the individual flow units can be traced radially across the area south of Caldera del Rey.

Member B sits concordantly on Member A. In proximal areas the contact is gradational over 0.5 m, but in medial areas the contact is sharp. The top contact is generally gradational into Member C. In proximal areas it grades over a distance of 1-2 m, while in southern areas it is locally overlain by a younger ignimbrite from Las Canadas Volcano.

The pumice clasts are generally sub-rounded to sub-angular, typically make up 15-25% of the deposit, and reach up to 14 mm in diameter. Pumice clasts decrease in size slightly with distance from the vent. The pumice clasts are predominantly low density (<90%), with sub-rounded to sub-angular vesicles up to 1-2 mm in diameter (Chapter 3.9).

Lithic fragments are angular to sub-angular and comprise 20-30% of the deposit. The lithic fragments are generally ash to lapilli sized (<2.5 cm in diameter; average 1 cm). The lithologies are similar to those found in Member A, with a small decrease in the abundance of the Adeje formation ignimbrite and an increase in the abundance of older welded ignimbrites. The lithic fragments predominantly consist of mafic lavas, of which aphanitic basalt makes up 44%, and ankaramite 18% (Figure 3.10).

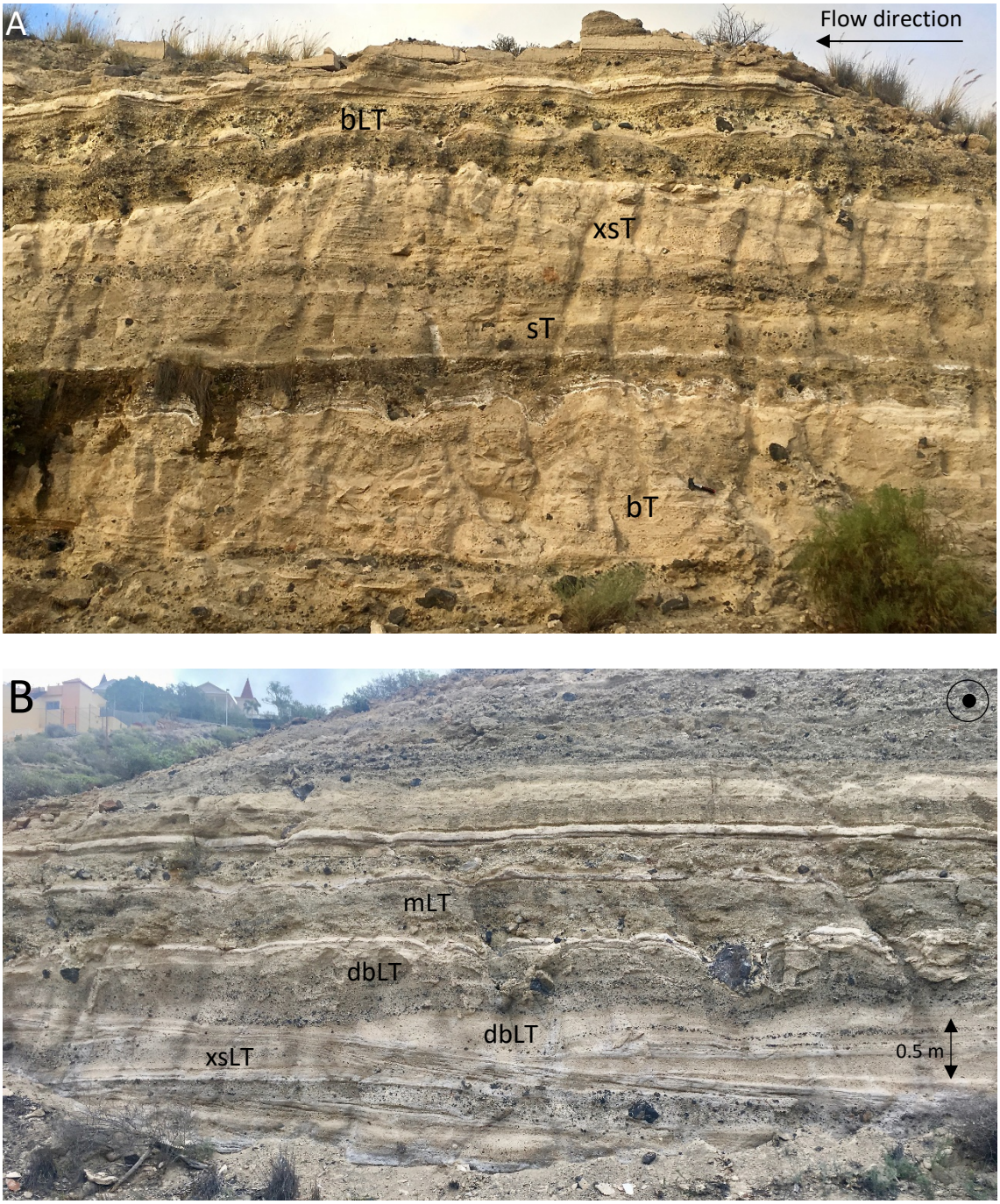

Figure 3.9 *CDR Member B –* ***(A)*** *Proximal deposit showing the base of Member B where two thickly bedded fine-grained packages are found, which transition vertically into finer- and coarser-grained beds. Black hammer is 20cm. (GR: 0330456 3106717).* ***(B)*** *Cross-stratified and diffuse-bedded tuffs at a proximal outcrop 550m from source. (GR: 0330508 3106679).*

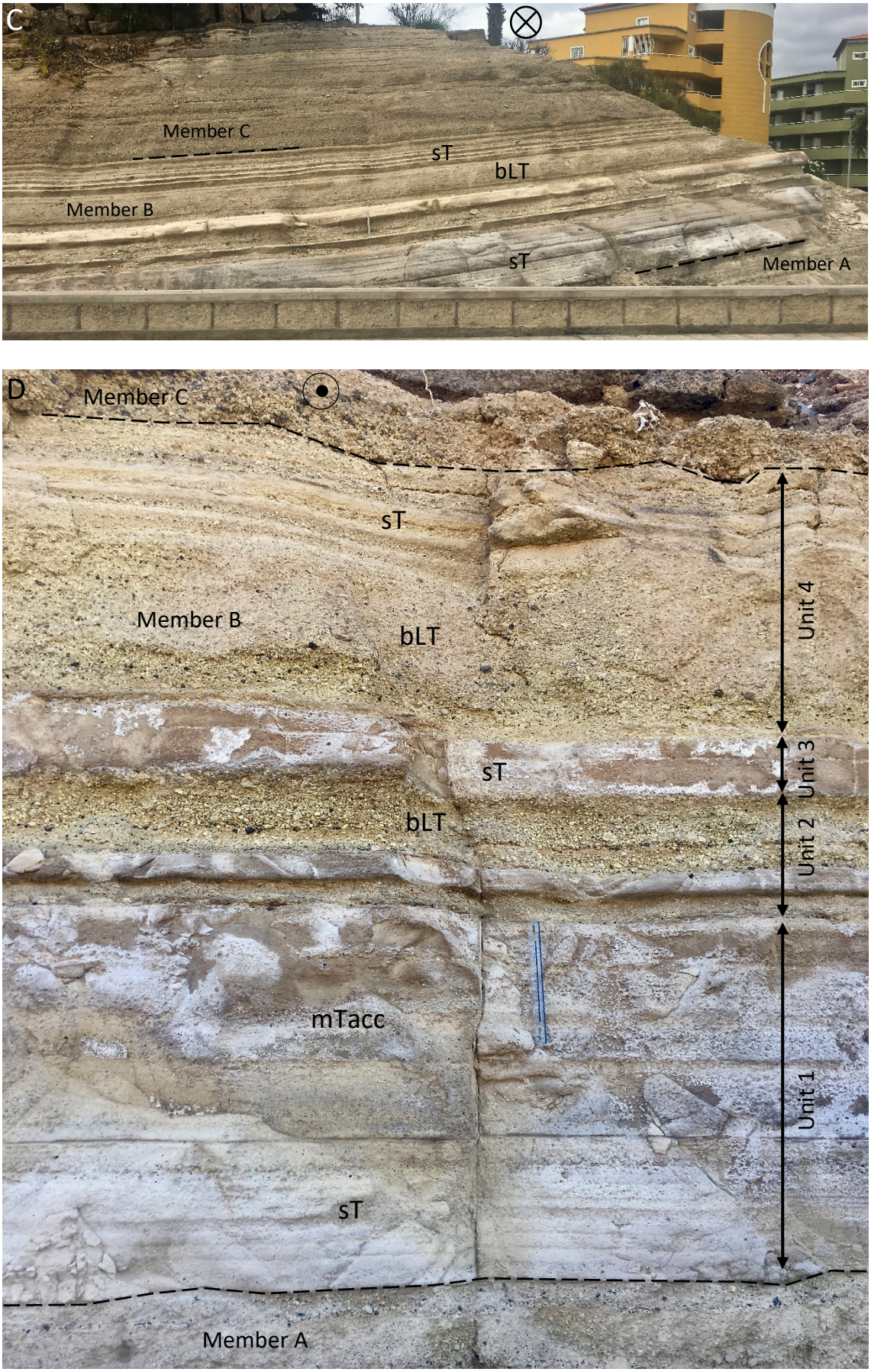

Figure 3.9 *(Continued) -* ***(C)*** *Medial outcrop showing the full sequence of Member B. The member transitions from thicker packages of stratified tuffs into thinner packages. Silver rule shows 30 cm. (GR: 0330048 3107445).* ***(D)*** *Medial outcrop showing the full sequence of Member B found 1.78 km from source. (GR: 0329793 3107997).*

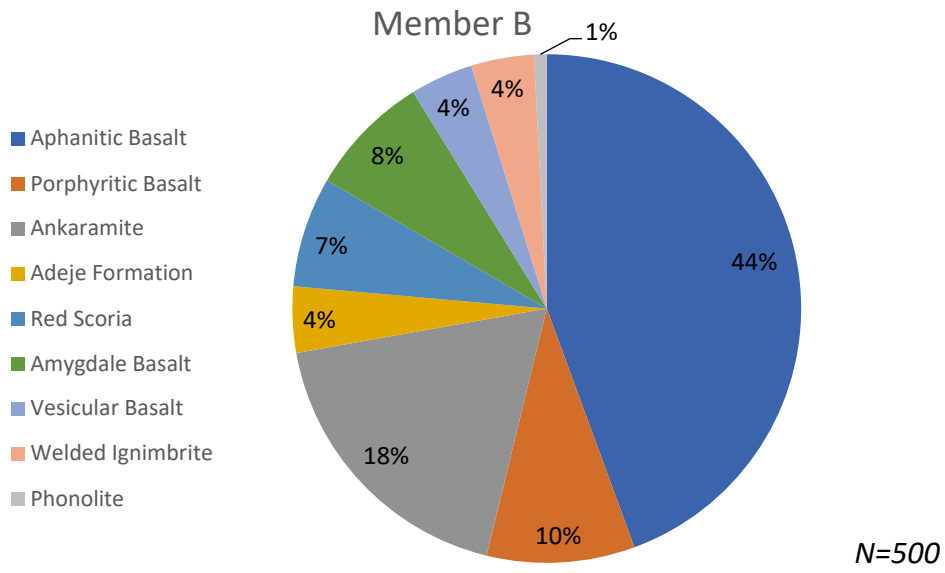

Figure 3.10 *Pie chart showing the abundance of lithic fragments of various compositions within Member B.*

Pumice and lithic clasts are enclosed in a light brown fine-grained matrix that makes up 45-65% of the deposit. It contains sanidine and amphibole crystals, <5 mm, that typically make up ~5% of the matrix.

The deposits of Member B show evidence of cross-stratification, diffuse bedding and parallel stratification. Cross-stratification is generally low angle, between 3° and 10° to bedding, and laterally persistent over 10s metres. Diffuse bedding is generally discontinuous, sub-parallel and undulatory and is defined by cm-thick lithic-rich horizons that are laterally persistent over several metres. Parallel stratification, commonly spaced 2–5 cm, is laterally persistent over 100s metres.

3.3.1 Units

Member B has four sub-units that are characteristic of the structure of the deposit and can be traced across the region (Figure 3.11).

Unit 1 comprises a thickly bedded, fine-grained sequence of sT. The unit exhibits stratifications 1-5 cm thick. Unit 1 contains locally diffuse stratified layers of matrix supported accretionary lapilli and/or coated pellets (mTacc). Stratification at the base and middle of the unit is defined by 1–2 cm thick horizons of lapilli-sized pumice and

lithic clasts. Variable proportions of ash aggregates are found throughout the unit. However, towards the top of the unit the abundance decreases. The unit has a maximum thickness of 1.8 m close to the vent (Figure 3.11) where it is thickly bedded (60-80 cm) and cross-stratified in places. Medial exposures reach 1 m thick, whereas in distal exposures it is 0.83 m thick (Figure 3.11). Unit 1 passes gradationally into unit 2.

Unit 2 is a package of bLT and bT. The deposits are thin to medium bedded (3 - 20 cm). The boundaries between these individual packages are often sharp. The unit has a maximum thickness of 1.2 m close to source (Figure 3.11). This thins to 0.33 m in medial exposures, over a distance of 0.8 km. In distal exposures it is 0.3 m thick. There is a sharp contact between unit 2 and unit 3.

Unit 3 is composed of a bedded, fine-grained deposit of stratified tuffs (sT). The unit contains stratifications which are commonly spaced 1-10 cm. Unit 3 contains variable amounts of diffuse stratified accretionary lapilli (5-20 %) and coated pellets (5-25 %). In proximal locations the unit is locally cross stratified and diffuse stratified (Figure 3.9). The unit has a maximum thickness of 1.80 m close to source (Figure 3.11). Medial exposures of unit 3 measure 0.2 m thick (Figure 3.11) whereas in distal exposures it is 0.14 m thick. There is a sharp contact between unit 3 and unit 4.

Unit 4 is a package of mLT, sT, mTacc and mTpel. The unit is bedded (2.5 m - 5 cm). Ash aggregates occur as separate beds composed entirely of accretionary lapilli and pellets. The bases of these beds are typically composed of matrix to clast supported quantities of accretionary lapilli; the middle, framework-supported coated pellets, and the top contains poorly preserved, framework-supported ash pellets.

The base and middle of unit 4 is thickly to very thickly bedded (40 cm - 2.5 m). This passes up into the upper thinly bedded (1 m - 5 cm) region of the unit. Additionally, the top of the unit shows bedded (50 - 5 cm) pumice lapilli fall deposits (mL). The boundaries between these individual packages are often sharp. The unit has a maximum thickness of 5.12 m close to source (Figure 3.11). This thins to 1.03 m in medial exposures, over a distance of 0.8 km. In distal exposures it is 0.64 m thick. There is a gradational contact between unit 4 and the above member.

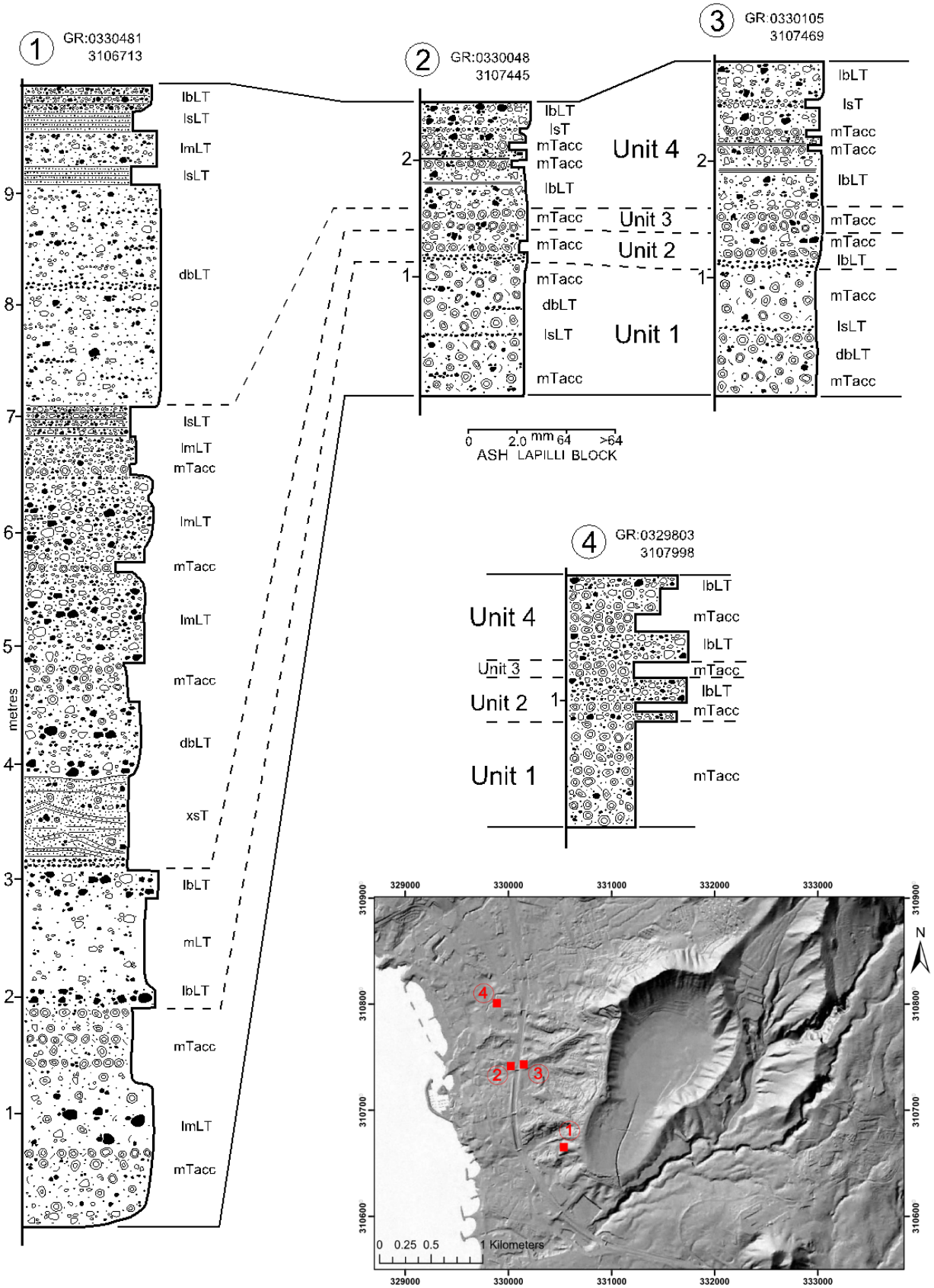

Figure 3.11 *Fence diagram of Member B. The deposits originated from the southern crater of Caldera del Rey. The member maintains a constant unit structure away from the vent.*

3.3.2 Ash Aggregates

Ash aggregates are moderately abundant (10-60%) within the fine-grained beds of Member B. They appear in thin to medium bedded fine-grained packages and in beds composed wholly of ash aggregates. Accretionary lapilli, coated pellets and ash pellets are found that can either be fully intact or broken fragments. Fining upwards sequences are common.

Accretionary lapilli, typically sub-spherical, occur matrix-supported within the stratified and cross-stratified tuffs. The size of the aggregates are usually between 5 and 8 mm. The core of the aggregates are often massive, coarse-grained and resemble the matrix of the beds they are found within. The rims, typically 1 to 1.5 mm thick, are made up of multiple concentric layers of fine-grained ash that commonly fine outwards. However, in some cases, the rims show a fine-coarse-fine structure outward. The accretionary lapilli are generally well preserved.

Coated pellets with a single ultra-fine-grained rim are matrix- to clast-supported. They are typically spherical to sub-spherical, 3 mm in diameter, with rims commonly 0.5 mm thick. Conversely, ash pellets occur in exclusively framework-supported beds. They are composed of fine to medium ash and are typically 2 mm in diameter. However, they are commonly poorly preserved.

3.3.3 Distal Deposits

The distal deposits of Member B maintain the same unit structure as those in proximal and medial locations (Figure 3.9). A distal outcrop, 1.77 km from source (GR: 0329803 3107998), has an overall thickness of 1.93 m. Units 1, 2, 3 and 4 measure at 0.83 m, 0.32 m, 0.14 m and 0.64 m respectively. The grainsize is finer within the mLT compared to proximal outcrops, with the average maximum thickness of the pumice clast 1 cm in diameter.

The units of Member B can be traced around the southern and western areas of Caldera del Rey. The member thins and fines with distance from the source.

3.4 CDR Member C

Member C is composed of a thick, coarse-grained, moderate to poorly sorted, pumice fall deposit (mL, bL) with a maximum preserved thickness of ~18 m (Figure 3.12). The pumice is almost always framework-supported and lacks a matrix. The member is typically a weathered yellow colour and very thickly bedded (<5 m). It is composed of lapilli sized pumice and lithic clasts. Member C contains thin fine-grained //sT that separate the pumice-fall deposits. Member C predominantly outcrops in the southern and western areas of mapped area (Figure 3.1). The member outcrops over 0.32 km^2. Bedding dips between 4° and 7° are recorded that slope towards the south and west of Caldera del Rey.

The deposits of Member C typically drape the pre-existing topography and maintain a constant thickness when infilling depressions.

Member C sits concordantly on the deposits of Member B. In proximal areas the contact may be gradational due to the clast supported fall deposits found within unit 4 of Member B. Further from source the contact is sharp. A sharp boundary is observed where the member passes up into the deposits of Member D. In southern areas the member is locally overlain by a dark coloured, younger ignimbrite from Las Canadas volcano.

The pumice clasts are generally sub-angular, typically make up 65-85% of the deposit and average 1 - 3.5 cm in diameter. However, larger pumice clasts can reach up to 35 cm. Pumice clasts decrease in size and become moderately sorted with distance from the vent. The pumice clasts are mostly low density (Chapter 3.9) and micro-vesicular.

Lithic fragments are angular and make up 10-35% of the deposit. The lithic fragments are generally ash to lapilli sized (<3.3 cm in diameter; average 1.2 cm). The lithic fragment lithologies are predominantly composed of aphanitic basalt (48%), porphyritic basalt (12%) and ankaramite (17%). Small amounts of welded ignimbrite (3%) and phonolite (3%) are found (Figure 3.13).

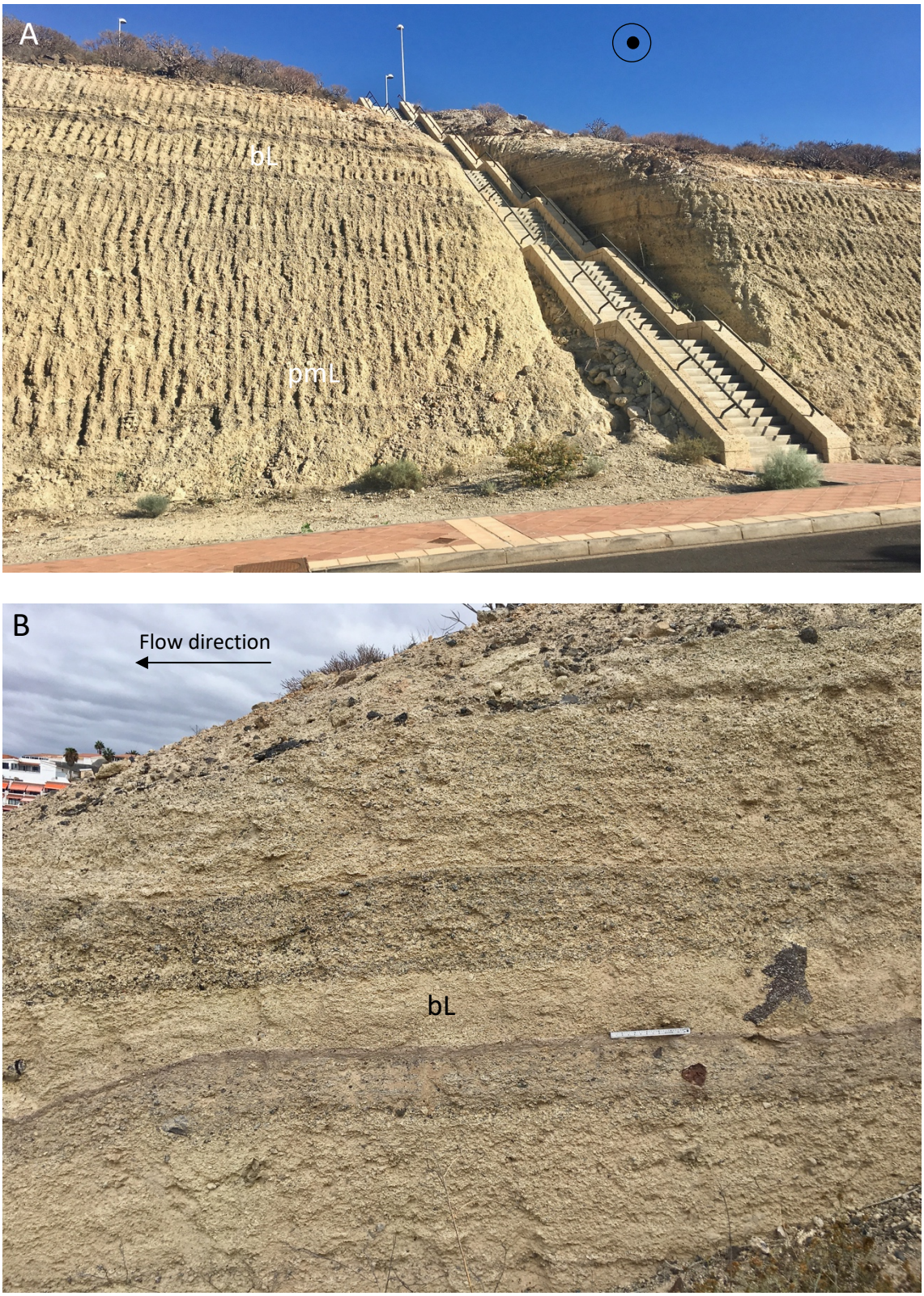

Figure 3.12 *CDR Member C –* ***(A)*** *Medial outcrop of thickly bedded pumice lapilli of unit 1, 650 m from source (GR: 0330503 3106631).* ***(B)*** *Bedded deposits defined by changes in lithic abundance, interstratified with thin beds of parallel laminated tuff. Found towards the top of unit 1. (GR: 0330509 3106606).*

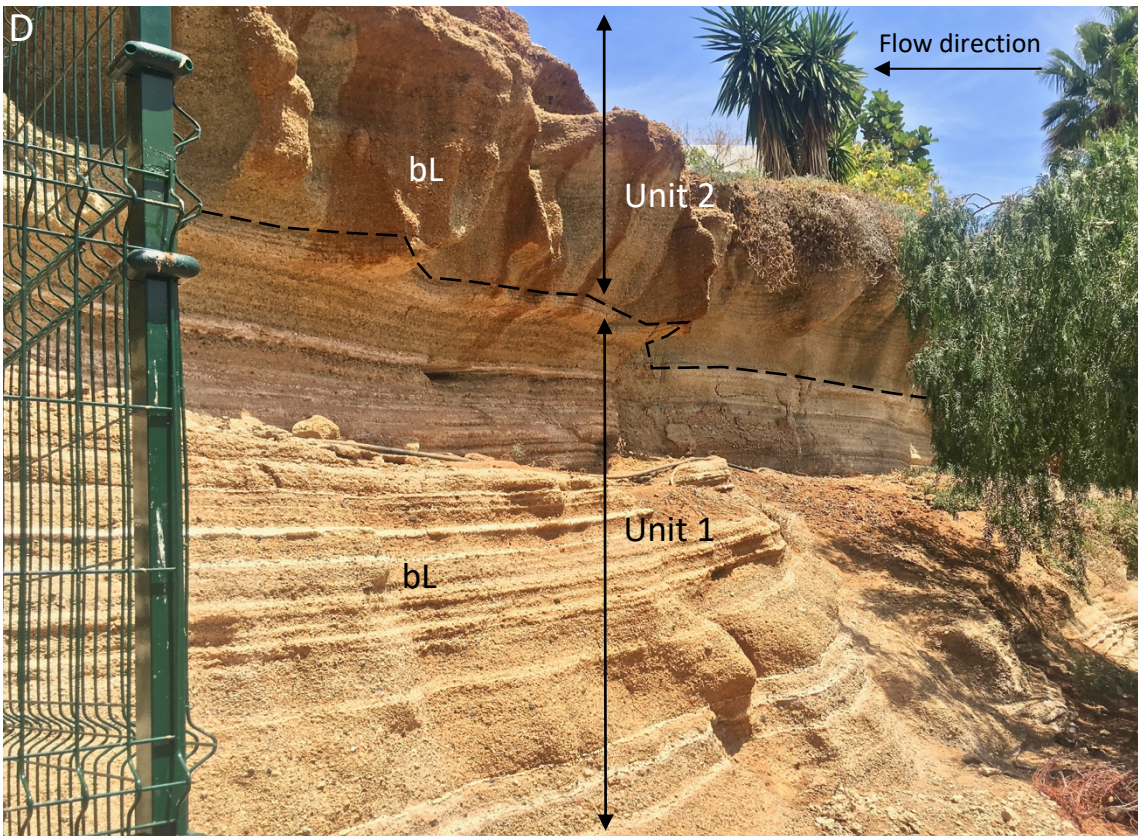

Figure 3.12 *(continued) -* ***(C)*** *Thinly bedded units from a medial exposure. Bedding defined by changes in grainsize and lithic content. (GR: 0329865 3108100).* ***(D)*** *Exposure of Member C to the southwest of Caldera del Rey. The thinly bedded unit 1 transitions into thickly bedded unit 2 (GR: 0329935 3107619).*

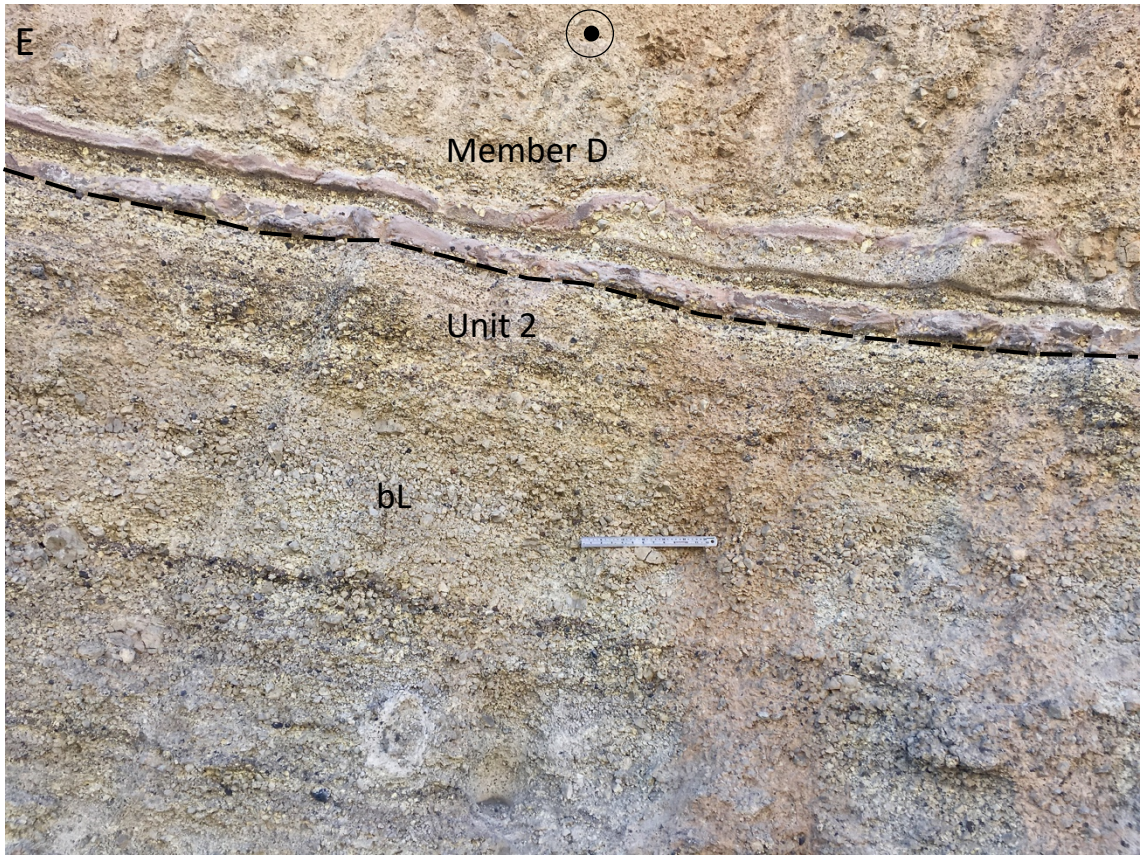

Figure 3.12 *(continued) -* ***(E)*** *Detail of the internal stratification in unit 2. The unit is overlain by Member D. (GR: 0330134 3107545).* ***(F)*** *Fractured pumice clast surrounded by moderately sorted pumice clasts. (GR: 0329946 3107488).*

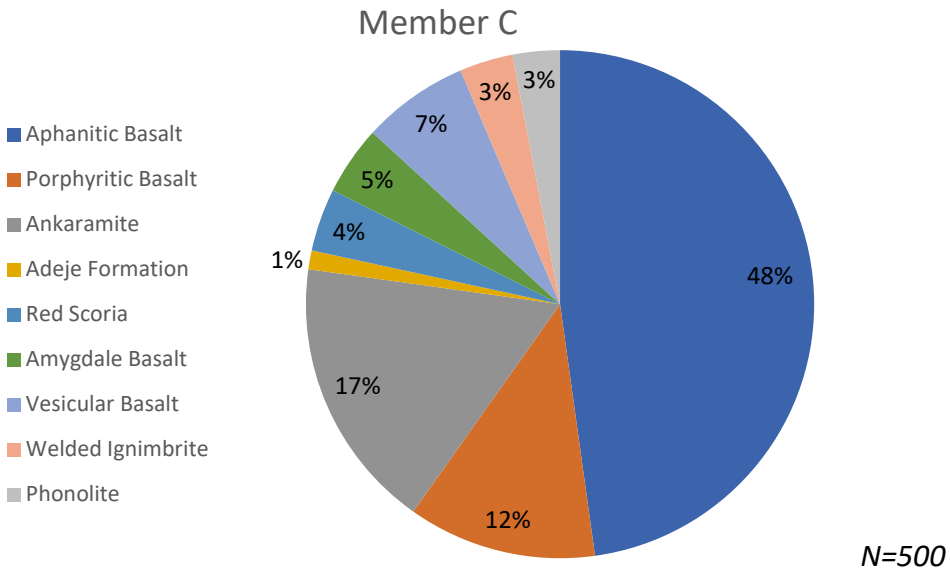

Figure 3.13 *Pie chart showing the abundance of lithic fragments of various compositions within Member C.*

3.4.1 Units

Member C has two sub-units that are characteristic of the structure of the member and can be traced across the region (Figure 3.14).

Unit 1 consists of multiple coarse-grained pumice-rich fall deposits (mL, bL). The unit is typically very thickly bedded (0.3 – 5.75 m) to thinly/medium bedded (3-20 cm). Unit 1 contains distinct lithic rich (40%) and lithic poor (15%) beds that are normally between 10 and 35 cm thick. The unit has a maximum thickness of at least 16.5 m close to vent (GR: 0330425 3106755). The unit thins to 3.15 m in medial locations (Figure 3.14). In the southern areas of Caldera del Rey the unit is thickly bedded, whereas in western areas it is thinly bedded. Unit 1 passes gradationally into unit 2.

Unit 2 comprises a bedded, coarse-grained pumice-rich fall deposit (bL). The unit is typically thickly to very thickly bedded (0.5–1.9 m) with internal stratifications (1-3 cm). There is an increase in the abundance of lithic fragments in unit 2 with lithic rich horizons (35-40%) typically 1–2 cm thick. A fine-grained matrix is present (<20% of the deposit). The unit has a maximum thickness of at least 2.9 m where it is exposed 1.1 km from the vent (Figure 3.14). In southern medial locations the unit is 1.6 m thick, whereas in

western medial locations it is 2.4 m thick (Figure 3.14). A sharp boundary is observed where unit 2 passes up into the deposits of Member D.

3.4.2 Distal Deposits

The distal deposits of Member C maintain the same unit structure as the medial deposits (Figure 3.12). A distal outcrop, 1.57 km from source (GR: 0329933 3107766), has an overall thickness of at least 4.6 m. Unit 1 measures at least 2.6 m and unit 2 is 2 m thick. The grainsize is finer within the mL compared to medial outcrops, with the average maximum thickness of the pumice clast 2 cm in diameter. The member generally thins, fines and becomes better sorted with distance from the source.

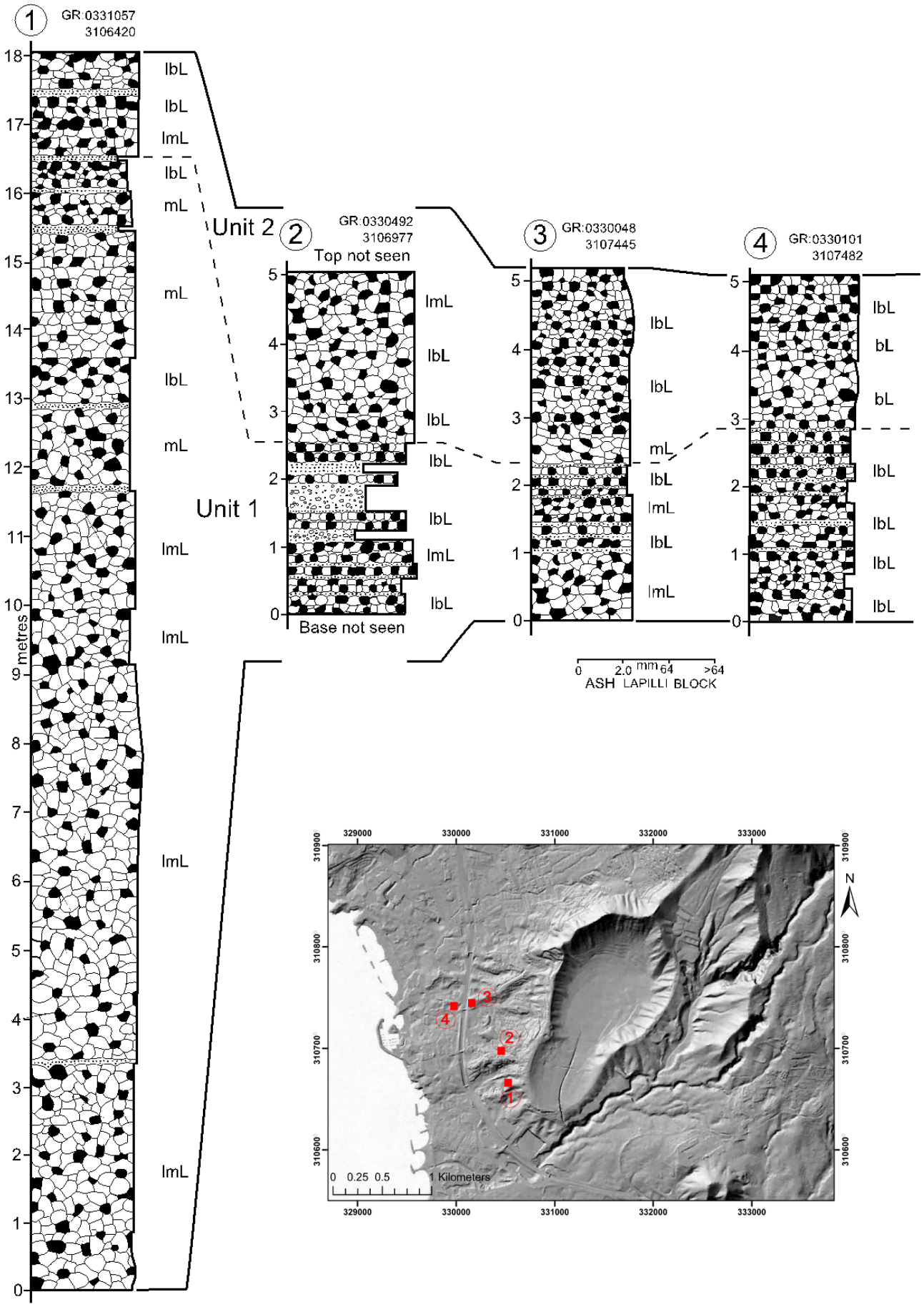

Figure 3.14 *Fence diagram of Member C. These are the first deposits from the northern crater of the Caldera del Rey formation and show pumice fall deposits. The logs are positioned with increasing distance from the estimated initial dispersal axis.*

3.5 CDR Member D

Member D predominantly consists of xsLT, dbLT and mLT, interbedded with thin ash aggregate bearing layers (mTacc) and pumice fall deposits (bL) (Figure 3.15). This member is up to 34 m thick in proximal locations. The deposits are commonly poorly to moderately sorted and contain ash to block sized pumice and lithic clasts within a fine- to medium-ash matrix. It is typically a weathered cream colour, very thickly (200 cm) to thinly (3 cm) bedded and radially dispersed around Caldera del Rey (Figure 3.1). Member D is the most widely dispersed member and outcrops over 3.23 km^2. Bedding dips between 4° and 52° are recorded that slope radially away from the vent. Westward dipping beds, <30°, are exposed east of Caldera del Rey, where the deposits are plastered up against a slope of 'Old Basaltic Series' lavas.

The deposits of Member D are often difficult to trace laterally and show lateral lithofacies transitions away from the vent (see section 3.9). The deposits thicken into palaeovalleys (Figure 3.15A) and generally infill topographic low points.

The lower contact is concordant with Member C. In southern areas the contact is fairly gradational over 0.3 m. However, in western areas a sharp contact is observed. The member unconformably overlies basaltic lavas and the Adeje formation. The upper boundary with Member E is sharp.

The pumice clasts are generally sub-rounded and make up 5-40% of the deposit. Pumice clasts are generally lapilli-sized (<8.8 cm in diameter, average 0.5-1.3 cm). Pumice clasts are typically high density (Chapter 3.9) and microvesicular. Vesicles that are visible to the naked eye are generally sub-spherical and reach up to 1.5 mm in diameter.

Lithic fragments are angular and make up 5-40% of the deposit. The lithic fragments range in size from coarse ash to block sized (<50 cm in diameter; average 0.5-2 cm). The lithic fragment lithologies are predominantly composed of aphanitic basalt (33%), ankaramite (15%) and welded ignimbrite (20%) (Figure 3.16).

Figure 3.15 *CDR Member D –* ***(A)*** *Palaeovalley infilling deposits of Member D overlying Member C. (GR: 0330126 3107537). Photo credits: Alexis Schwartz* ***(B)*** *Basal outcrop of Member D unconformably overlying mafic lavas. Basal deposits of massive pellet tuffs (mTpel) pass up into massive lapilli tuffs (mLT). (GR: 0330793 3107920).*

Figure 3.15 *(Continued) -* ***(C)*** *Proximal deposits of unit 2 showing interbeds of massive lapilli tuffs (mLT) and stratified lapilli tuffs (sLT). (GR: 0330952 3107700).* ***(D)*** *Close-up of the medial deposits of unit 1. Diffuse-bedded lapilli tuffs (dbLT) pass vertically upwards to stratified lapilli tuffs (sLT) and lithic-rich massive lapilli tuffs (lmLT). (GR: 0330551 3107684).*

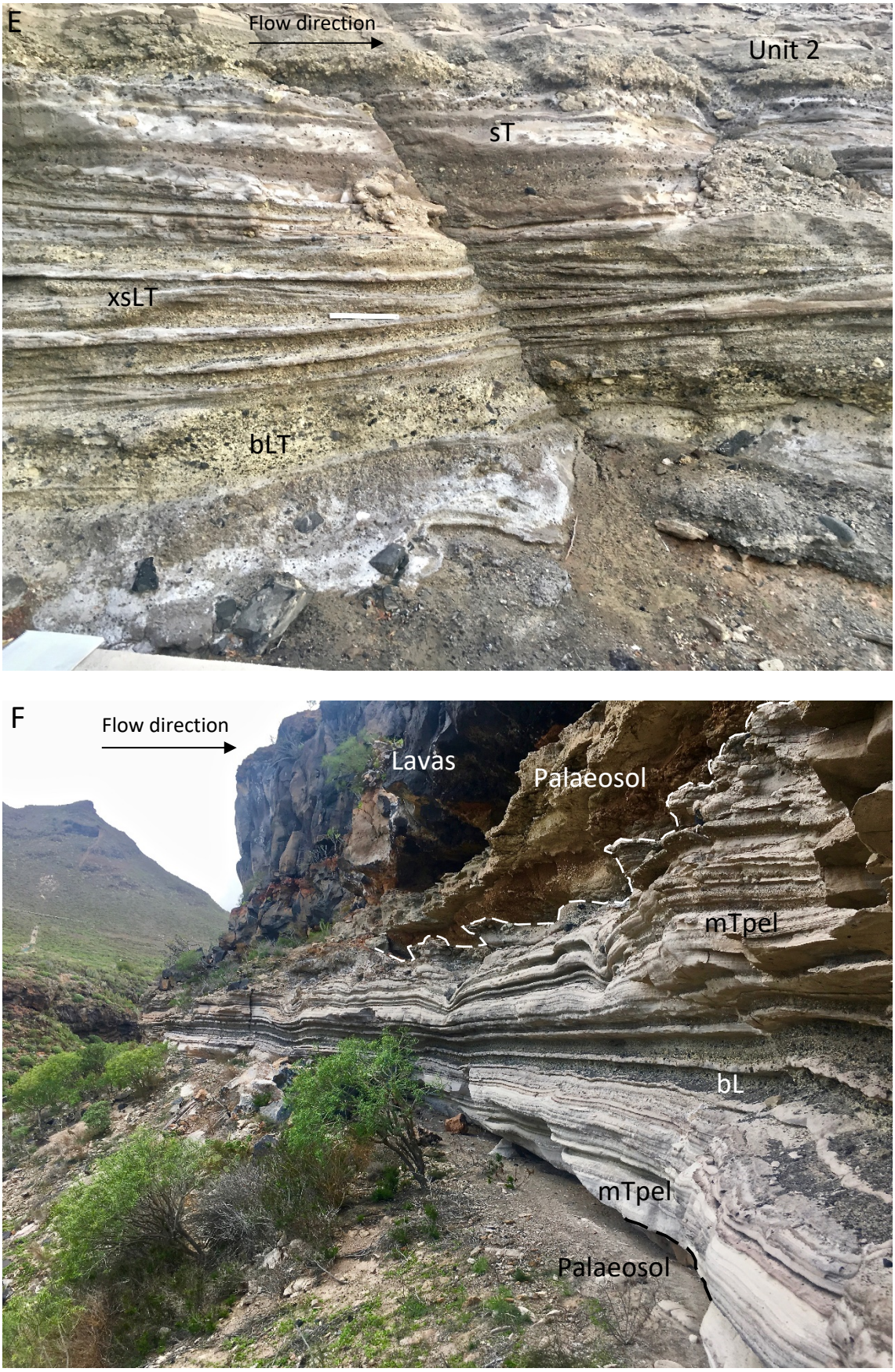

Figure 3.15 *(continued) –* ***(E)*** *Medial deposits of unit 2 showing interbeds of cross-stratified lapilli tuffs (xsLT) interbedded with bedded lapilli tuffs (bLT) and stratified tuffs (sT). (GR: 0330354 3107943).* ***(F)*** *Distal outcrop exposed in Barranco del Rey, composed of predominantly massive pellet tuffs (mTpel) and bedded pumice fall deposits (bL). (GR: 0333177 3107862).*

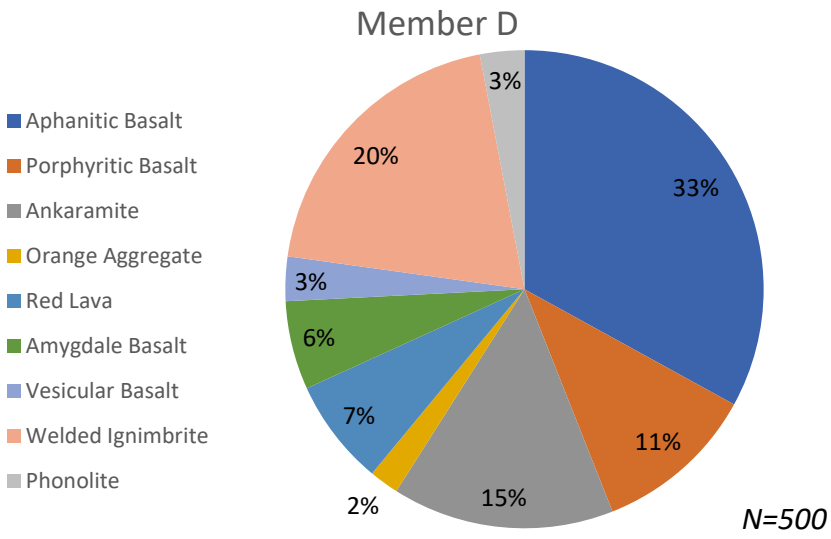

Figure 3.16 *Pie chart showing the abundance of lithic fragments of various compositions within Member D.*

Member D is predominantly composed of a fine-grained matrix that makes up 25-70% of the deposit. The matrix is generally a light brown colour. It contains sanidine and amphibole crystals, <10 mm, that typically make up <5% of the matrix.

The deposits of Member D are diffuse bedded, cross-stratified and parallel stratified. The bedforms typically have wavelengths <2 m and amplitudes <0.3 m (Figure 3.17; Table **3.2**). Cross-stratification is generally low angle, between 5° and 15°, and laterally persistent over centimetres to 10s metres. Diffuse bedding is generally discontinuous, sub-parallel and undulatory. The bedding is typically defined by dm-thick lithic-rich horizons. These beds are laterally persistent up to 15 m. Parallel stratifications, commonly spaced 2–10 cm, are laterally persistent for 10s metres.

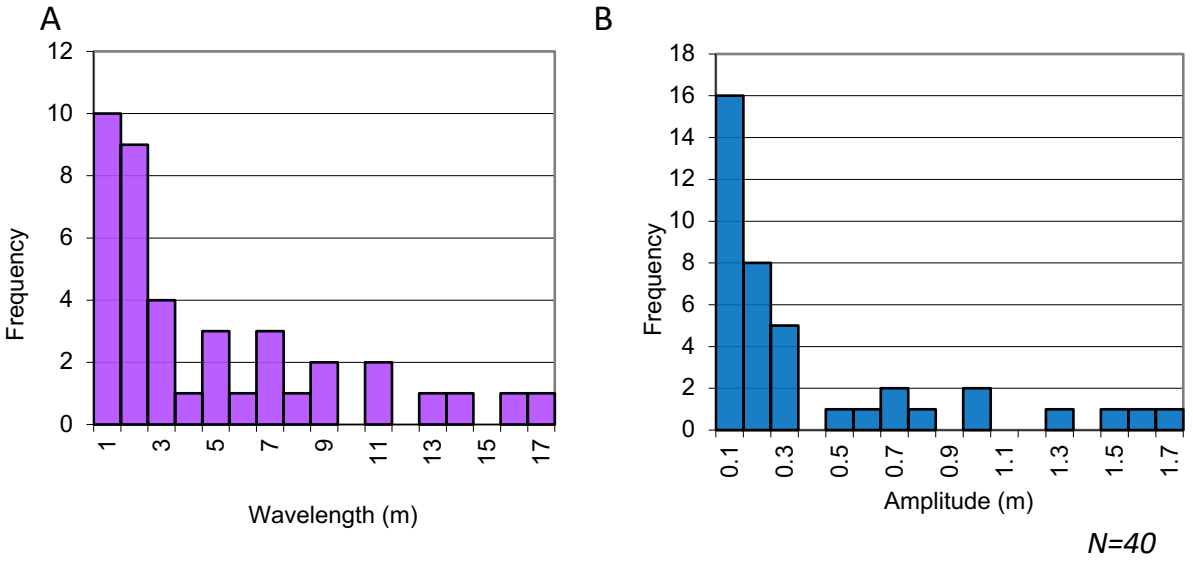

Figure 3.17 *Member D bedforms* ***(A)*** *Plot of wavelength against frequency* ***(B)*** *Plot of amplitude against frequency*

	Wavelength (m)	Amplitude (m)
Mean average	4.4	0.37
Maximum value	17	1.7
Minimum value	0.28	0.02

Table 3.2 *Table showing the mean, maximum and minimum values recorded in the Member D bedforms.*

3.5.1 Units

Member B has two sub-units that are characteristic of the proximal structure of the deposit (Figure 3.18).

Unit 1 comprises packages of dominantly mLT and bLT. These are interbedded with sLT, mL and mTpel. The unit is medium to very thickly bedded (10-200 cm) and lithic-rich close to source. In eastern and western areas unit 1 contains a 1.5 m thick base composed of variable amounts of coated pellet (0-60%) within a light cream coloured, fine-grained ash matrix. Towards the top of the unit there is a slight increase in the abundance of ash aggregates and sLT. The unit has a maximum thickness of 18.5 m close to source, 600-700 m from the vent (Figure 3.18). Unit 1 passes gradationally into unit 2.

Unit 2 comprises packages of mainly mLT, bLT and sLT. These are interbedded with sT, mL and mTpel. The unit is thin to thickly bedded (8-90 cm) and lithic-rich close to source. Pumice-rich, matrix- to clast-supported beds occur occasionally in this unit. The top of the unit sees an increase in the number of thinly bedded stratified tuffs and a decrease in the average bed thickness. The unit has a maximum thickness of 15.5 m close to source, 600-700 m from the vent (Figure 3.18). A sharp contact is observed where unit 2 is overlain by Member E.

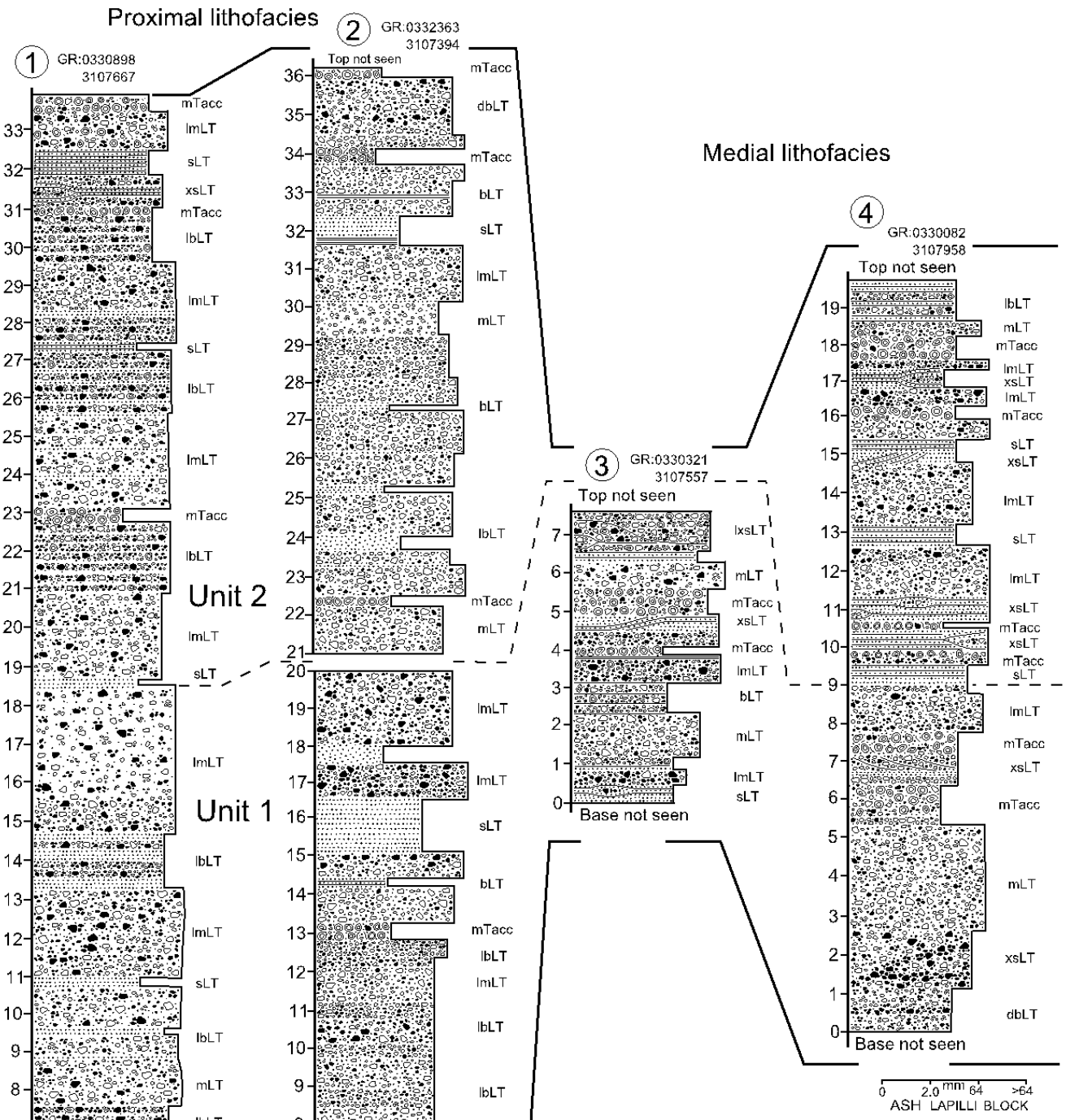
Proximal lithofacies
Medial lithofacies
1
GR:0330898
3107667
2
GR:0332363
3107394
Top not seen
3
GR:0330321
3107557
Top not seen
4
GR:0330082
3107958
Top not seen
Unit 2
Unit 1
Base not seen
Base not seen
Base not seen
mTacc
lmLT
sLT
xsLT
lbLT
dbLT
bLT
mLT
lxsLT
0 2.0 mm 64 >64
ASH LAPILLI BLOCK

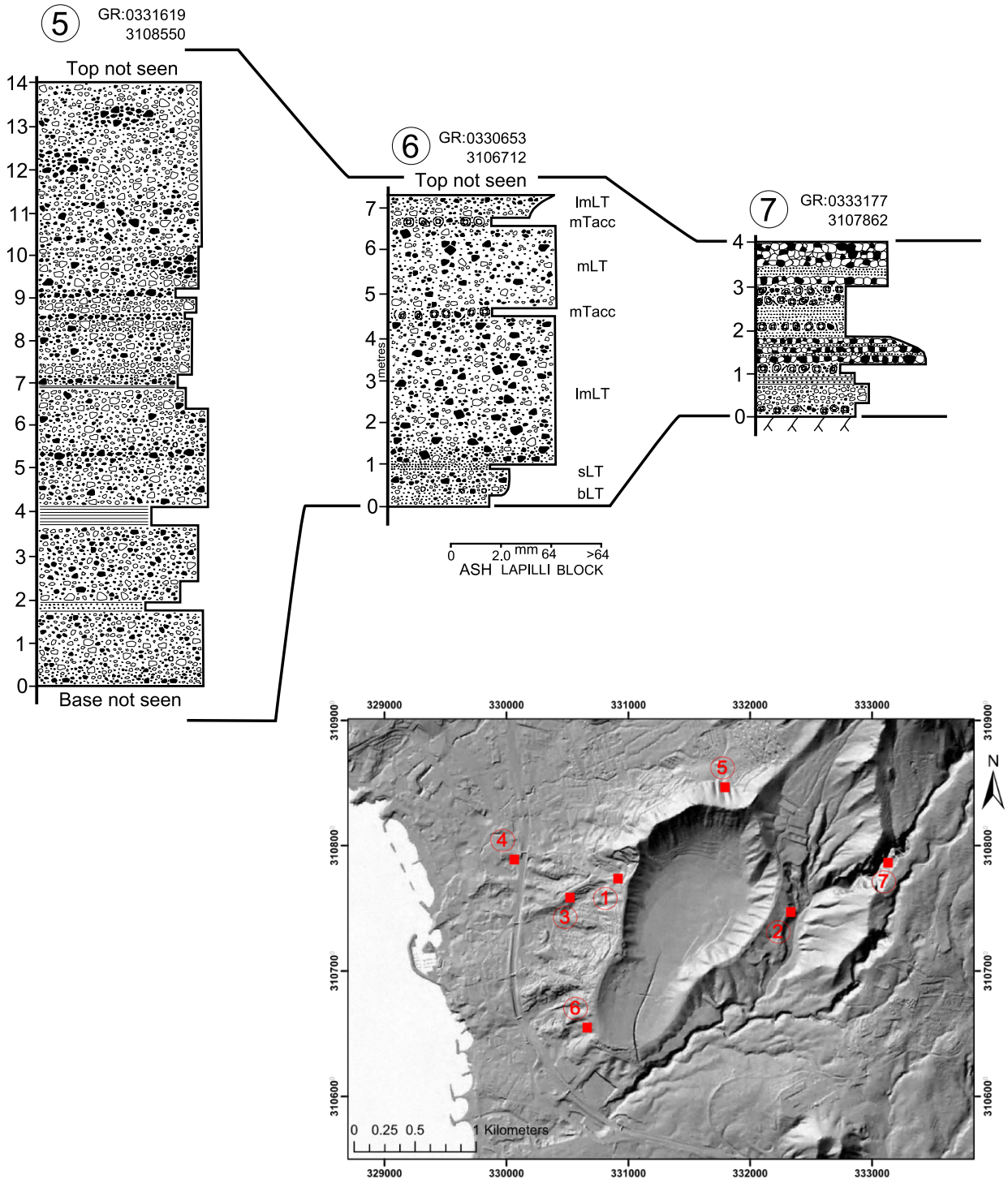

Figure 3.18 *Selected logs from Member D. The deposits were dispersed radially from the northern crater. The lithofacies undergo transitions from proximal deposits to medial deposits (Logs 1–4). Various deposits that overcame topographic barriers are shown (Logs 5 and 7).*

3.5.2 Ash Aggregates

Ash aggregates are moderately abundant and occur matrix-supported and framework-supported (mTacc, mTpel). Accretionary lapilli, coated pellets and ash pellets are present that can either be fully intact or broken fragments. Fining upwards sequences are common.

Accretionary lapilli, typically sub-spherical, are usually found in matrix-supported quantities (10-25%) within bedded, stratified and cross-stratified tuffs. The size of the aggregates average 5–6 mm in diameter (range 3.5–10 mm). The core of the aggregates are often massive, coarse-grained and resemble the matrix of the beds they are found within. The rims of the aggregates, typically 1 to 1.5 mm thick, are composed of multiple concentric layers of fine-grained ash that commonly fine outwards. The accretionary lapilli are generally well preserved.

Coated pellets are the dominant ash aggregate found in Member D. They are typically spherical and are found in matrix to clast supported quantities (10-40%). They contain a single ultra-fine-grained rim around a core of medium to coarse ash. The coated pellets average 4 mm in diameter (range 2–7 mm), with rims commonly 0.5–1 mm thick.

Ash pellets occur in exclusively framework-supported beds (1-4 cm) that occasionally grade up from framework supported coated pellet beds. They are typically spherical, well sorted and make up 30-60% of the deposit. They are composed of fine to medium ash and are typically 1.5 mm in diameter (range 1–3 mm). Ash pellets are commonly poorly preserved.

3.5.3 Medial and Distal Deposits

The medial and distal deposits of Member D vary from the proximal structure outlined above. This is partly due to vertical lithofacies transitions and the palaeotopography. The member thins and fines with distance from the source.

A medial outcrop, 1.5 km from the vent has an overall thickness of 19.7 m (Figure 3.18). The basal 30 cm of this outcrop is composed of thinly bedded fine-grained tuffs (bLT) that thicken into the palaeo-valley. This passes up into very thickly bedded (1-2 m) dbLT. These deposits likely belong to unit 1 of the proximal structure. There is a sharp contact where the deposits transition into thin to medium interbedded layers of bLT, xsLT, sT and mTacc. These deposits gradationally pass upwards into dominantly xsLT and bLT. These deposits likely correlate to unit 2 of the proximal structure.

3.5.4 Barranco del Rey deposits

A distal outcrop of Member D, situated 300 m above the current level of the crater floor, is preserved 1.7 km east of Caldera del Rey, within a section exposed by Barranco del Rey. The outcrop is 120 m long and pinches and swells to a maximum thickness of 4 m. The deposits unconformably rest upon a 0.5 m thick dark cream coloured palaeosol. The deposits are overlain by a dark orange coloured palaeosol that passes up into a 6 m thick, localised mafic lava flow deposit. The outcrop mainly consists of white coloured, fine-grained tuffs (mT) that are commonly ash and coated pellet bearing (mTpel). Lithic-rich, coarse-grained pumice fall deposits (mL) are interbedded. The beds are typically moderately sorted, matrix- to framework-supported and very thinly to medium bedded (1-30 cm).

Pumice clasts are typically sub-angular, ash sized and average <0.5 cm in diameter. Lithic fragments are angular, ash sized and average <0.5 cm in diameter. A fine to medium ash matrix is present that comprises 20-90% of the deposits. Coated pellets are the dominant ash aggregate found within the deposits of this outcrop. Ballistic clasts, <50 cm, composed of mafic lavas and pumice blocks, often have substantial sags. The deposits have an overall thickness of 4 m.

Due to high elevation of the outcrop it does not show the same unit structure to the proximal deposits of Member D. A four unit structure can be identified for this outcrop (Figure 3.18). Unit 1 is 1.39 m thick and consists of stratified, white coloured, fine-grained tuffs that commonly contain coated pellets. This passes in to unit 2 which consists of 0.61 m of lithic-rich pumice fall deposits, interbedded with finer-grained

tuffs. Unit 3, 0.72 m thick, is mainly composed of thinly bedded, stratified fine-grained tuffs. Coated pellet beds are common. 3–4 cm thick, lithic rich fall deposits are interbedded. Unit 4 is 1.17 m thick and consists of predominantly lithic-rich fall deposits interbedded with fine-grained tuffs.

3.6 Member E

Member E comprises fine-grained beds forming xsT, sT and ash aggregate bearing tuffs (mTacc, mTpel). It has a maximum preserved thickness of 27.5 m. The deposits are generally matrix supported and well sorted. The member is typically a weathered brown colour and bedded (0.2-5 m). It is predominantly composed of ash sized pumice and lithic clasts. Member E is only exposed in the intracaldera areas (Figure 3.1). The member outcrops over 0.26 km^2. Centroclinal dips of between 6° and 40° are recorded that dip northwards.

The member creates an angular unconformity where it infills parts of the southern crater and is plastered up against the older deposits of the Caldera del Rey formation (Figure 3.19). The deposits thin into the angular unconformity.

The contact between Member E and the other members is generally sharp. The member is overlain by fluvial sediments that have infilled the craters.

The pumice clasts are generally sub-rounded, typically make up 15-30% of the deposit, and average 1.5-2 mm in diameter. Larger pumice clasts are occasionally preserved and reach an average maximum size of 4.2 cm. The pumices are typically high density (Chapter 3.9) and microvesicular. Phenocrysts are rare within Member E.

Lithic fragments are angular, make up 10-20% of the deposit, and have an average maximum size of 2 mm in diameter. Larger clasts are occasionally preserved and reach up to 1.5 cm. The clasts are predominantly composed of mafic lavas, of which aphanitic basalt is the most dominant. Porphyritic and vesicular basalt are also abundant.

Member E is predominantly composed of a well sorted, fine-grained ash sized matrix that makes up 40-60% of the deposit. The matrix is generally a dark brown colour and contains sanidine and amphibole crystals.

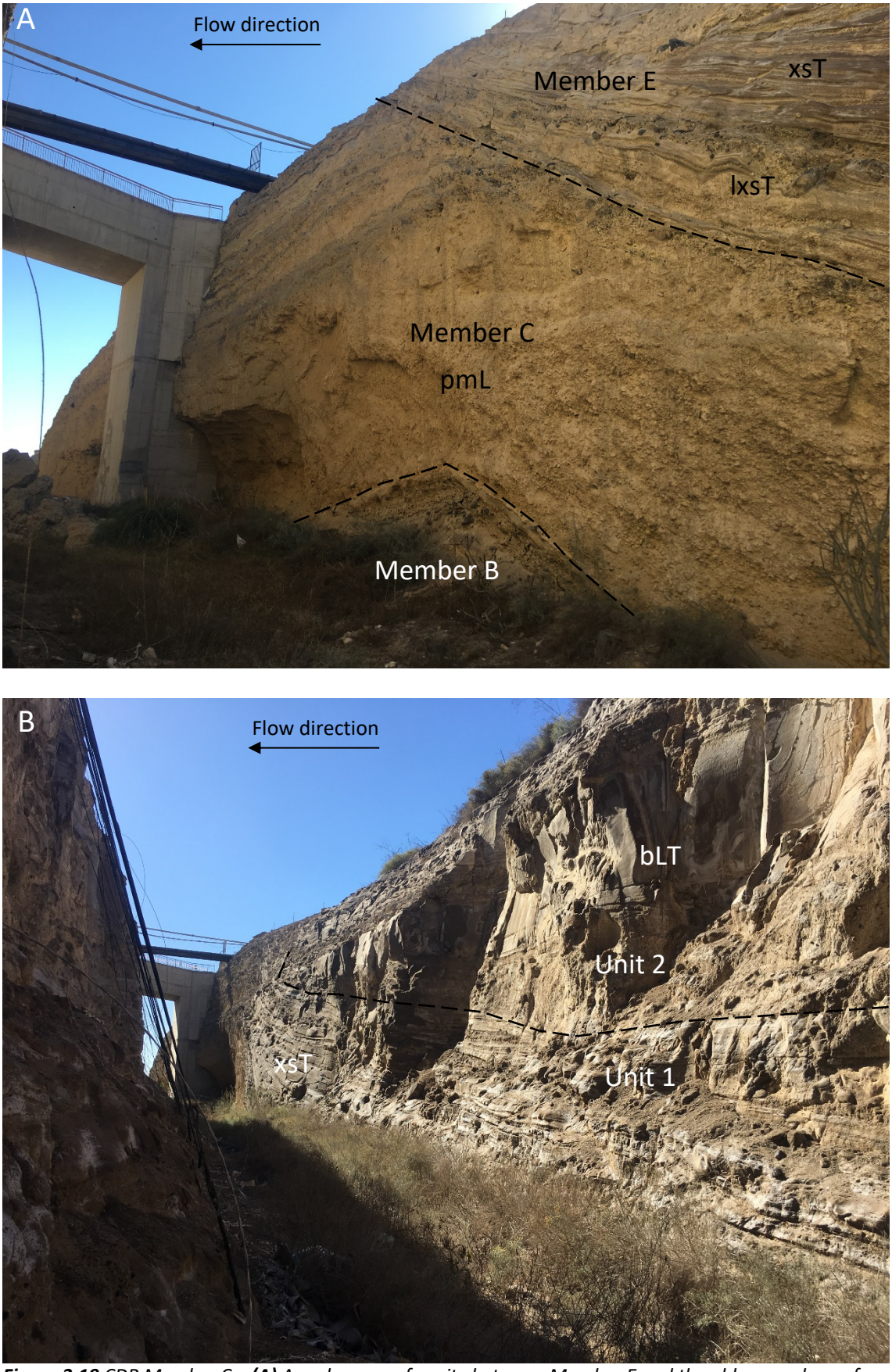

Figure 3.19 *CDR Member C –* ***(A)*** *Angular unconformity between Member E and the older members of the Caldera del Rey formation. Exposed at the old Caldera del Rey entrance road cut (GR: 0331057 3106420).* ***(B)*** *Overview of Member E infilling the southern crater. Concrete bridge is 15.8 m tall.*

Figure 3.19 *(continued) –* ***(C)*** *Lithic rich cross-stratified tuffs (lxsT) that pass into cross-stratified tuffs (xsT) at the base of unit 1.* ***(D)*** *Detailed view of the ash aggregates present in the deposits of unit 1. Rule shows 30 cm.*

A wide variety of structures and bedforms are preserved in the deposits of Member E. Cross-stratification angles range between 7° and 12°. The deposits also show scour surfaces, impersistent bedding, soft-state deformation and evidence of slumping. Parallel stratifications, <0.5 cm thick, are laterally persistent.

3.6.1 Units

Member E has two sub-units that are characteristic of the structure of the member (Figure 3.20).

Unit 1 consists of fine-grained xsT, mTacc and mTpel. The unit is typically medium to thickly bedded (20-80 cm). Ash aggregates are heterogeneously distributed within the beds of unit 1 (Figure 3.21). The unit has a maximum preserved thickness of 10.5 m (Figure 3.20). Unit 1 passes gradationally into unit 2.

Unit 2 is generally composed of sT, bLT and massive ash aggregate tuffs (mTacc, mTpel). The unit is thickly bedded (1-5 m). Pumice-rich horizons, 10–30 cm thick, occasionally occur and contain pumice clasts up to 10 cm in diameter. The unit has a maximum preserved thickness of 17 m (Figure 3.20).

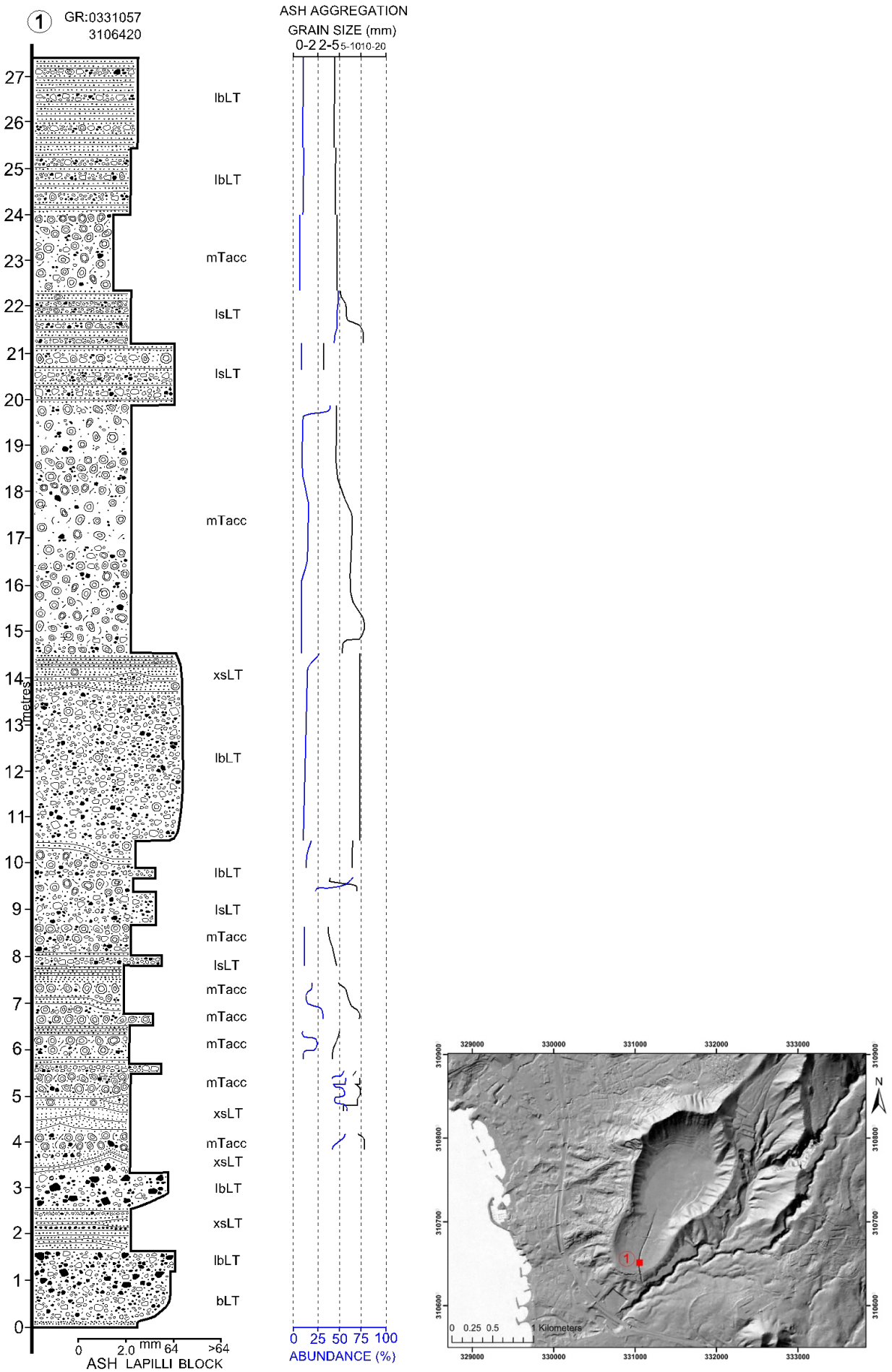

Figure 3.20 *Log from Member E. The variations in the size and abundance of ash aggregates within the member are also shown.*

3.6.2 Ash Aggregates

Ash aggregates are abundant within member E, making up 10-40 % of the deposit when present (Figure 3.21). Coated pellets are the dominant aggregate found, with accretionary lapilli present in lesser concentrations. Fining upwards sequences are common. Lithic fragments, <1 mm, are found in the rims of the aggregates. The aggregates are often fully intact and stand proud from the matrix.

Accretionary lapilli, typically sub-spherical, are matrix supported (10-20%) and occur between 6 and 10 mm in diameter. The core of the aggregates are often massive, coarse-grained and resemble the matrix of the beds they are found within. The rims, <1 mm thick, are made up of multiple concentric layers of fine-grained ash that fine outwards.

Coated pellets with a single ultra-fine-grained rim are matrix to clast supported (20-40%). They are generally spherical, average 4 mm in diameter, with rims commonly 0.5 mm thick. The coated pellets are found alongside accretionary lapilli as well as in individual packages. Ash pellets are absent in Member E.

3.6.3 Distal Deposits

The deposits of Member E are exclusively exposed in intra-crater sections (GR: 0331057 3106420). It is likely that some parts of the member were originally deposited beyond the crater walls but were not preserved.

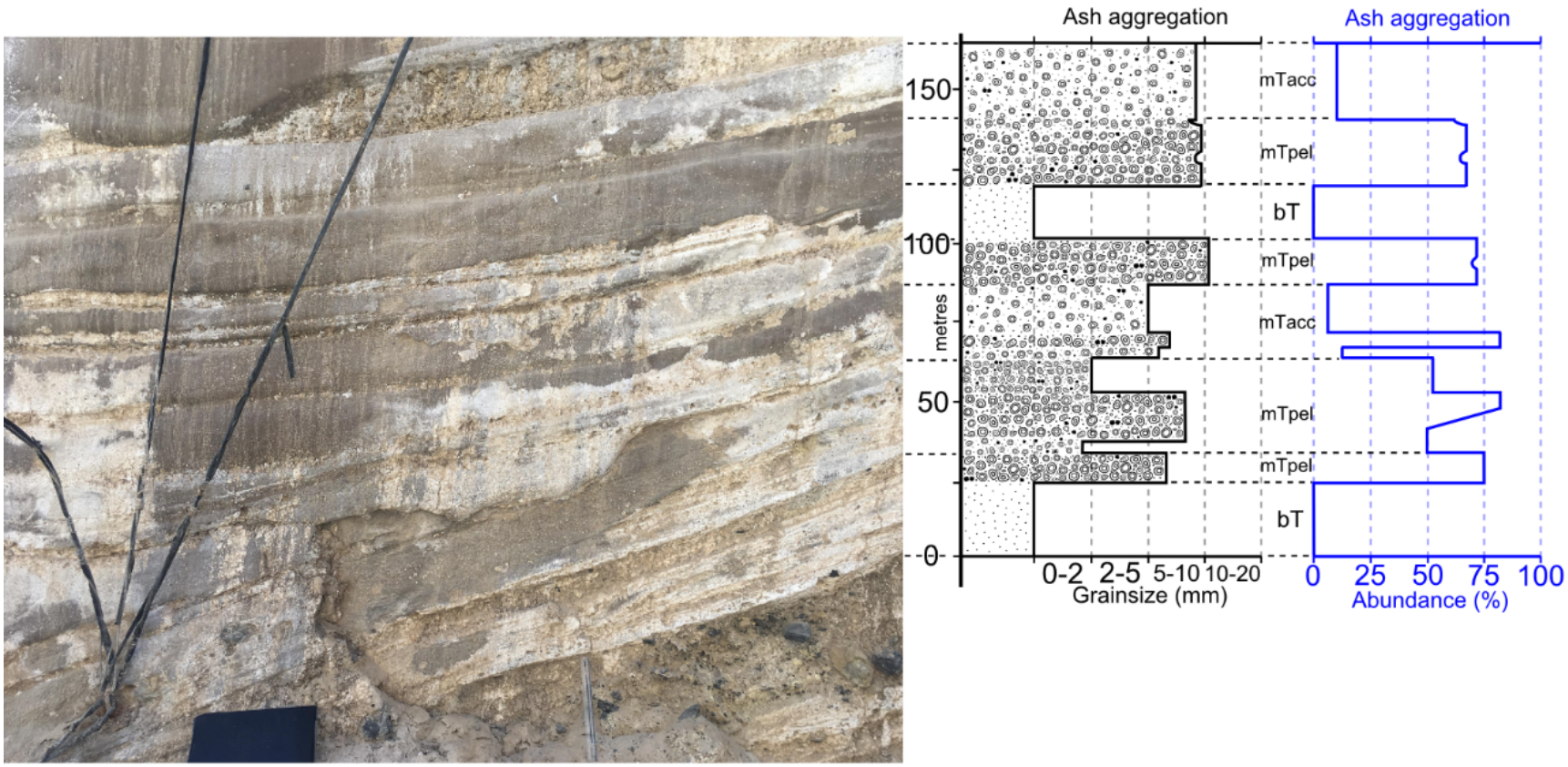

Figure 3.21 *Member E ash aggregation. Detailed log showing variations of ash aggregates at the base of Member E.*

3.7 Distal Outcrops

3.7.1 Fañabe Beach

A distal outcrop of the Caldera del Rey formation is exposed 2.5 km west of Caldera del Rey, at the northern end of Fañabe beach (GR: 0329068 3108273). The outcrop is 35 m long and 6 m tall. The outcrop has a sinusoidal shape (Figure 3.22). The deposits unconformably rest upon a dark brown coloured massive ignimbrite that passes upwards into an orange coloured palaeosol that varies in thickness between 0.2–1 m. The deposits are overlain by a 3-4 m thick, fine-grained, white coloured massive ignimbrite. The outcrop shows CDR Members A – D (Figure 3.23). The contacts between the members are often sharp. The outcrop is determined to represent Caldera del Rey deposits due to the sequence of the members encountered and the correlation with other distal of the same members.

CDR Member A has an overall thickness of 1.17 m. Units 1 and 2 share a combined thickness of 0.92 m. Unit 3 measures only 0.25 m thick, with the top 10 cm grading normally into the top contact. The overall grainsize of the member is finer, with the average maximum thickness of the pumice clasts 1.5 cm and the lithic fragments 1.1 cm.

CDR Member B has an overall thickness of 1.42 m. Unit 1 measures 0.55 m and contains up to 50% coated pellets and accretionary lapilli that reach an average maximum size of 4.5 cm. Units 2 and 3 have thicknesses of 0.15 m and 0.11 m respectively. Unit 4 has a thickness of 0.61 m and is thinly bedded (6–9 cm). Sharp contacts are observed between the different units.

CDR Member C has an overall thickness of 3.77 m. Unit 1, 2.5 m thick, is thinly to medium bedded (3–20 cm). Individual beds show coarsening upwards sequences and variations in pumice abundance. Unit 2 measures 1.27 m thick. The average maximum size of the pumice and lithic fragments are 1.9 cm and 1.3 cm respectively.

Only the basal beds of CDR Member D are exposed and have a minimum thickness of ~2 m. The first 0.77 m are composed of interbeds of prominent fine-grained mTacc and

less prominent coarser-grained bLT. These beds resemble those observed in western medial locations (Figure 3.15A). They are typically thin to medium bedded (4.5–35 cm) and occasionally contain 1 mm thick stratifications. Accretionary lapilli are found between 3 and 10 cm and make up 30–70% of the deposit. Pumice and lithic clasts are found up to 1.5 cm. The beds maintain the sinuous shape of the outcrop. This is overlain by thin to medium bedded, sT, xsT and bLT. The average maximum size of the pumice clasts increases to 3 cm. The beds are parallel bedded and infill the space created by the sinuous shape of the underlying deposits. This creates an erosional contact within the some of the beds of Member D.

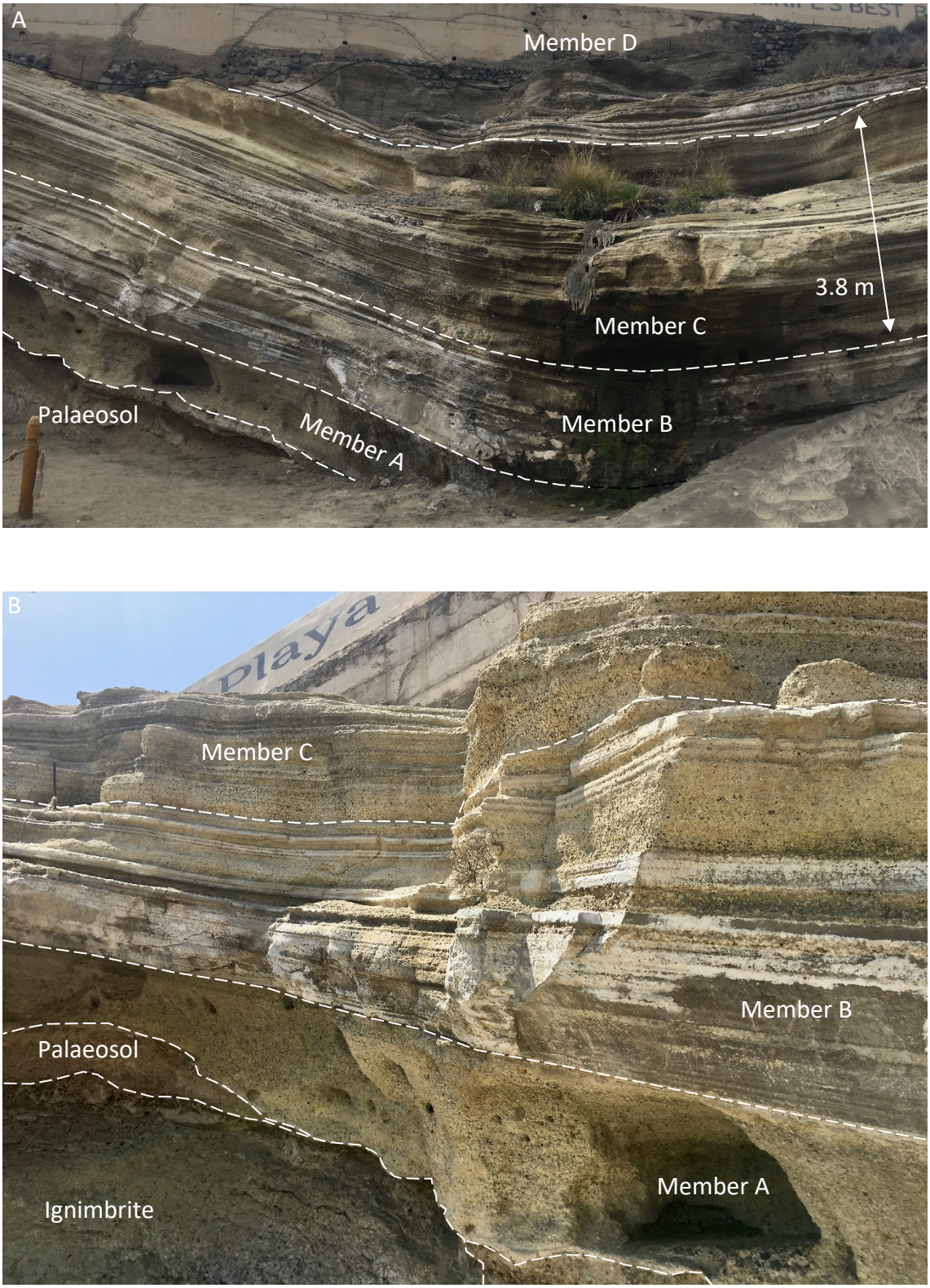

Figure 3.22 *Distal outcrop of the Caldera del Rey Formation – **(A)** Overview of the outcrop at the northern end of Playa de Fañabe beach. Note the sinuous shape of the outcrop. (GR: 0329068 3108273). **(B)** Detailed view of CDR Members A-C that unconformably overlie a massive ignimbrite and palaeosol.*

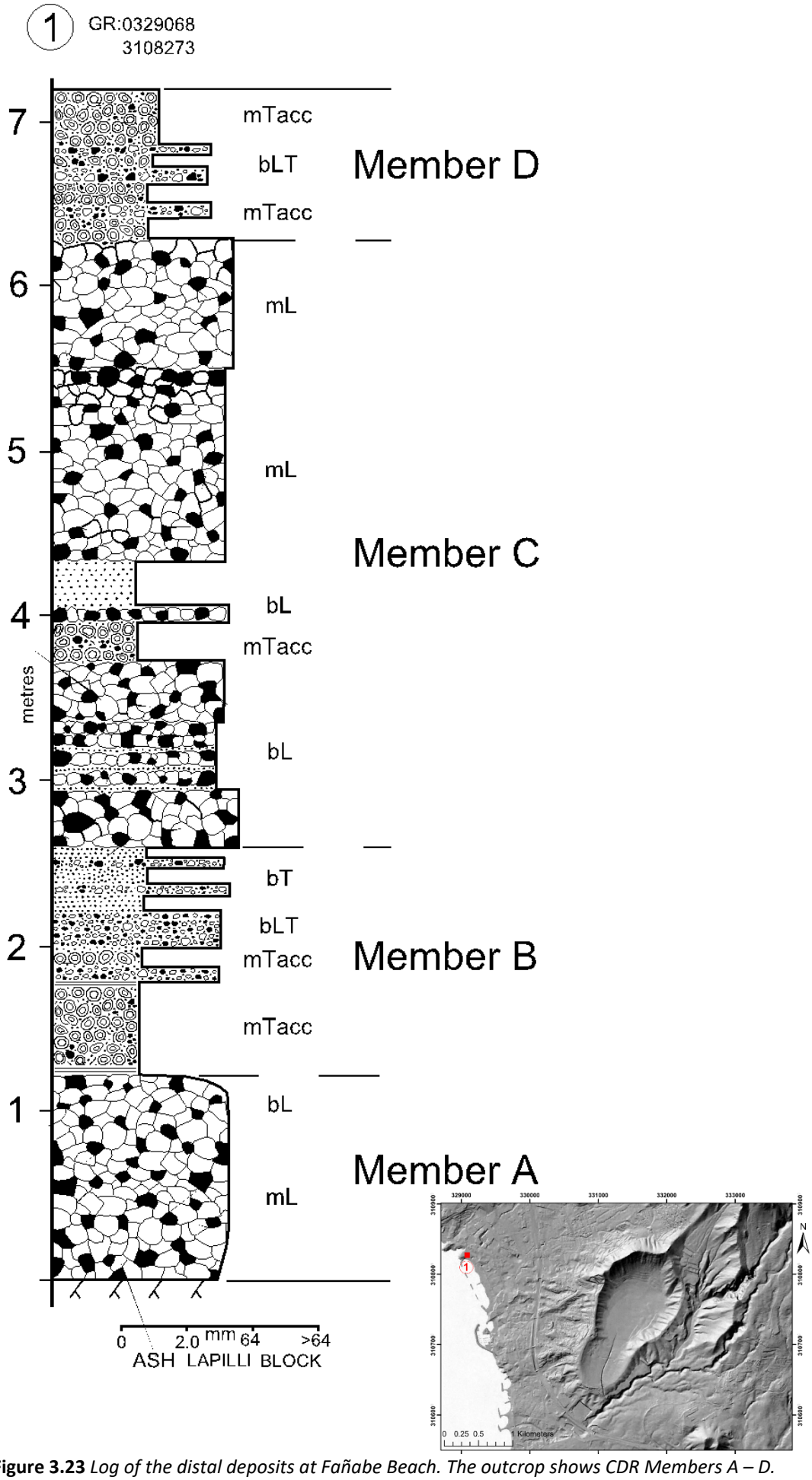

Figure 3.23 *Log of the distal deposits at Fañabe Beach. The outcrop shows CDR Members A – D.*

3.7.2 North of Montaña Guaza

A distal outcrop of the Caldera del Rey formation is exposed 3.9 km east of Caldera del Rey, north of the Montaña Guaza (GR: 0334235 3104847). The outcrop is 40 m long and 5 m tall. The deposits are parallel stratified (Figure 3.24). The deposits unconformably rest upon fluvial gravels that pass into a soil. The deposits are immediately overlain by reworked material that is laterally impersistent. Subsequently, this is overlain by a light cream coloured massive ignimbrite that belongs to the Tosca Formation. Individual members cannot be distinguished. However, it is likely the deposits are primarily composed of CDR Member D due to the similarity with the deposits of this member observed east of Caldera del Rey (Figure 3.15F).

The Caldera del Rey deposits have an overall thickness of 0.88 m. The basal 10 cm of the deposits are comprised of thin to medium bedded layers of sT that are composed of fine to medium ash. Rare amounts of coated ash pellets are found up to 2mm in diameter and make up <50% of the deposit. This passes into an 8.5 cm thick package of mT. This is overlain by 6 cm of sT. These layers are composed of very fine and fine ash and are found between 0.2–1.3 cm thick. This is followed by 17.5 cm of ash aggregate bearing tuffs. The base of this bed is primarily composed of accretionary lapilli which are up to 5 mm in diameter and make up <25% of the deposit. This grades upwards into an ash pellet-rich top which is framework-supported and contains rare accretionary lapilli found up to 8 mm in diameter.

The following 17 cm is composed of sT. These layers are composed of very fine and fine ash and are found between 0.5-2 cm thick. This passes into a 20 cm thick package of sT that are 3–4 cm thick. The final 9 cm comprise of a mT that is composed of medium ash and contains weak stratifications.

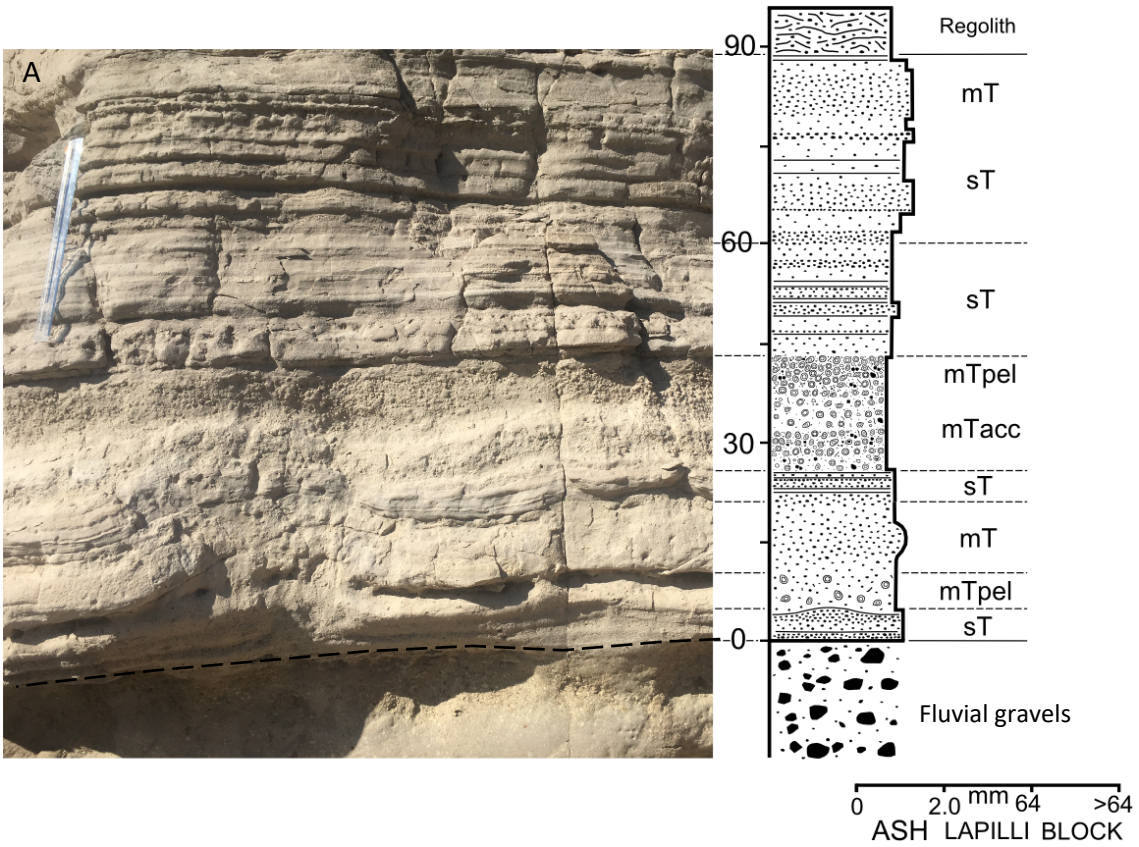

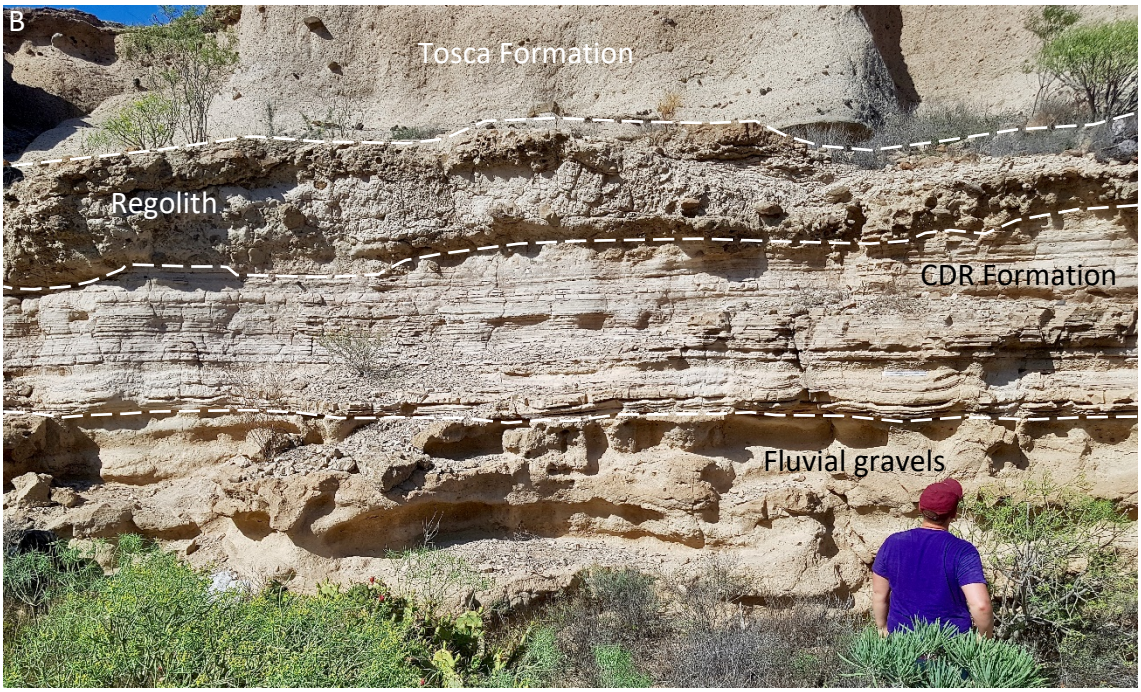

Figure 3.24 *Distal outcrop of the Caldera del Rey Formation north of Montaña Guaza –* ***(A)*** *Detailed view of the distal facies of the Caldera del Rey Formation. Rule shows 30 cm. (GR: 0334235 3104847).* ***(B)*** *Overview of the outcrop. The Caldera del Rey Formation unconformably overlies fluvial gravels and is overlain by reworked deposits that pass into the Tosca Formation (Dávila Harris, 2009). Photo credits: Richy B.*

3.8 Lithic Fragments

Lithic fragments are abundant in the Caldera del Rey formation. They are often angular, ash to block sized and poorly sorted. Nine different types of lithic fragments are found in varying abundances within the formation (Table 3.3). The deposits from the southern crater often contain a greater volume of lithic fragments. It is likely that many of the larger blocks were emplaced as ballistic projectiles (see section 3.12).

The dominant lithic fragments present throughout the formation are aphanitic basalt (33–48%), porphyritic basalt (10–12%) and ankaramite (15–18%) (Figure 3.25). Red scoria (<7 %), amygdaloidal basalt (<8%) and vesicular basalt (<7%) occur in lower abundances. At the base of the formation there is an increased abundance of ignimbrite fragments from the Adeje Formation (Dávila Harris, 2009), whereas at the top of the formation welded ignimbrites become more abundant (Figure 3.25).

Lithic fragment	Description	Interpretation
Aphanitic basalt	Mafic black coloured (melanocratic); aphanitic groundmass; equigranular	likely originates from 'Old Basaltic series' (Fúster et al., 1968)
Porphyritic basalt	Mafic black coloured (melanocratic); porphyritic; subheadral phenorcysts; pyroxene phenocrysts, <5–10% of the rock, <3 mm; plagioclase feldspar phenocrysts, 5–10% of the rock, <5 mm, elongate; aphanitic to fine-grained phaneritic groundmass	likely originates from 'Old Basaltic series'
Ankaramite	Mafic black coloured (melanocratic); porphyritic; subheadral phenorcysts; pyroxene phenocrysts, <10–15% of the rock, <4 mm; olivine phenocrysts, 5–10% of the rock, <5 mm, elongate, often altered; aphanitic groundmass	likely originates from 'Old Basaltic series'
Adeje Formation	Orange coloured, crystal-rich, partly welded ignimbrite (Davila-Harris, 2009)	Derived from underlying, pre-dating pyroclastic units that were dispersed close to Adeje, west of Caldera del Rey (Davila-Harris, 2009)
Red scoria	Mafic red coloured; abundant vesicles (40–60%), variable size; aphanitic solid portions; frothy textured	Likely originates from localised scoriaceous basalt that belongs to the 'Old Basaltic series'

Amygdaloidal basalt	Mafic black coloured (melanocratic); equigranular; aphanitic groundmass; vesicular; amygdular texture, amygdales of zeolites and carbonates	likely originates from 'Old Basaltic series'
Vesicular basalt	Mafic black coloured (melanocratic); equigranular; aphanitic groundmass; vesicular, <30-60% of the rock, < 8 mm	Likely originates from 'Old Basaltic series'
Welded ignimbrite	Cream/dark brown coloured; welded ignimbrite; slight eutaxitic texture, stretched mafic minerals, aspect ratios <1:10; can contain green coloured, eutaxtitic, pumice fiamme	Likely derived from underlying, pre-dating pyroclastic units
Phonolite	Brown/green coloured; mingled texture; intermittent mafic streaks	Likely derived from localised phonolite lavas

Table 3.3 *Summarised description and interpretation of the lithic fragments present within the Caldera del Rey formation.*

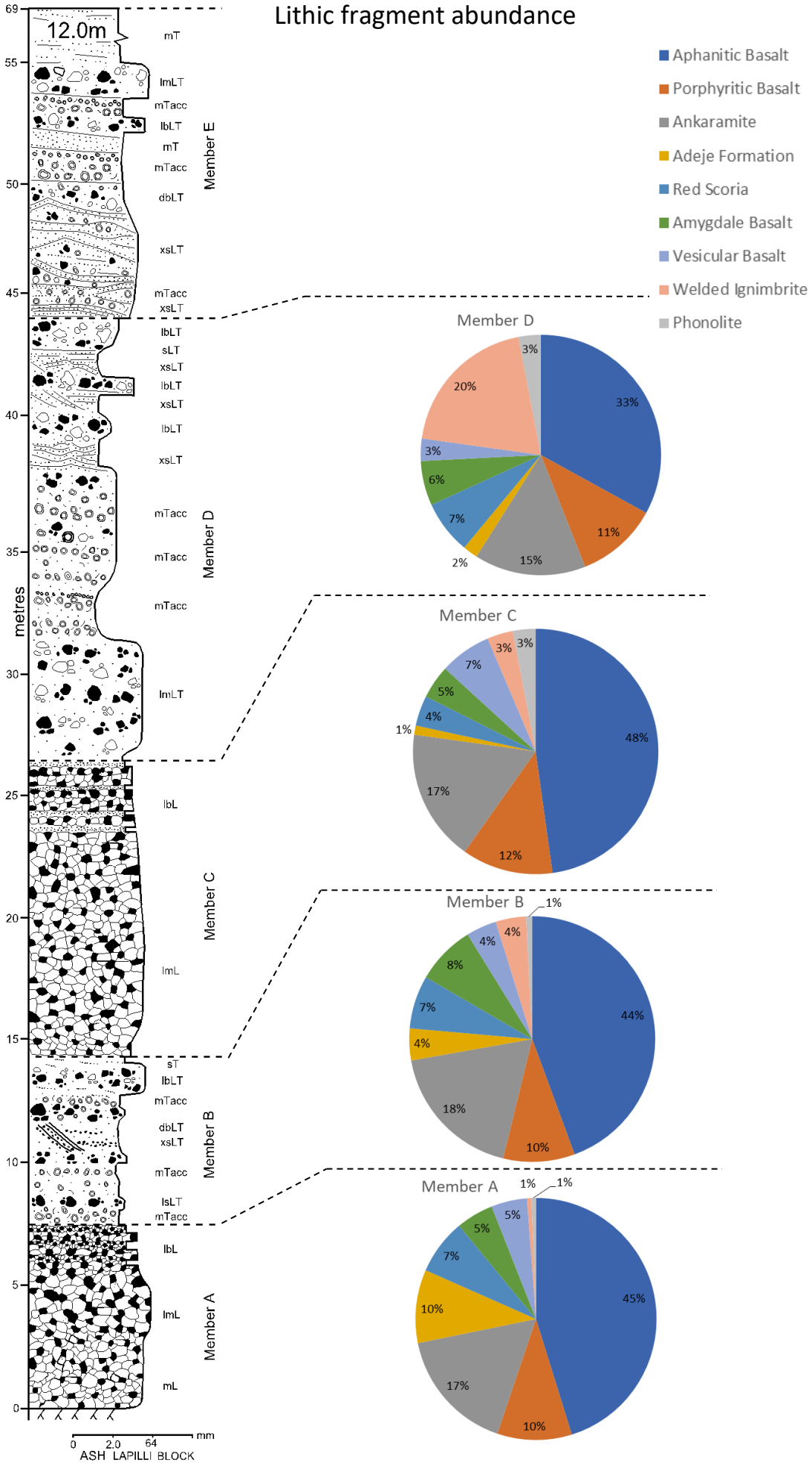

Figure 3.25 Variations of the lithic clast abundance through the Caldera del Rey formation.

3.9 Pumice Densities

The density and the vesicularity of the pumice clasts show changes between eruption styles and upwards variations through the Caldera del Rey formation. The lower the average density of the clasts, the higher the average vesicularity, and vice versa. Members A and C have the lowest average densities of 0.56 and 0.62 g/cm^3, respectively, and have a unimodal distribution (Table 3.4; Figure 3.26). Members B, D and E have a broad range of density values and have average density values that are significantly higher than Members A and C (Table 3.4).

The density and vesicularity curves (Figure 3.26) show an overall upwards trend towards higher density, lower vesicularity values. Additionally, two phases showing trends of increasing density upwards can be picked out (Figure 3.26). The first phase is recorded in Members A and B that originated from the southern crater. A density decrease is observed between Members B and C, before a second general increasing density trend is present in Members C, D and E that were erupted from the northern crater.

	Member A	Member B	Member C	Member D	Member E
Mean density (g/cm^3)	0.56	0.69	0.62	0.99	0.93
Maximum density	1.07	1.61	1.64	2.17	2.04
Minimum density	0.33	0.32	0.36	0.49	0.34
Mean vesicularity (%)	75	67	72	52	55
Maximum vesicularity	86	86	85	79	86
Minimum vesicularity	55	32	31	9	14

Table 3.4 *Density and vesicularity values for the pumice clasts of the Caldera del Rey formation.*

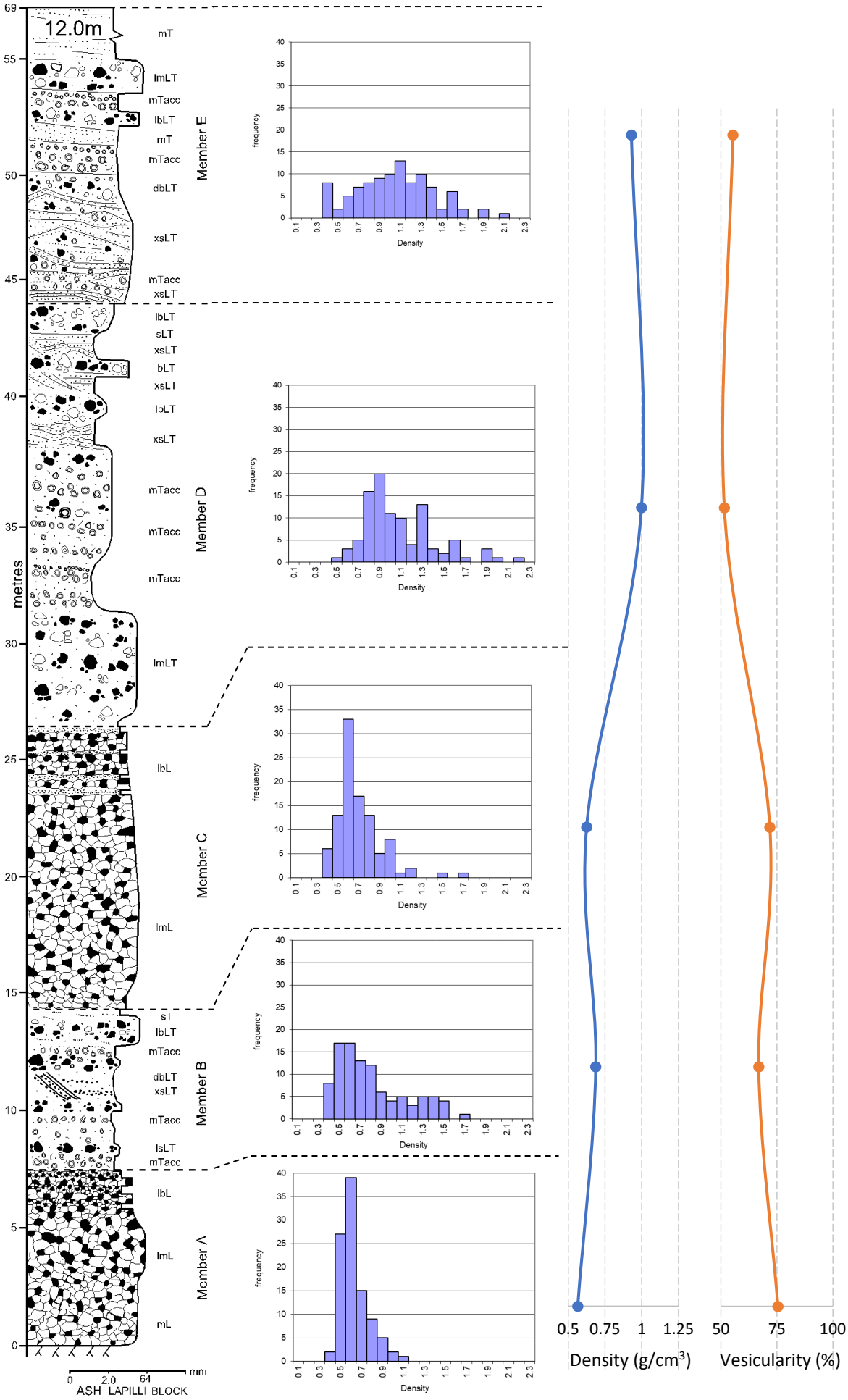

Figure 3.26 *Variations in the density of pumice clasts throughout the Caldera del Rey formation.*

3.10 Ballistic Projectiles

Volcanic ballistic projectiles are common in the Caldera del Rey formation and present a potentially fatal hazard close to erupting vents (Yamagishi and Feebrey, 1994; Waitt et al., 1995; Williams et al., 2017). Ballistic projectiles are most abundant in Unit 3 of Member B and throughout Member D, with up to 35 clasts per square metre. The deposits from the northern crater contain the largest blocks (up to 2.5 m) compared to the southern crater (up to 1.4 m), with 13 blocks over 1 m in diameter. They are also found at a greater distance from the vent in the northern crater (1.6 km) compared to the southern (1 km). The size of the ballistics varied between lapilli and blocks (0.05–2.5 m) and decreased in size, alongside their spatial density, with distance from the vent (Figure 3.27).

Ballistic projectiles were identified by their often block size (>64 mm), blocky shape, anomalous size with respect to surrounding clasts and impact sags. The ballistic projectiles were predominantly composed of mafic lavas (90%) and pumice (10%).

The composition of the mafic ballistic blocks is similar to the lithic fragment population (see section 3.10) with aphanitic basalt (50%), porphyritic basalt (11%) and ankaramite (12%) the most common.

The limited exposure of Members A and B restricted the data points of ballistic projectiles from the southern crater to 23. The ballistic projectiles derived from the southern crater are found up to a maximum range of 1 km from the vent and average 42 cm in diameter. The largest block, 1.4 m in diameter, can be found 0.69 km from the source.

Given the great exposure of the deposits from the northern crater, 683 data points were collected, and a study was undertaken within these members to determine the eruptive processes of the ballistic blocks for the entire Caldera del Rey eruption. The ballistic projectiles ejected from the northern crater are at distances of 0.65 km to 1.6 km from the vent (Figure 3.28). They have an average size of 0.22 cm (Table 3.5). The largest block, 2.5 m in diameter, is situated 0.75 km from the vent. The calculated initial velocity,

volume and mass for the largest and average blocks observed are presented in Table 3.5.

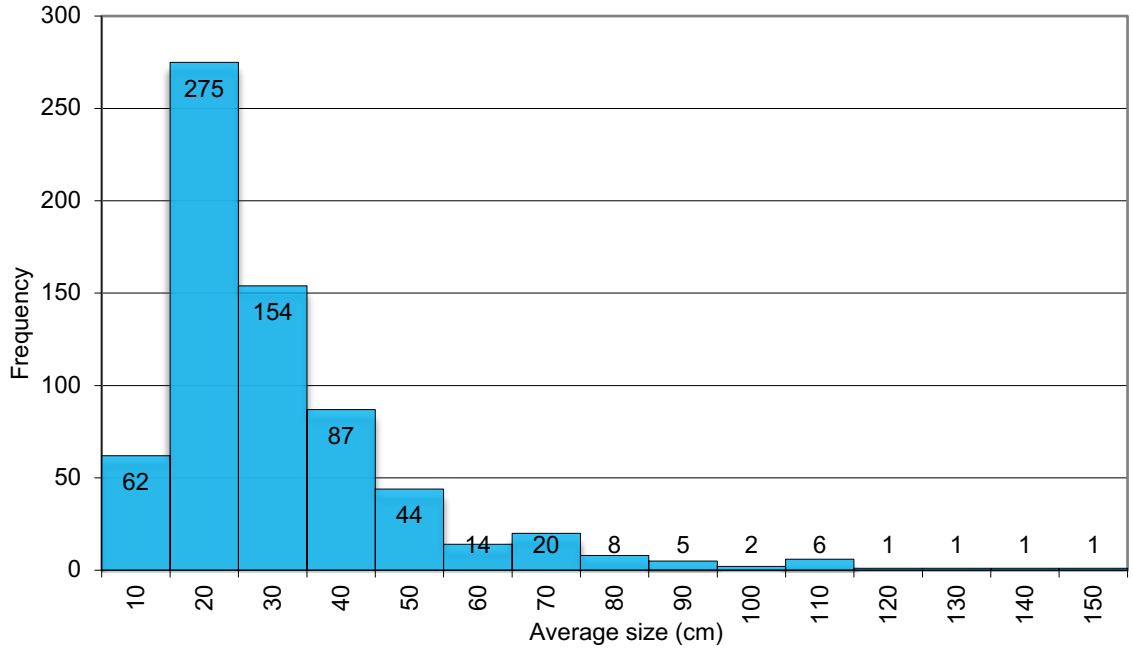

Figure 3.27 *Graph showing the number of ballistic projectiles measured for a given size from the northern crater.*

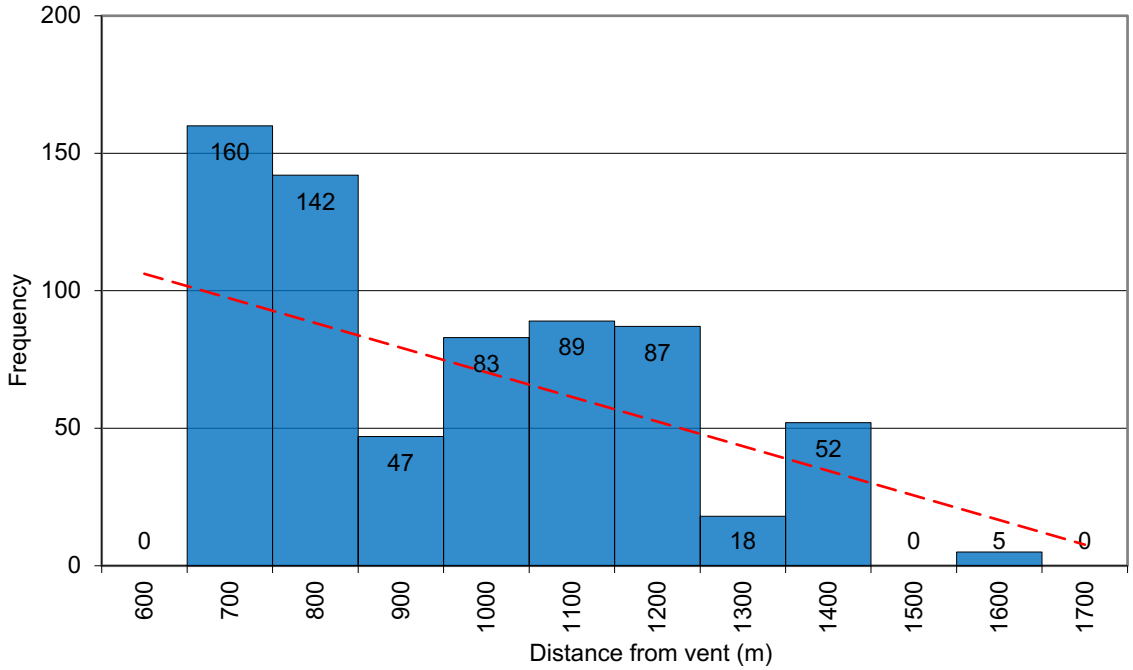

Figure 3.28 *Graph showing the number of ballistic projectiles measured in relation to their distance from the vent for the northern crater. The red trendline shows a decrease in abundance with distance from the vent.*

	Largest block	Minimum block	Average size
Bomb size (m)	2.5	0.05	0.22
Distance from vent (km)	0.75	1.37	0.92
Initial velocity (m s^{-1})	92	152	102
Density (g/cm^3)	2.7	2.7	2.7
Volume (m^3)	15.63	1.25 x10^{-4}	0.01
Mass (kg)	42, 200	0.338	27.3

Table 3.5 *Ballistic projectile characteristics for the deposits of the northern crater.*

Chapter 4: Interpretation

4.1 Member A

Member A records the first deposits of the Caldera del Rey formation and the southern tuff ring. The member comprises pumice fallout deposits from a sustained plume that is classified close to subplinian. The clast-supported nature, constant thickness and the mantling of topography confirms the deposits are of air fall origin, which suggests this was a fairly dry phase of the eruption.

The first deposits of the eruption are much finer grained than the main body of the eruption. This suggests the eruption column was at a lower height initially. As the column height rose and the eruption intensified, the grainsize increased and thickly bedded pumice rich fall deposits were deposited (units 1 and 2). These most likely originated from a steady sustained umbrella cloud. These pass into closely bedded, lithic-rich deposits that are found within unit 3 of this member. This is the result of fluctuations of the sustained eruption column. These fluctuations could be caused by changes at the source, which has the potential to control the lithic abundance and the column height. Sharp increases in the abundance of lithic fragments have been directly associated with increases in the amount of external water available to the eruptive system (Houghton and Smith, 1993). Additionally, the bedding may be caused by subtle changes in the wind direction that causes changes to the main dispersal axis of the eruption plume.

A main dispersal axis towards the southwest, trending at roughly 275°, is calculated from isopach maps (Figure 4.1). The rapid thinning of the deposits shown in the isopach maps is reflective of the cone-shaped structure (Figure 4.2). Isopleth maps constructed from pumice clasts are dispersed across a greater area than the lithic fragments. Similarly, pumice clasts of a given size reach a greater distance from the vent than lithic fragments of the same size (Figure 4.3). This reflects the greater influence of the wind on the lower-density pumice clasts compared to the denser lithic fragments (Francis and Oppenheimer, 2004).

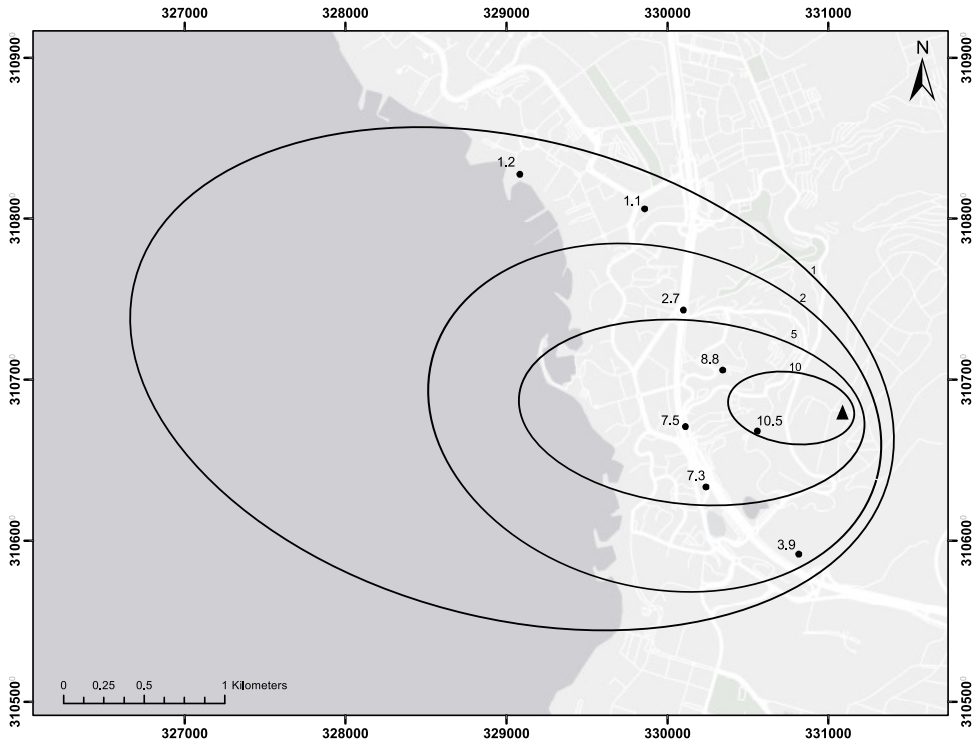

Figure 4.1 *Member A isopach map*

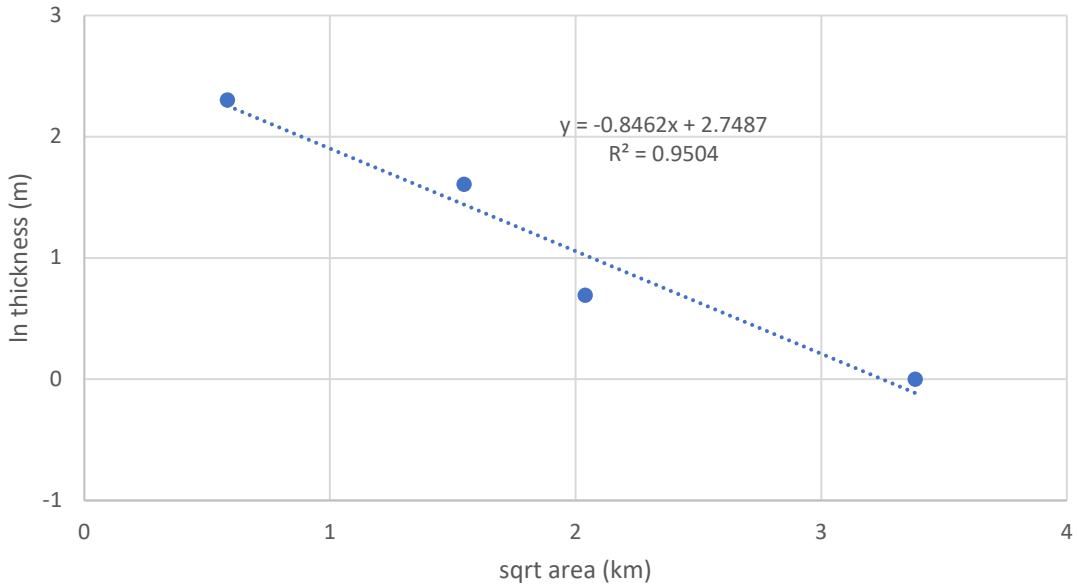

Figure 4.2 *Plot of the square root of the area against the natural logarithm of the thickness, derived from isopach maps under normal wind conditions (Fig. 4.4A). The gradient of the slope is equivalent to the thinning constant (K).*

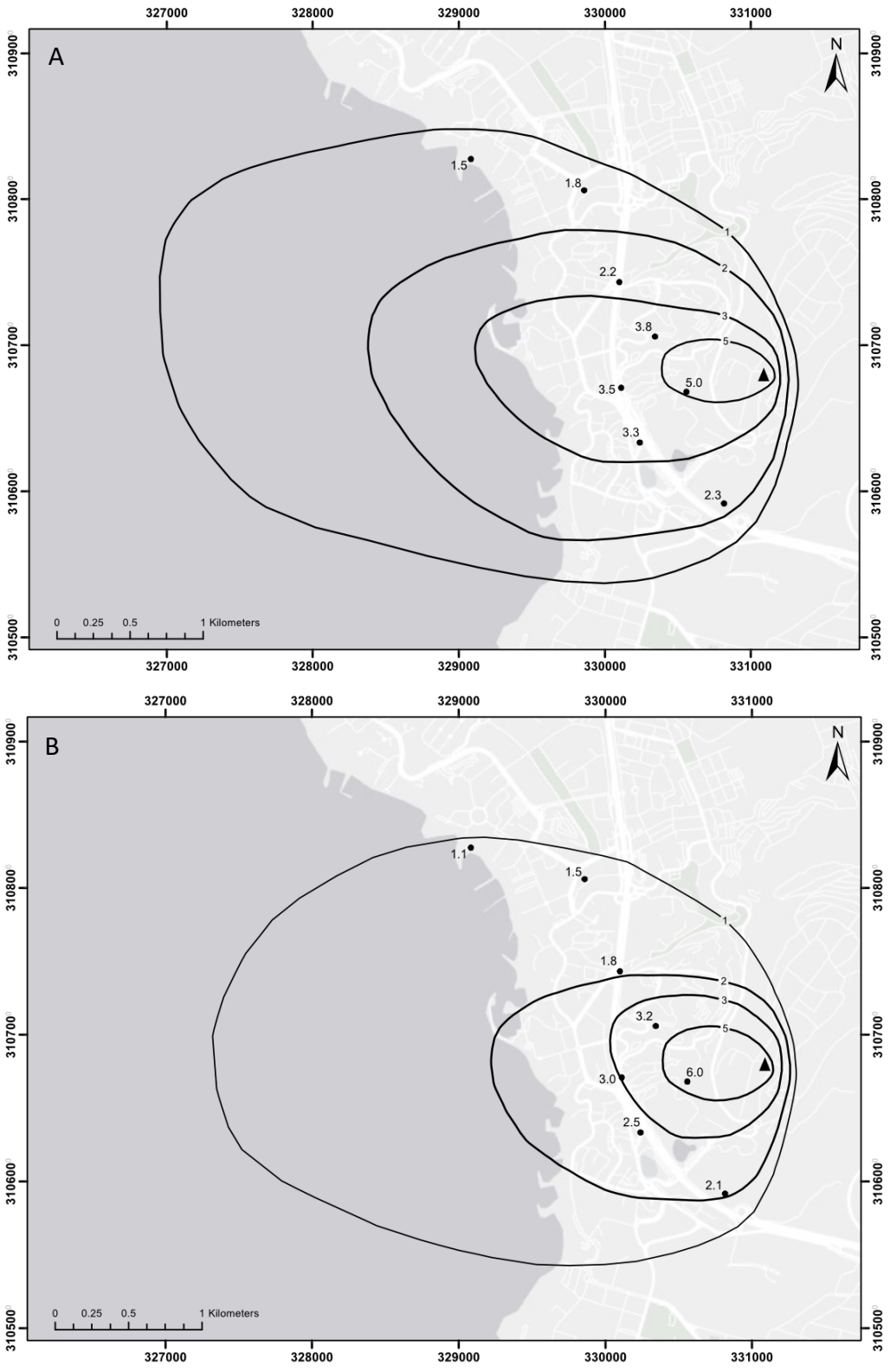

Figure 4.3 *Member A isopleth maps – **(A)** Pumice clast isopleth map **(B)** Lithic clast isopleth map.*

Using the estimated volumes from the isopach and isopleth maps, the eruption parameters for the Member A pumice fall are estimated (Table 4.1) (Pyle, 1989). An eruption speed of 102 m^3 s^{-1} is estimated, which is equivalent to 2.42 x 10^5 kg s^{-1}. The eruption corresponds to a VEI 3 eruption. The plume is estimated to have reached a

maximum height (H_T) of 5.53 km (Pyle, 1989). This classifies the plume close to subplinian (Figure 4.4).

The roughly elongated nature of the isopach and isopleth maps likely reflects the influence of the wind in directing the eruption plume downwind. Additionally, the lack of upwind deposits suggests that the plume may have been bent over. The low level of the umbrella cloud, below the tropopause, allows the plume to be subject to strong winds that have the potential to cause downwind extension of a plume (Francis and Oppenheimer, 2004).

Eruption Parameter	Value
Bulk tephra volume (km^3)	0.044
Mass (kg)	4.40×10^{10}
DRE volume (km^3)	0.018
Eruption rate ($m^3\ s^{-1}$)	102
Eruption rate ($kg\ s^{-1}$)	2.42×10^5
VEI	3
Maximum plume height (km)	5.53

Table 4.1 *Estimated eruption parameters for the eruption plume that deposited Member A.*

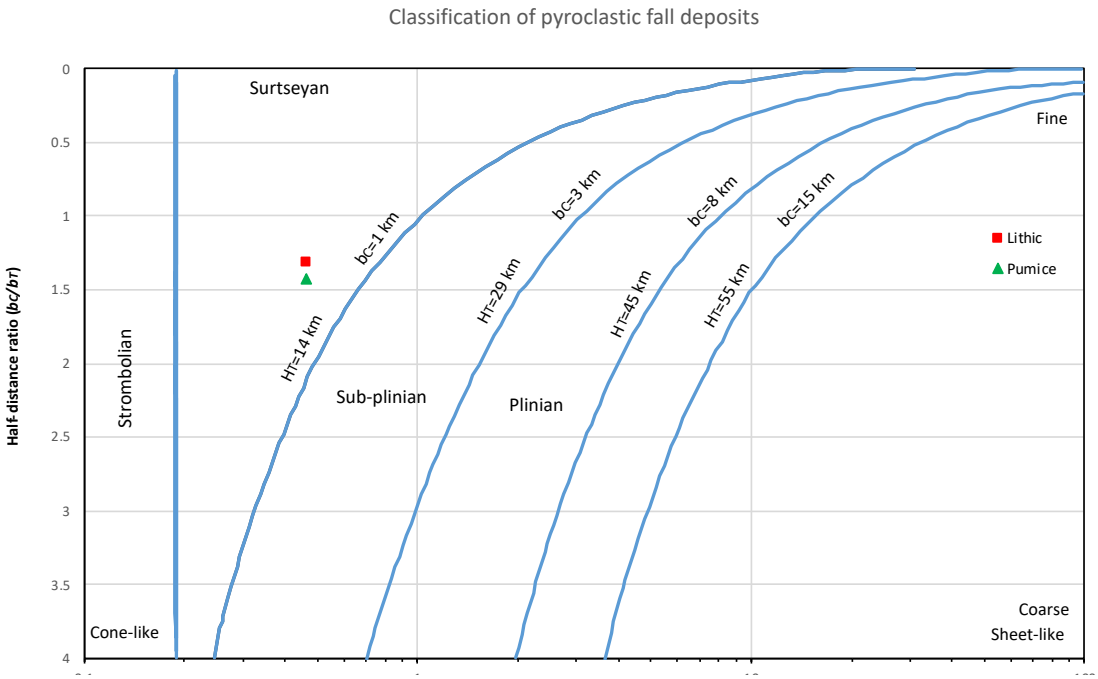

Figure 4.4 *Diagram classifying the pyroclastic fall deposits of Member A. Edited from Pyle (1989). Isopleth volumes were extracted for both lithic and pumice clasts. The differing clast size half distance (b_c) demonstrates the density contrast between the different types of tephra.*

4.2 Member B

The deposits of Member B were erupted from the southern crater and were deposited by multiple closely spaced, depletive, pulsatory, fully dilute pyroclastic density currents. The member is typically composed of fine-grained tuffs with stratified and cross-stratified bedforms, that record a wet phase. The matrix-supported nature, variable thickness, poor sorting and infilling of topography confirms the deposits were produced from pyroclastic density currents.

Unit 1 is composed of xsLT in proximal locations that transition into sT with distance. This unit was deposited from depletive, fully dilute currents with traction-dominated flow-boundary zones. The cross-stratified structures represent areas of localised non-uniformity (Branney and Kokelaar, 2002). The fine-grainsize of the unit is a result of extreme fragmentation that is typical of phreatomagmatic eruptions (Zimanowski et al., 2015).

Unit 2 is composed of bLT and bT. The finer-grained bedded tuffs were likely deposited from fully dilute currents with traction-dominated flow-boundary zones. However, the coarser-grained bedded lapilli tuffs, which are often internally massive, were most likely deposited from higher concentration currents, with granular flow-dominated flow-boundary zones (Branney and Kokelaar, 2002).

Unit 3 is composed of xsLT and dsLT in proximal locations that quickly transition into sT with distance. The proximal deposits were deposited from depletive, close to fully dilute currents with mainly traction-dominated flow-boundary zones. Diffuse-stratification suggests localised transitions towards more granular flow-dominated flow-boundaries (Branney and Kokelaar, 2002). With distance the currents transition closer towards the fully dilute end member (see section 4.9).

Unit 4 comprises beds of mLT and sT. The stratified tuffs were likely deposited from close to fully dilute currents with traction-dominated flow-boundary zones whereas the massive lapilli tuffs were likely produced by closer to granular fluid-based currents with

granular flow-dominated flow-boundary zones. The unit shows alternations between the degree of phreatomagmatic fragmentation. A thin pumice fall deposit may have originated from a small, short-lived plume that originated alongside the phreatomagmatic explosions forming PDCs. Alternatively, the deposit may have originated from the sustained plume that produced Member C and marks the start of the eruption from the northern crater.

The different grainsizes observed in this member, and within units 2 and 4, are often sharp and show abrupt vertical changes in the depositional structures. This is likely controlled by the amount of water available, which controls the degree of phreatomagmatic fragmentation. The fine-grained deposits are produced by high levels of fragmentation during phreatomagmatic eruptions whereas coarser grained deposits result from lower water content eruptions (Zimanowski et al., 2015). The periodic ingress of water into the system could be a result of low groundwater recharge rates (Lorenz, 1986). Many hydrovolcanoes show similar rapid fluctuations between wetter and drier phases (e.g. Ukinrek, Alaska, Self et al., 1980; Crater Hill, New Zealand, Houghton et al., 1996).

The PDCs that deposited Member B were generated following the collapse of the buoyant plume. Considering the phreatomagmatic influence, it is likely the addition of water into the system had an impact on triggering a reduction in plume buoyancy by lowering the plume temperature (Houghton et al., 2015). Fracturing of the country rock and downward migration of the diatreme eruptive explosions may have allowed greater access for water (Ross et al., 2017). Additionally, the increased lithic content observed in unit 3 of Member A could be evidence of the vent widening, which would have reduced the exit velocity and in turn decreasing the likelihood of the plume becoming buoyant (Varekamp, 1993). This process would account for transitional contact observed between Member A and B.

4.3 Member C

Member C records the first deposits erupted from the northern crater. The member comprises pumice fallout deposits from a quasi-sustained, fluctuating plume of almost

subplinian dimensions. The clast-supported nature, constant thickness and the mantling of topography confirms they are ash fall deposits. Similarly, inter-bedded beds of parallel-stratified tuffs likely have an ashfall origin. The fallout origin of this member suggests it was a relatively buoyant phase.

Fractures and jointing have formed in some of the pumice clasts that are found both throughout the pumice clasts and on the outer rims. This is most likely due to impact fracturing on deposition and the formation of thermal fractures during cooling (Patel et al., 2013; Cioni et al., 2015)

Unit 1 was deposited from a southwest dispersed umbrella cloud, trending at roughly 215°, which deposited thickly bedded lithofacies on the main dispersal axis (Figure 4.5) and thinly bedded lithofacies in western areas. It is inferred the western deposits represent the margins of the umbrella cloud where a lower amount of tephra is supplied, and any variations are more pronounced (Francis and Oppenheimer, 2004).

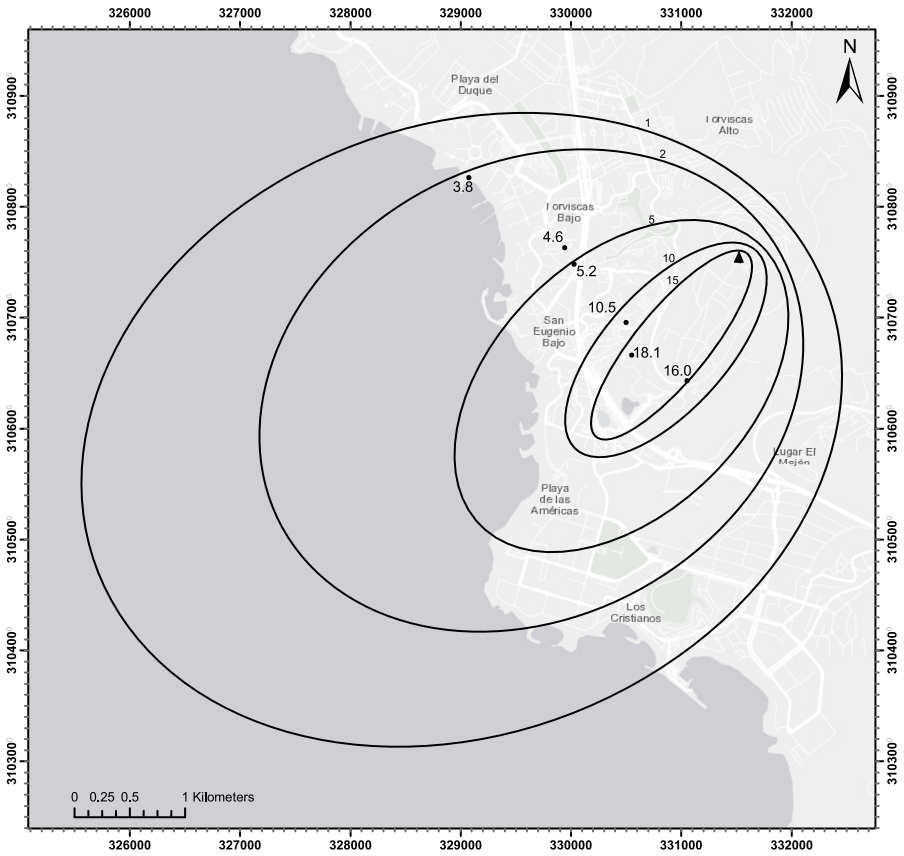

Figure 4.5 *Member C isopach map*

The bedded nature of these deposits is a result of fluctuations in the plume height and changes in the supply at the vent. Sharp lithic-rich and lithic-poor beds may reflect changes in the supply of lithic material at source. Alternatively, the fallout of pumice clasts into small, moderately lithic-rich PDCs may produce lithic-rich beds. Parallel-stratified tuffs represent the intermittent fallout of fine-grained ash or the formation of rolling ash clouds (Branney and Kokelaar, 2002).

The main dispersal axis then shifted westwards, trending at roughly 250°, and produced deposits of unit 2. This is inferred from the greater thickness of deposits in western areas compared to southern areas. The unit was produced from a sustained plume, but internal stratifications reflect the fluctuating height of the plume and changes in the tephra emitted from the vent.

The rapid thinning of the deposits shown in the isopach maps is reflective of the cone-shaped structure observed in the field (Figure 4.5; Figure 4.6). Isopleth maps constructed from pumice clasts are dispersed across a greater area than isopleth maps from lithic fragments, reflecting the greater influence of the wind on the lower-density pumice clasts (Francis and Oppenheimer, 2004).

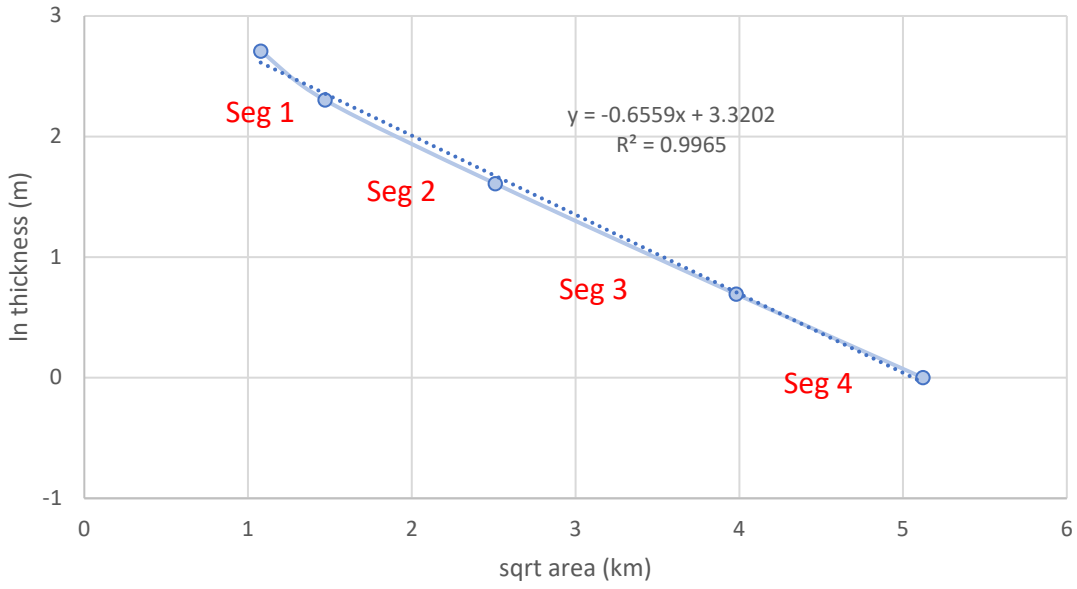

Figure 4.6 *Plot of the square root of the area against the natural logarithm of the thickness, derived from the isopach map. The gradient of the trendline (dotted line) is equivalent to the thinning constant (K). The gradient of the slope for segment 1 is significantly steeper than the other segments. This is a result of the greatest thicknesses being preferentially deposited in proximal regions and is reflective of the cone-shaped morphology of the deposits (Pyle, 1989).*

Using the estimated volumes from the isopach and isopleth maps (Figure 4.7), the eruption parameters for plume that deposited Member C are estimated and presented in . An eruption speed of 249 $m^3\ s^{-1}$ is estimated, which is equivalent to 5.92 x 10^5 kg s^{-1}. The eruption corresponds to a VEI 4 eruption. The plume is estimated to have reached a maximum height (H_T) of 6.97 km (Pyle, 1989). This classifies the plume close to subplinian (Figure 4.8).

The roughly elongated nature of the isopach and isopleth maps suggests the wind had a great influence on directing the eruption plume downwind. Additionally, the lack of upwind deposits and the low level of the umbrella cloud suggests that the plume may have been somewhat bent over.

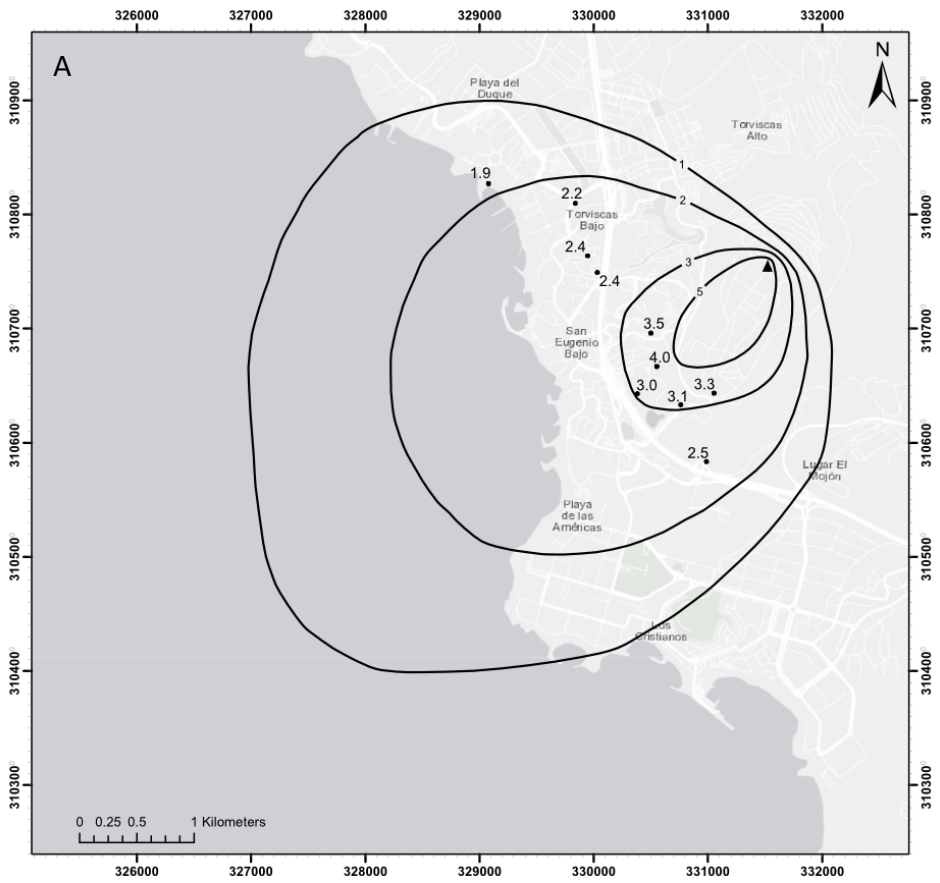

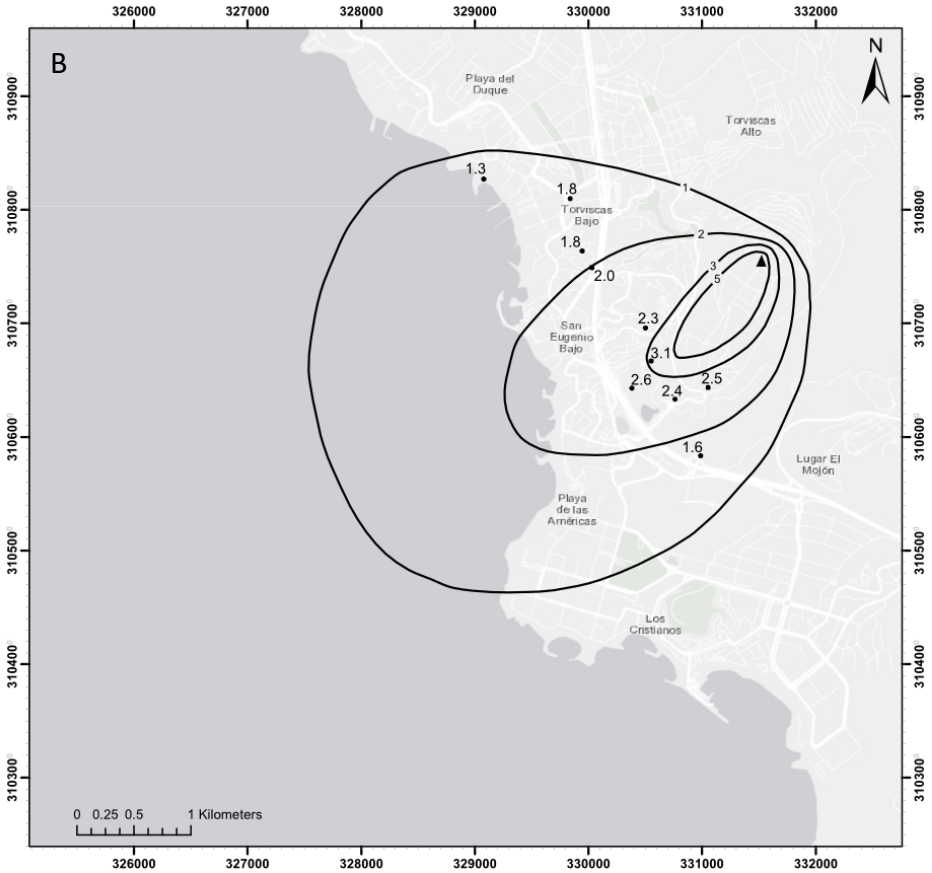

Figure 4.7 *Member A isopleth maps – (**A**) Pumice clast isopleth map **(B)** Lithic clast isopleth map.*

Eruption Parameter	Value
Bulk tephra volume (km^3)	0.129
Mass (kg)	1.29×10^{11}
DRE volume (km^3)	0.054
Eruption rate ($m^3\ s^{-1}$)	249
Eruption rate ($kg\ s^{-1}$)	5.92×10^5
VEI	4
Maximum plume height (km)	6.97

Table 4.2 Estimated eruption parameters for the eruption plume that deposited Member C.

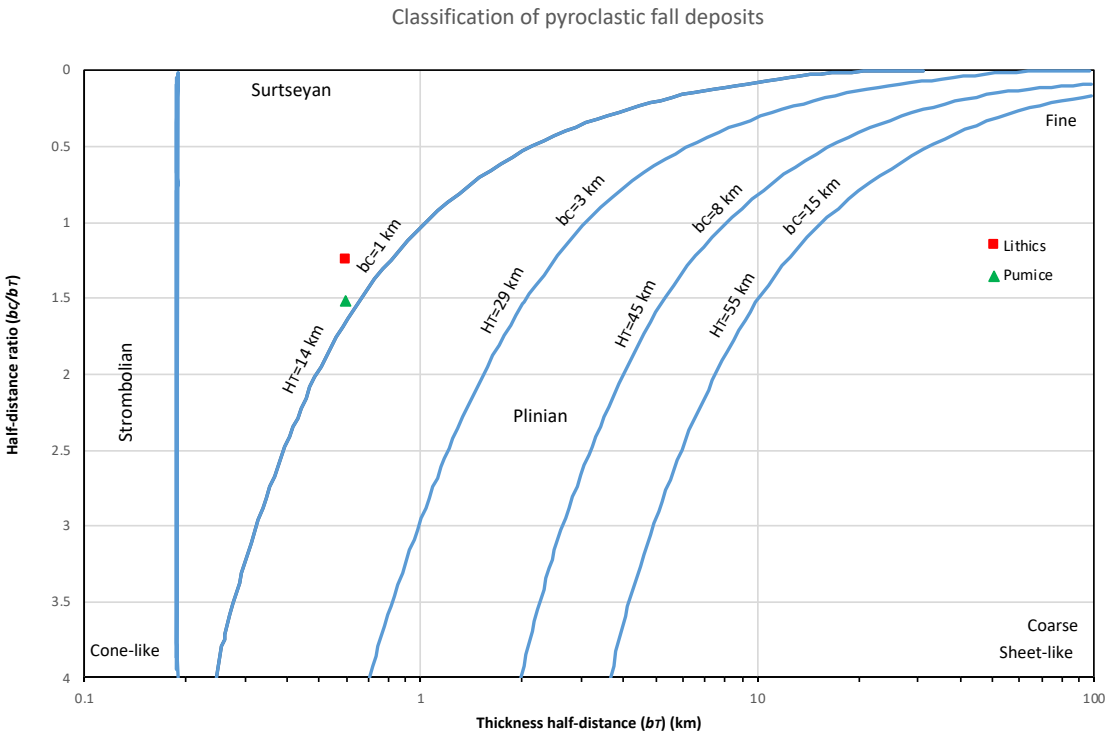

Figure 4.8 *Diagram classifying the pyroclastic fall deposits of Member C. Edited from Pyle (1989). Isopleth volumes were extracted for both lithic and pumice clasts. The differing clast size half distance (b_c) demonstrates the density contrast between the different types of tephra.*

4.4 Member D

The deposits of Member D, erupted from the northern crater, are the most widely dispersed of the Caldera del Rey formation. They are formed from multiple closely spaced, depletive pyroclastic density currents that range between fully dilute and granular fluid-based. The member is typically composed of mLT and sLT lapilli tuffs that show variable water contents. The matrix supported nature, variable thickness, poor sorting and infilling of topography confirms the deposits were dominantly produced from pyroclastic density currents.

The proximal deposits of both unit 1 and unit 2 comprise mLT and bLT that were produced by more granular fluid-based currents with fluid escape- to granular flow-dominated flow-boundary zones. Occasional diffuse-bedding is the result of current unsteadiness caused by high shear rates. Conversely, sLT were likely produced by close to fully dilute currents with traction-dominated flow-boundary zones. Lateral lithofacies changes are observed with distance from source (see section 4.9). mL are occasionally found and record fallout from short-lived umbrella clouds.

4.4.1 Barranco del Rey deposits

In this location Member D is predominantly composed of fine ash (mT) and mTpel. These beds record fallout from co-ignimbrite plumes that lofted to heights of at least 300 m above the vent. The occurrence of multiple thin beds suggests a significant number of co-ignimbrite plumes were generated that may individually correlate with underflow deposits.

Pumice fall deposits (mL) are interbedded and record the formation of short-lived umbrella clouds that were generated alongside pyroclastic density currents. The pumice fall deposits found in this location likely correlate with the pumice fall lithofacies found alongside the underflow deposits.

4.4.2 Eruption Characteristics

Different grainsizes observed within this member reflect different degrees of fragmentation that are primarily controlled by the phreatomagmatic influence and energy of the eruption. This could be a result of low groundwater recharge rates (Lorenz, 1986) or result from increased mass discharge rates (Brown et al., 2007).

Member D marks a transition from a buoyant plume and umbrella cloud (Member C) to a phase of generally pulsatory fountaining. It is likely the change in plume buoyancy resulted from the addition of water into the system and progressive vent widening. Multiple, short-lived eruption columns and umbrella clouds developed during the persistent phreatomagmatic explosivity, possibly marking relatively dry eruptions, similar to the 1965 eruption at Taal Volcano (Moore, 1967).

4.5 Member E

The deposits of Member E represent the final eruptive phase. They were erupted from the northern crater and formed from multiple short-lived, pulsatory fully-dilute pyroclastic density current. The member is typically composed of sT and xsT tuffs with

abundant coated ash pellets. This member records a very wet phase. The matrix supported nature, thickness variations, poor sorting and infilling of topography confirms the deposits were produced from PDCs. Fractures and jointing have formed in exteriors of some of the pumice clasts. These most likely represent thermal fractures that formed during cooling (Patel et al., 2013).

Unit 1 is primarily composed of thinly bedded, xsT. This unit was deposited from closely spaced, short-lived, successive fully dilute currents with traction-dominated flow-boundary zones. Cross-stratification is very common, suggesting there was regularly non-uniformity between the current and the substrate (Branney and Kokelaar, 2002).

Unit 2 is composed of thickly bedded sT and bLT that were produced from multiple closely spaced eruptions. The lithofacies were likely deposited from fully dilute currents with traction-dominated flow-boundary zones. The thickly bedded nature suggests the eruptions were more sustained than unit 1.

The fine grainsize, abundant coated ash pellets, impersistent bedding, soft-state deformation and slumping suggest that this member was produced by moist and cool currents. This member contained the greatest water component of the Caldera del Rey formation and was likely accompanied by a sustained and substantial influx of water into the system. This could be a result of progressive fracturing of the basaltic aquifer opening pathways for groundwater to enter the system. Alternatively, surface water may have accumulated in the crater and provided a source of additional external water. However, there was no evidence of crater lake deposits found in the field.

The transition from coarse-grained granular fluid-based PDCs of Member D to fine-grained fully dilute PDCs of Member E represents the waning phase of the northern crater eruptions. The PDCs of Member E likely originated from sustained low fountaining eruptions that lacked the kinetic energy normally transferred from a high fountain (Branney and Kokelaar, 2002).

4.6 Distal Outcrops

The most distal outcrop, exposed 3.9 km east of Caldera del Rey, is primarily composed of sT and mTpel. The deposits were produced by co-ignimbrite plumes and depletive pyroclastic density currents (Figure 4.9). The limited thickness of the deposits (90 cm) is a result of distance from the vent. The preserved deposits formed from the highest energy eruptions to overcome the large distance and potential barriers.

The stratified tuffs are inferred to have originated via ash fallout from either the distal portions of an umbrella cloud or co-ignimbrite plume. mT record the fine-grained deposits of depletive pyroclastic density currents. Coated ash pellets are the fall-out products of wet co-ignimbrite plumes. mTacc are found which pass upwards into framework-supported pellets and record the simultaneous deposition from a co-ignimbrite plume and dissipating pyroclastic density currents.

Individual members are not distinguishable in this outcrop. However, it is likely the deposits belong to Member D given the lithofacies present and the widespread dispersion of this member. Furthermore, the resemblance of these deposits to the deposits found in the hills northeast of Caldera del Rey provides more evidence to support this.

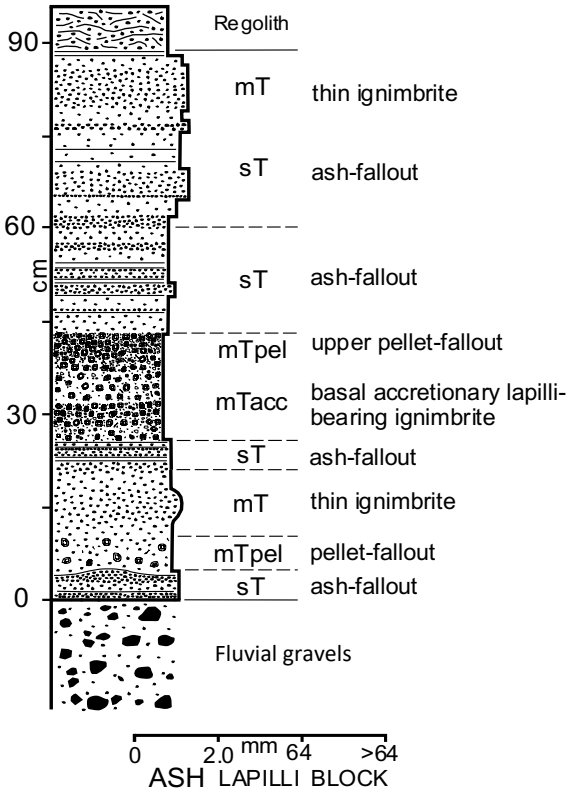

Figure 4.9 *Log and interpretation of the distal outcrop of the Caldera del Rey Formation north of Montaña Guaza (GR: 0334235 3104847).*

4.7 Ash Aggregation

Ash aggregates are commonly found within the phreatomagmatic deposits of Caldera del Rey (Members B, D and E) which likely contained the necessary water to promote hydrostatic adhesion of ash aggregates (Schumacher and Schmincke, 1991, 1995; James et al., 2002; Van Eaton et al., 2012, 2015).

Accretionary lapilli are commonly found matrix-supported and randomly distributed in the deposits of Members B and D. It is inferred that accretionary lapilli originate from ash pellets in the upper levels of co-ignimbrite plumes that lofted from the top of the dilute pyroclastic density currents. As the ash pellets pass through the lower parts of a hot, turbulent, density-stratified underflow they accrete a fining outwards ash rim and are transformed into accretionary lapilli (Brown et al., 2010).

Several layers, particularly found in Member D, that commonly overlie the accretionary lapilli bearing deposits, contain a layer of coated pellets that occasionally grade up into framework-supported ash pellets. This likely records the fallout of ash pellets from co-ignimbrite plumes during quiescent intervals. Coated pellets form as the ash pellets fall through dusty moist air left over from recently dissipated currents. Ash pellets fall through clean air (Brown et al., 2010) and, when present, reflect a substantial hiatus between currents. This sequence is observed in many of the large ignimbrites on Tenerife (Brown et al., 2010) and occurs in many other hydrovolcanoes (e.g. Walker, 1984; Sohn and Chough, 1989; Chough and Sohn, 1990; Mastrolorenzo, 1994). The deposits often show soft-state deformation and fluid-escape structures which suggest they were wet when deposited (Brooker et al., 1993).

Many of the deposits containing ash aggregates show an increase in abundance between proximal and medial locations. This suggests that the co-ignimbrite plumes mostly become buoyant and lofted on the slopes of the tuff ring. Coated ash pellets are abundant in the deposits of Member E. These likely formed as they passed through the fallout-dominated flow-boundary zone of weak, fully-dilute PDCs (Branney and Kokelaar, 2002). Where framework-supported quantities of aggregates are found it is assumed that this corresponds to the main period of fallout from the co-ignimbrite

plume. Matrix-supported quantities likely formed from a depleted co-ignimbrite plume. It is assumed that multiple co-ignimbrite plumes were created during the deposition of this member.

The generally random distribution of ash aggregates in the Caldera del Rey formation is a result of the pulsatory eruptions typical of phreatomagmatic eruptions (Colella and Hiscott, 1997). This leads to multiple flows occurring within quick succession of each other. Pauses long enough to allow fallout from co-ignimbrite plumes are rare and the process will often be disturbed by the next current. This is reflected by the abundance of accretionary lapilli and the rarity of ash pellets in this formation. This likely created a semi-constant ash plume around the tuff ring, in a similar way to an Oruanui-like scenario (Houghton et al., 2015, Fig.30.9B).

4.8 Lithic Fragments

A large majority of the lithic fragments are derived from the 'Old Basaltic Series' that forms the substrate and the northern rim of Caldera del Rey. Directly north of Caldera del Rey the 'Old Basaltic Series' is composed of horizontally orientated, very thickly bedded (2–5 m), lava flow deposits (Ancochea et al., 1990). These are typically basaltic and have multiple petrographic variations (Table 3.3). Additionally, fragments of pre-dating pyroclastic units are found. Fragments of the welded, distinctly orange coloured 1.559 ± 0.014 Ma Adeje formation (Dávila Harris, 2009) and a welded, poorly eutaxitic ignimbrite are found.

Aphanitic basalt is the most dominant lithology present (Figure 3.25) throughout the Caldera del Rey formation. This suggests that this is the dominant aquifer lithology in the diatreme, where the phreatomagmatic eruptions occur. Similarly, porphyritic basalt and ankaramite are also found in substantial abundances which suggests they are also dominant in the aquifer. A wide variety of lithologies reflects the sharp differences in lava flow deposits of the 'Old Basaltic Series' and suggest a diatreme vertical length of hundreds of metres (White and Ross, 2011).

The Adeje formation, approximately 0.6 Ma older than the Caldera del Rey formation, is likely the youngest lithic fragment found, and at the time of the eruption, would have been situated very close to the surface. This fragment type is dominantly found in Member A and decreases in abundance upwards through the Caldera del Rey formation. Additionally, fragments of welded ignimbrite show a marked increase in abundance in Member D. Therefore, it is inferred that these observed changes in lithic fragment lithology shows the downward migration of the diatreme with time during phreatomagmatic explosive activity (Lorenz and Kurszlaukis, 2007). Similar inferences have been made elsewhere for hydrovolcanoes (e.g. Saefell tuff-cone, Iceland, Mattsson et al., 2005; Kienle et al.,1980; White, 1991).

4.9 Pumice Densities

Pumice clasts show a general upwards trend to higher densities and lower vesicularities in the Caldera del Rey formation. The mean vesicularity of the pumice clasts is generally high (52–75%; Figure 3.26), which is common for silicic pyroclastic deposits (Houghton and Wilson, 1989; Cashman and Mangan, 1994; Gardner et al., 1996). Additionally, there is a marked difference in vesicularity values for different depositional processes. Pumice clasts from fall deposits (Members A and C) generally have high average vesicularities (72-75%) and a small range of values. Conversely, pumice clasts deposited by pyroclastic density currents (Members B, D and E) have lower average vesicularities (52-67%) and a greater range of values. This a common characteristic of hydrovolcanic juvenile clasts (e.g. Mt Rawdon, Australia, Brooker, 1991; Brooker and Jaireth, 1995; Tepexitl, Mexico, Austin-Erickson et al., 2008, 2011; Houghton and Wilson, 1989; Klug et al., 2002; Cashman and Rust, 2016).

The pumice clasts sampled from Member B were taken from pumice fall beds found in unit 4. The fine-grainsize of the finer-grained beds in Member B meant it was not possible to collect samples of an adequate size. Hence, the pumice clasts of Member B plot closer to Members A and C. The density of the pumice clasts present in the phreatomagmatic beds in Member C would be expected to give values similar to Members D and E.

The pumice clasts generated during the phases that produced pyroclastic density currents have significantly lower vesicularities than those produced by pumice clasts found in the pumice fall deposits. It is possible the additional water quenched the pumice clasts soon after fragmentation, and in doing so inhibited bubble growth and coalescence (Klug et al., 2002).

The upwards trend towards higher densities observed within Members A and B forming from the southern crater and Member C – E forming from the northern crater may also suggest a transition towards pumice clasts fragmenting from either crystalline or partially degassed magma. This transition would produce pumice clasts with highly variable densities that are typically close to 1 g/cm3 (Cashman, 2004; Cashman and Rust, 2016), as is observed in the pumice clasts of Members D and E (Figure 3.26).

4.10 Volcanic Ballistic Projectiles

Volcanic ballistic projectiles are centimetre- to metre-sized pyroclasts of solid to molten fragments ejected during explosive volcanic eruptions (Taddeucci et al., 2017). They move through the atmosphere along ballistic trajectories that are dependent on the highly variable nature of explosive volcanic eruptions (Self et al., 1980). The ballistic projectiles in the Caldera del Rey formation are predominantly composed of blocks of mafic lavas that were fragmented from the basaltic aquifer below Caldera del Rey. The impact of the ballistic projectiles often results in well-defined sags that reflect the wet nature of the deposits.

The spatial density of the clasts decreases with distance from the vent (Figure 3.28). This is a common occurrence for ballistic projectiles irrespective of the eruption style (Kilgour et al., 2010). A circular distribution is observed for the ballistic projectiles that originated from the northern crater (Figure 4.10). This suggests the eruptions were predominantly vertical and the axis symmetrical (e.g. de'Michieli Vitturi et al., 2010).

The size of the ballistic projectiles generally decreases away from the vent (Figure 4.10). This is a common characteristic of phreatomagmatic eruptions (Lorenz, 1970; Self et al., 1980; Waitt et al., 1995; Sottili et al., 2012). Furthermore, the same trend is observed in

the ballistic projectiles produced by a Plinian phase from the 79 A.D. Vesuvius eruption (De Novellis and Luongo, 2006). This distribution results from the pyroclasts being ejected and supported in a gas stream (Lorenz, 1970), and the time at which they decouple is a function of their angle of ejection and terminal velocity. Smaller projectiles are influenced more by the turbulent plume motion than larger ones, and as a result are carried to greater heights in the atmosphere before leaving the eruption column (Self et al., 1980). Hence, larger blocks tend to fallout first and closer to the vent.

Evidence for blocks being entrained and carried to substantial heights before decoupling was observed in the deposits of Member D situated in Barranco del Rey, east of Caldera del Rey. The deposits record ballistic projectiles, up to 50 cm in diameter, which are situated 300 m above the base of the current caldera floor.

Given the almost continuous explosions at the crater during phreatomagmatic phases, a fairly maintained gas stream column is likely, similar to that recorded during the 1957 Capelinhos eruption (Waters and Fisher, 1971).

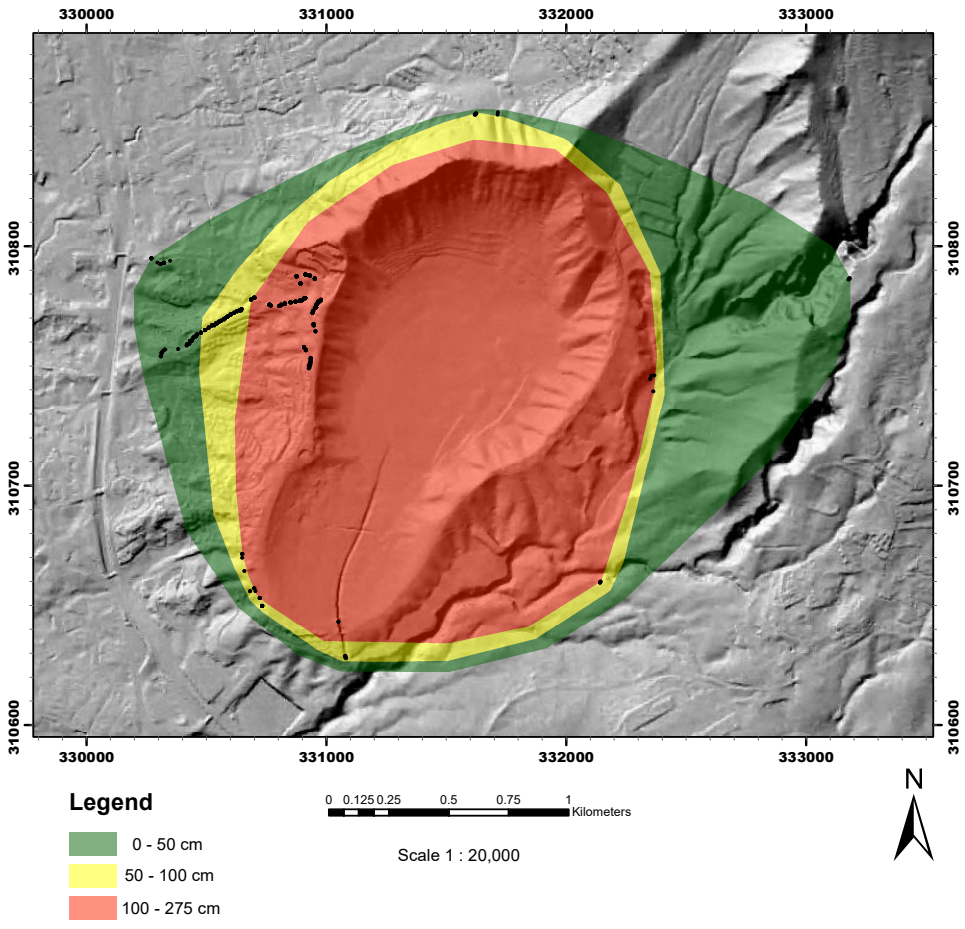

Figure 4.10 *Map showing the size distribution of ballistic projectiles originating from the northern crater.*

4.10.1 Ballistic Eruption History

Member A contains a moderate abundance of ballistic projectiles that dramatically increase in abundance at the top of the member. The typically coarse lapilli and block sizes reflect the high energy and the eruptions and poor fragmentation rates. The eruption column that produced the deposits of Member A likely facilitated the ejection of the ballistic projectiles to significant heights before decoupling. The sudden increase towards the top of the member crated a belt of impact craters and likely represents a phase of vent widening and crater forming explosions (Self et al., 1980).

Ballistic projectiles are limited in abundance and size in Member B. This is attributed to more efficient fragmentation (Carrasco-Núñez et al., 2007) and reduced energy being available for ejecting blocks in phreatomagmatic explosions (López-Rojas and Carrasco-Núñez, 2015). Where impact sags are present, they tend to show the greatest plastic deformation of the Caldera del Rey formation, reflecting the high-water content. In some cases, the deformation is larger than the diameter of the ballistic block. The maximum velocities of the ballistic blocks are expected to be lower in this member given the high-water content (Self et al., 1980).

Ballistic projectiles are rarely observed in Member C. The member represents a fairly dry phase of the Caldera del Rey formation in which the fragmentation of the substrate was somewhat limited. When sags are preserved, they tend to show considerable deformation with the sag size often greater than the size of the block.

There is a sharp increase in the abundance of ballistic projectiles in Member D. This marks the onset of phreatomagmatic explosions and the growth of the diatreme. Persistent vent widening, diatreme growth and recycling of material provided a continuous supply of blocks. The ballistic projectiles were mainly supported in a gas stream that is typical of phreatomagmatic eruptions (Lorenz, 1970). Intermittent subplinian columns may have lofted some blocks to greater heights before decoupling. Larger ballistic projectile sizes and smaller sag sizes are observed in Member D compared to Member B, suggesting the eruptions were not suppressed due to extremely high-water contents, as they were in Member B.

Member E contains a low abundance of ballistic projectiles that are rarely greater than lapilli sized. However, they create significant sags when present. This reflects the high water content of the deposits which most likely led to high fragmentation rates and subdued eruptions. The ballistic projectiles were likely erupted at lower maximum velocities than the other members. A 10 wt.% increase in water content has been proven to lower velocities by up to 20% (Self et al., 1980).

4.10.2 Initial Velocities

Various ballistic projectile eruption characteristics were observed and calculated for the deposits of Member D and are presented in Table 4.3. The ballistic projectiles of Member D were used due to the large sample size (683 samples). Member D represents the climactic phase of the Caldera del Rey formation. Therefore, it is likely that some of the largest initial velocities were produced by this member. The ballistic projectiles of Member A were likely influenced by the eruption plume and had initial velocities greater than those calculated for Member D.

The largest and smallest ballistic projectiles observed have calculated initial velocities of 92 and 152 m s^{-1} respectively. The range in diameter and initial velocities for the ballistic projectiles of Member D is concordant with other phreatomagmatic eruptions (Table 4.3). Similarly, the maximum distance at which ballistic projectiles were recorded is consistent with other similar eruptions (Table 4.3).

The average block size (22 cm) for the Member D ballistic projectiles is calculated at 102 m s^{-1}. This is similar to the values predicted by Self et al. (1980), who calculated initial velocities of 100 ± 20 m s^{-1} for clasts 20–40 cm in diameter for the 1977 Ukinrek maars eruption. As with the Caldera del Rey formation, Self et al. (1980) calculated lower initial velocities for the larger ballistic blocks. Ballistic projectiles >40 cm in diameter were predicted to have initial velocities of 86–98 m s^{-1}. This was also noted by Rohlof (1969), who calculated initial velocities around 100 m s^{-1} for blocks >2 m.

Eruption	Style	Max distance (km)	Diameter range (m)	Initial velocity (m s^{-1})	Reference
Caldera del Rey	Phreatomagmatic /subplinian	1.6	0.05 – 2.5	92 - 152	
Atexac maar (Mexico)	Phreatomagmatic		0.1 – 2	100 – 120	López-Rojas and Carrasco-Núñez (2015)
1977 Ukinrek maars (Alaska)	Phreatomagmatic	0.7	2 – 25	100 – 150	Self et al. (1980)
Sabatini Volcanic District (Italy)	Phreatomagmatic	0.9	0.1 – 2	50 – 110	Sottili et al. (2012)
Big Hole maar (USA)	Phreatomagmatic	3	0.1 – 2.3	90 – 120	Lorenz (1970)
1996 Soufriere Hills (Montserrat)	Subplinian	2.1	0.1 – 2	155 - 840	Waitt et al. (1995)

Table 4.3 *Table comparing Caldera del Rey ballistic projectile eruption characteristics with other examples from the literature.*

4.11 Eruption History

Caldera del Rey was constructed by two overlapping craters that show similar progressions regarding their eruptive history. The eruptions started with the generation of a buoyant plume that collapsed to form multiple, closely spaced pyroclastic density currents that originated from phreatomagmatic eruptions. The formation commenced with eruptions that led to the creation of the southern crater. The eruptions then shifted northwards, where a second larger crater was created. The shift in vent location is attributed to a change in the direction of supply or the generation of a second feeder dyke (Ross et al., 2017).

Eruptions occurred between magma and groundwater within an aquifer composed of 'Old Basaltic Series' lava flow deposits (Fuster et al., 1968). Intermittent supply of groundwater led to wet and dry eruption phases as well as variations in the degree of phreatomagmatic fragmentation.

The first phase of the Caldera del formation was the generation of a sustained, initially steady, bent-over eruption plume and umbrella cloud that produced the massive pumice fall deposits of Member A (Figure 4.11A). This initial phase to the eruption

mirrors that of the 1977 Ukinrek maars eruption, Alaska (Self et al., 1980). The plume was directed westward. Over time the plume began to fluctuate in height and a sudden increase in ballistic projectiles towards the top of the member suggests a period of vent widening and the formation of a protodiatreme (Valentine and White, 2012). This was likely the result of an increased supply of groundwater into the system from a progressively fracturing aquifer.

Once the vent widening and diatreme downward migration reached a critical point, the plume collapsed, and a period of low fountaining developed and deposited Member B (Figure 4.11B). This produced mainly fully-dilute pyroclastic density currents that originated from the interaction of a large supply of groundwater and magma within a growing diatreme. The supply of water became intermittent towards the top of the member. The typically fine-ash grainsize of the deposits suggests very effective phreatomagmatic fragmentation occurred. It is also likely that Member B formed from partially degassed magma.

The eruptions then shifted to the northern crater where a highly fluctuating, moderately sustained bent-over eruption plume and umbrella cloud generated pumice fall deposits of Member C (Figure 4.11C). The plume was initially directed southwards before shifting westwards towards the end of the eruption. Member C possibly marks a return to drier conditions. However, the eruptions contained a higher wt.% water than those that produced Member A. This was likely a period in which the groundwater level was returning to pre-Member B levels.

The eruption style then transitioned into closely spaced, pulsatory pyroclastic density currents that developed from semi-constant fountaining and deposited Member D (Figure 4.11D; Figure 4.11E). The currents were widely and radially dispersed and represent the climactic phase of the Caldera del Rey eruptions. Co-ignimbrite plumes commonly lofted from the top of these currents. This phase of the Caldera del Rey formation likely records 10s to 100s of phreatomagmatic explosions. The beds show rapid changes in the degree of fragmentation which shows changes in the amount of water interacting with the magma. Additionally, short-lived umbrella clouds deposit thin pumice fall beds and represent periods of plume buoyancy. An increase in the

abundance of ballistic projectiles at the base of this member suggests a period of vent widening and the formation of a new diatreme.

The final phase of the Caldera del Rey formation generated sustained low fountaining that produced slow moving depletive pyroclastic density currents that deposited Member E in the intracaldera regions (Figure 4.11F). This member marks the waning period following the deposits of Member D. The phreatomagmatic deposits resulted from a high wt.% water content that suggests a substantial ingress of water into the system. It is also likely that the deposits formed from partially degassed magma. Post-eruptive fluvial sediments have since partially filled the craters.

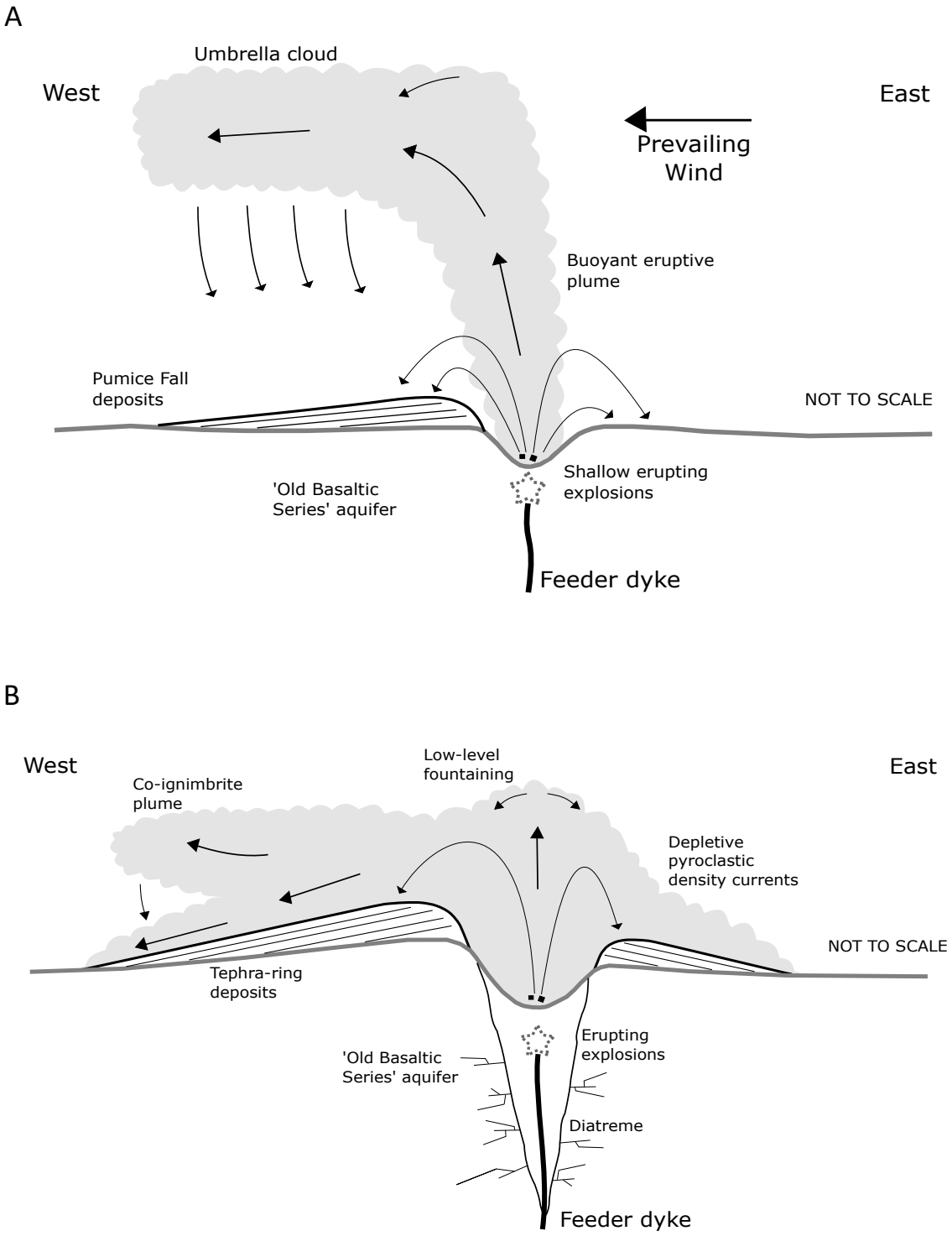

Figure 4.11 *Schematic diagrams depicting the eruptive processes for various phases of the Caldera del Rey formation –* ***(A)*** *Generation of Member A pumice fall deposits from a bent over plume and umbrella cloud. Shallow eruptions occur during the protodiatreme stage.* ***(B)*** *Generation of Member B phreatomagmatic deposits which resulted from low-level fountaining following plume collapse. Multiple eruptions have resulted in progression to a mature diatreme stage.*

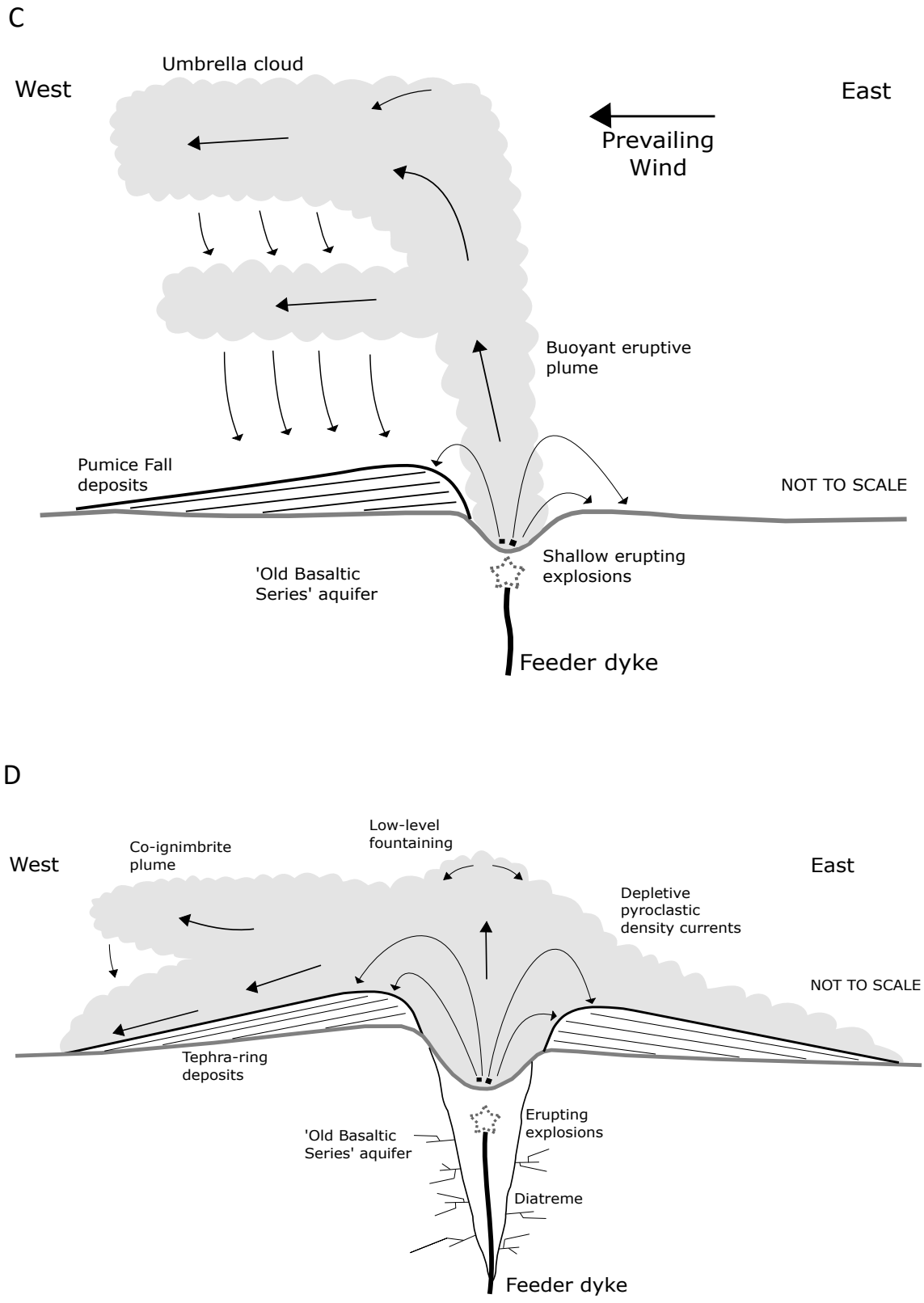

Figure 4.11 *(continued) –* ***(C)*** *Generation of Member C pumice fall deposits from a bent over plume and umbrella cloud that fluctuates in height.* ***(D)*** *Generation of Member D phreatomagmatic deposits which resulted from low-level fountaining that radially dispersed multiple pyroclastic density currents. Multiple eruptions have resulted in progression to a mature diatreme stage.*

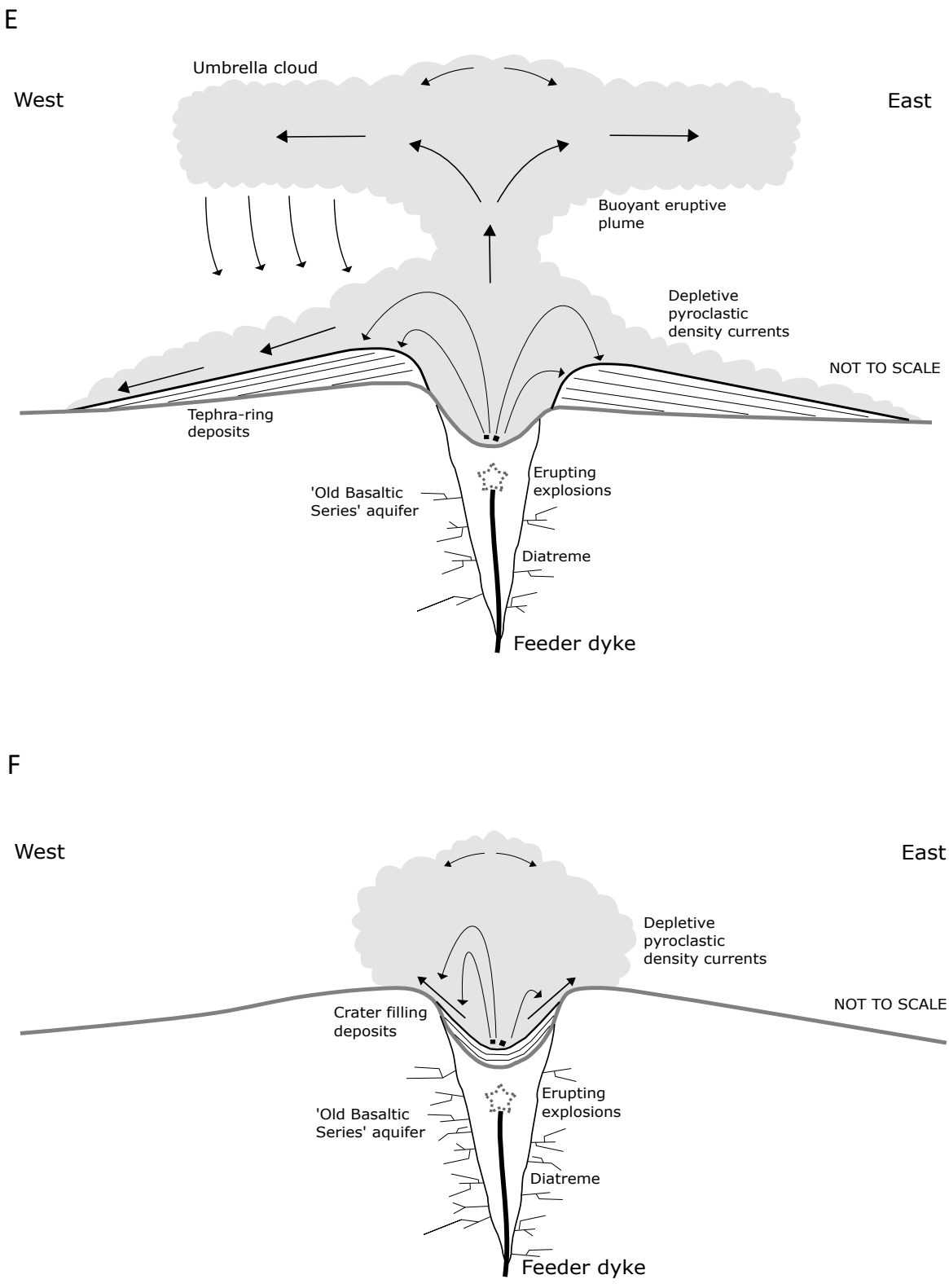

Figure 4.11 *(continued) –* ***(E)*** *Generation of a buoyant plume co-erupting with pyroclastic density currents during the deposition of Member D.* ***(F)*** *Generation of Member E phreatomagmatic deposits that infilled the craters.*

Chapter 5: Lithofacies Transitions

5.1 Lateral Lithofacies Transitions

Lateral lithofacies transitions are observed in the deposits of the pyroclastic density currents that deposited Members B and D. The great exposure in proximal and medial locations allows the transitions to be studied in detail. Lateral lithofacies Transition 1 (LFT 1) is observed in Member B, whereas LFT 2-5 are observed in Member D. This is due to a wider variety of lithofacies observed at proximal locations within Member D.

The downcurrent lithofacies transitions are all accompanied by radial thinning and fining trends from proximal to distal locations. The thickest and coarsest deposits are found at the crater rim and are the most proximal. There are presently no outcrops that show either diatreme or extreme distal deposits.

LFT 1 (xsLT, dsLT – mTacc, sT)

This sequence is observed within units 1 and 3 of Member B. The sequence begins with xsLT and dsLT in proximal locations (Figure 3.9A; Figure 3.9B). The deposits are generally thickly bedded between 60–80 cm. Cross-stratification is typically low angle (3–10°) and laterally persistent over 10s metres. Diffuse-bedding is discontinuous, sub-parallel, undulatory and usually defined by cm-thick lithic horizons and occasionally accretionary lapilli. This transforms downcurrent into mTacc, mTpel and sT (
Figure ***5.1***A).

LFT 2 (mLT – xsLT - sLT)

This sequence begins with mLT and dbLT lapilli-tuffs in proximal locations (Figure 3.18). The beds are typically thickly to very thickly bedded and poorly sorted. Diffuse-bedding is generally defined by lithic-rich horizons. In medial locations the lithofacies transition into xsLT. These beds are typically poorly sorted and medium to thickly bedded. Cross-bedding is generally low angle and cross cutting. Cross stratifications become more

common and well-developed with distance from the vent. This transforms further downcurrent into sLT (
Figure ***5.1***B).

LFT 3 (mLT, bLT – mTacc, mT)

This sequence begins with mLT and bLT lapilli-tuffs in proximal locations (Figure 3.18). The beds are typically thickly to very thickly bedded and poorly sorted. This transforms downcurrent into mTacc and mT. These beds are thin to medium bedded and contain matrix- to framework-supported quantities of accretionary lapilli (
Figure ***5.1***C).

LFT 4 (dblLT, lmLT – lbLT – bLT)

This sequence begins with lithic-rich dblLT and lmLT in proximal locations (Figure 3.18). The beds are typically thickly to very thickly bedded, poorly sorted and contain high clast concentrations. In medial locations the lithofacies transition into lbLT. These beds are also poorly sorted and medium to thickly bedded. This transforms further downcurrent into bLT (
Figure ***5.1***D).

LFT 5 (mT, dsLT, mTacc – mTacc, sT)

This sequence begins with dominantly massive mT in proximal locations (Figure 3.18). The beds are occasionally dsLT and can contain mTacc. The beds are typically thickly to thinly bedded. Soft-state deformation and prominent bedding sags formed beneath emplaced ballistic clasts is common. This transforms downcurrent into mTacc and sT. These beds are thinly bedded and contain mainly framework-supported quantities of accretionary lapilli (
Figure ***5.1***E).

A **LFT 1 (xsLT, dsLT – mTacc, sT)**

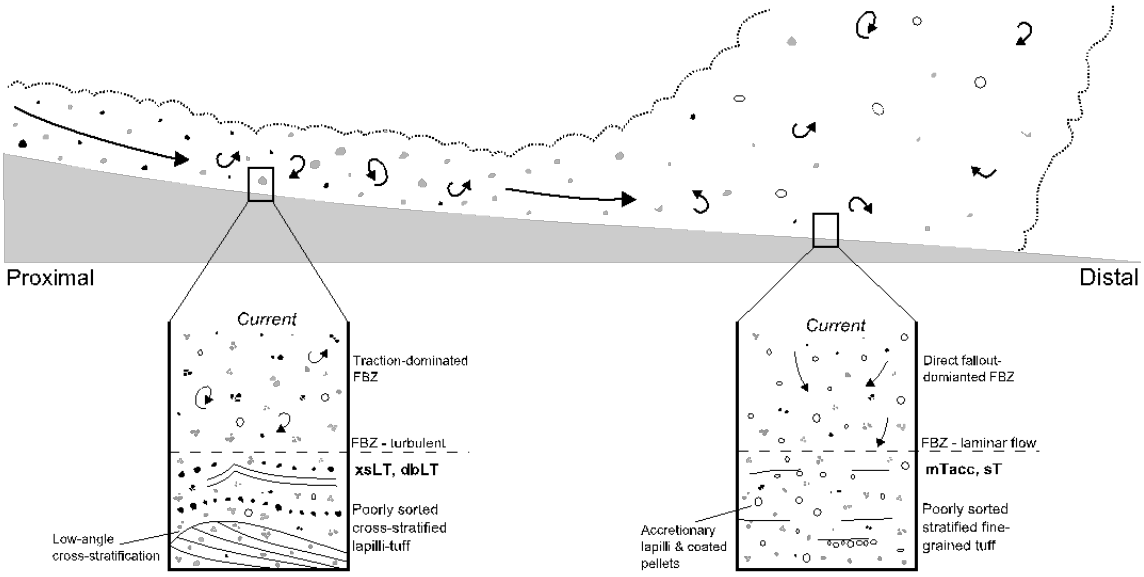

B **LFT 2 (mLT – xsLT - sLT)**

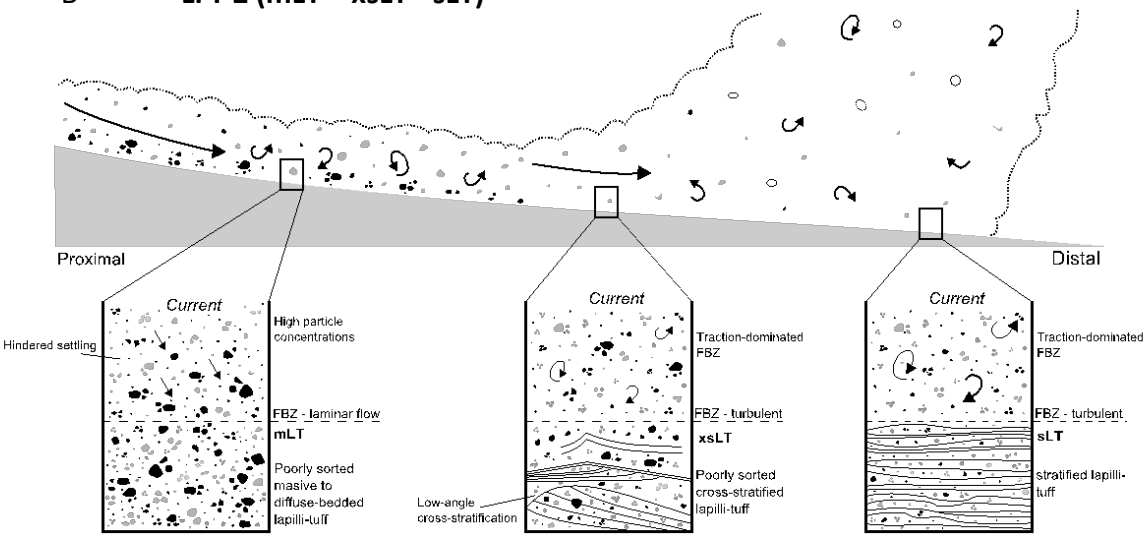

C **LFT 3 (mLT, bLT – mTacc, mT)**

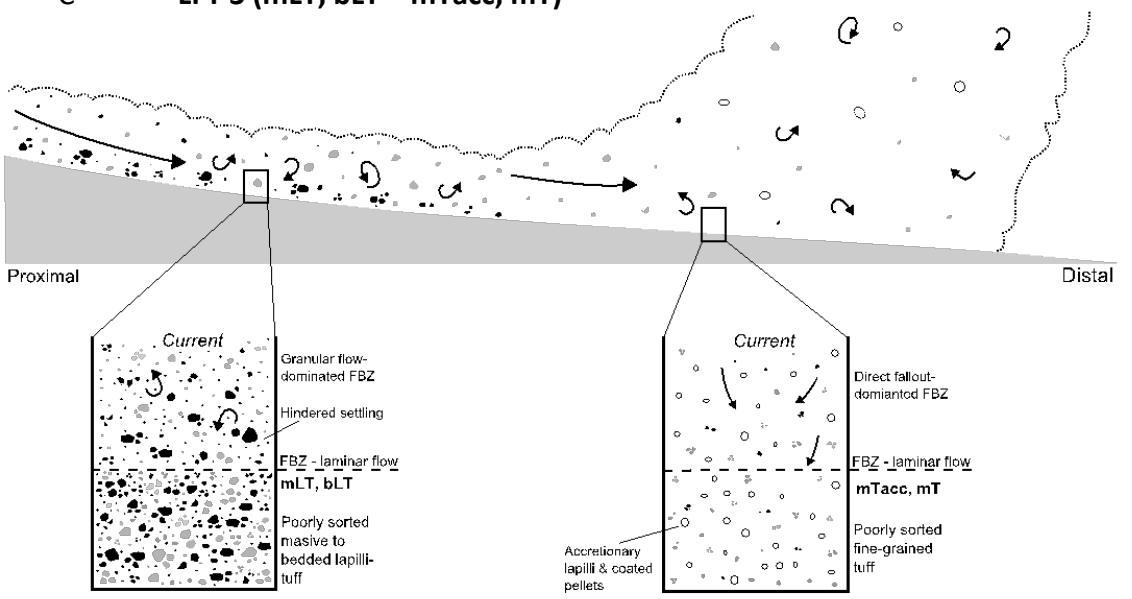

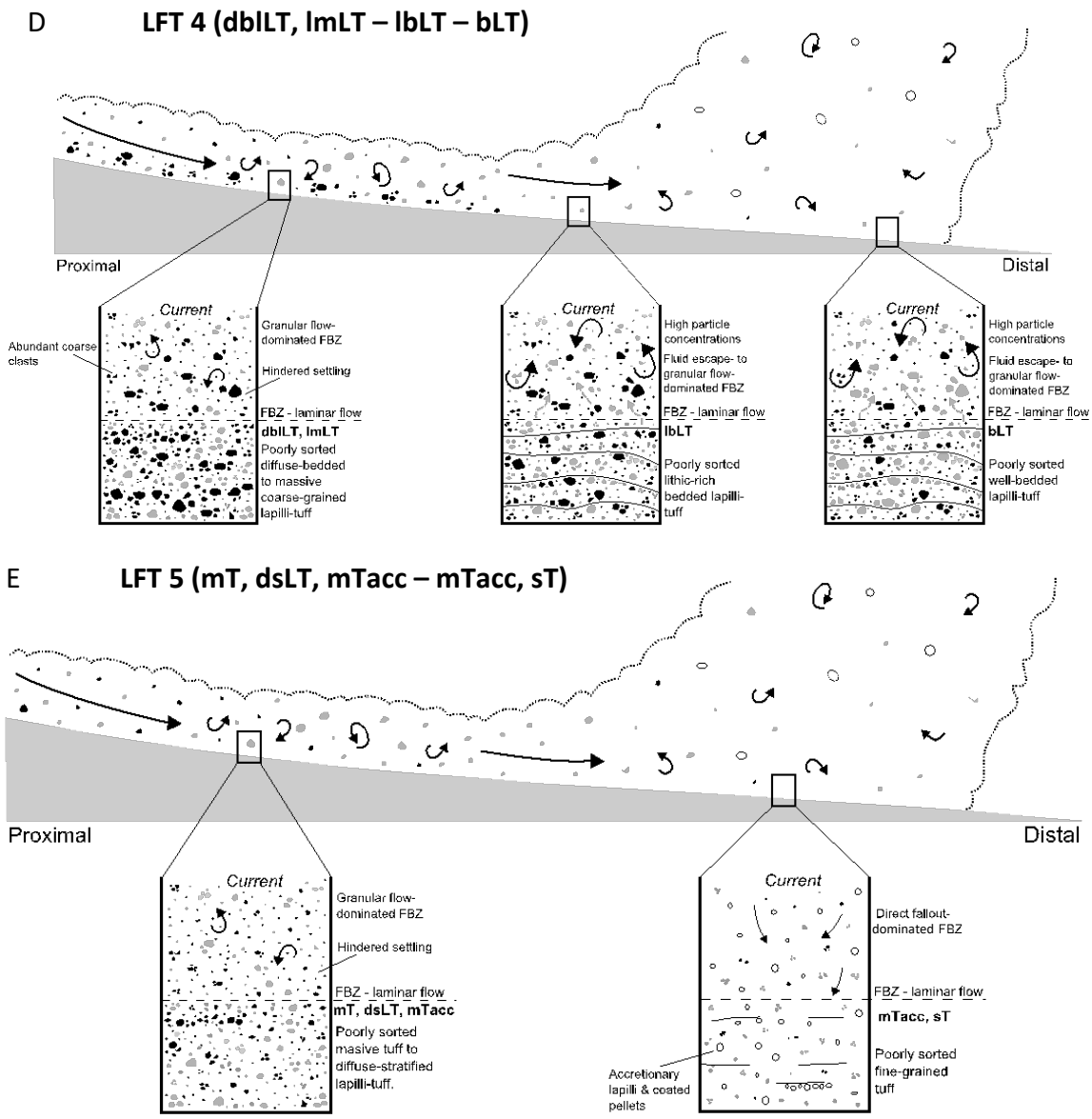

Figure 5.1 *Lateral facies transitions observed in the Caldera del Rey formation.* ***(A)*** *Transition from xsLT and dsLT in proximal locations to mTacc, mTpel and sT downcurrent, observed in Member B.* ***(B)*** *mLT and dbLT transition to xsLT in medial locations and sLT further downcurrent in distal locations.* ***(C)*** *mLT and bLT in proximal locations shift towards mTacc and mT downcurrent.* ***(D)*** *A sequence of dbLT and lmLT in proximal locations which in medial locations transition to lbLT and further downcurrent into bLT.* ***(E)*** *Proximal deposits of dominantly mT and occasional beds of dsLT and mTacc transition downcurrent into mTacc and sT.*

5.2 Interpretation of Transitions

The lateral lithofacies transitions observed in Members B and D of the Caldera del Rey formation are interpreted as downcurrent changes from proximal to distal locations. Repetitive phreatomagmatic blasts generated closely successive density currents that decelerated and lost capacity and competence with distance from the source (Chough and Sohn, 1990). The lithofacies record deposition from single-surge, depletive currents

that travelled downslope away from the vent. Where the deposits are channelised, they maintain competence and are not as depletive.

The inferences here are derived from the literature where there are similar examples of lithofacies transitions within small pyroclastic density currents that originated from tuff rings (Sohn and Chough, 1989; Chough and Sohn 1990; Colella and Hiscott, 1997; Vasquez and Ort, 2006; Brown et al., 2007).

The occurrence of cross-stratification and diffuse-stratification in the proximal deposits of units 1 and 3 of Member B indicates that the PDCs were likely fully dilute with traction-dominated flow-boundary zones (Brown et al., 2007). However, numerous thickly-bedded massive and diffuse-bedded lapilli tuffs occur in proximal locations in Member D. This suggests that these lithofacies were rapidly deposited from granular fluid-based density currents with granular flow-dominated and fluid escape-dominated flow boundary zones. These types of currents are more often associated with the deposition of ignimbrites, rather than the phreatomagmatic pulses that typically originate from tuff rings (Brown et al., 2007).

The coarsest material was generally deposited within 1 km of the vent, with the coarsest lithic blocks depositing rapidly and transported as bedload with only partial support from the turbulent particulate fluid (Branney and Kokelaar, 2002). Coarse lithic blocks that travelled to greater distances (>2 km) were feasibly entrained within the granular fluid at the low levels of the current (Choux and Druitt, 2002). Conversely, pumice clasts of a given size are found at a greater distance from the vent than lithic fragments of the same size. This is likely the result of overpassing of pumice and early deposition of dense lithic fragments (Branney and Kokelaar, 2002).

Various flow-boundary zone transitions are observed in the Caldera del Rey formation. The differences are the result of dissimilarities in the initial physical constitution of the erupted tephra that forms the currents. During phreatomagmatic explosivity there can be substantial variability in the amount of potential energy, thermal energy and clast concentrations (Kokelaar, 1986).

FLT 1 (xsLT, dsLT – mTacc, sT)

Facies transition laterally from cross-stratified and diffuse-bedded lithofacies into accretionary lapilli bearing and stratified lithofacies (LFT 1; Figure 5.2). The proximal lithofacies were deposited from close to fully dilute currents with traction-dominated flow-boundaries. Diffuse-bedding and the poor sorting suggests temporary shifts to granular flow-dominated processes (Brown et al., 2007). The high particles concentrations within the diffuse-bedded deposits limited the efficiency of particle segregation (e.g. by winnowing) in the flow-boundary zone (Branney and Kokelaar, 2002).

The lithofacies show a quick downcurrent transition to fully dilute currents with mainly direct fallout-dominated and occasional traction-dominated flow boundary zones (Branney and Kokelaar, 2002). This indicates tractional processes occurred over long distances as the currents decelerated and subsequently lost capacity with distance from the vent.

LFT 2 (mLT – xsLT - sLT)

The lateral transition from massive lithofacies into cross-stratified and stratified lithofacies (LFT 2; Figure 5.3) records the downcurrent evolution from granular fluid-based currents to fully dilute currents. The proximal massive lapilli-tuffs were deposited from fluid escape- to granular flow-dominated flow boundary zones within granular fluid-based currents. Traction-dominated flow-boundary zones dominate in medial and distal regions. This transition is due to the dilution and expansion of the current and the progressive deposition of the bedload (Vasquez and Ort, 2006). This results in low particle concentrations in the flow-boundary zone which creates a sharp interface between the current and the deposit where tractional processes can dominate. Cross-stratifications record localised current non-uniformity (Brown et al., 2007). Finer-grained material is transported to distal regions because of the depletive competence of the current, coupled with the proximal deposition of the coarse bedload.

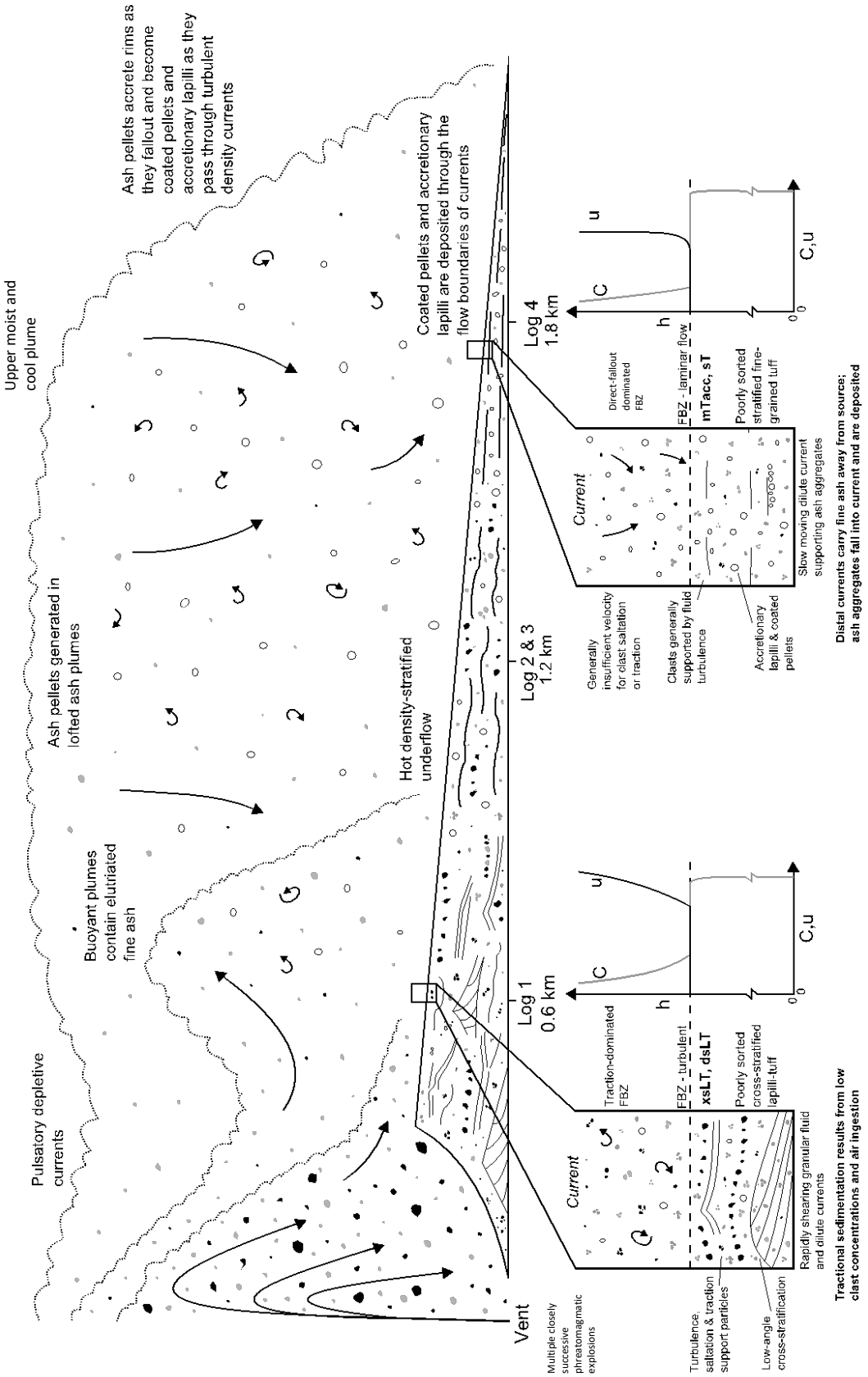

Figure 5.2 *Illustration showing the lateral downcurrent lithofacies changes inferred to have occurred in the single-surge, depletive pyroclastic density currents that deposited LFT 1. Progressive air ingestion and the proximal deposition of coarse bedload resulted in the lateral transition from traction- and granular flow-dominated flow-boundary zones near source to direct fallout- and traction-dominated flow boundary zones in distal regions. Ash aggregates formed in the lofted ash plumes and accreted rims as they passed through the successive density currents. Flow boundary illustrations modified from Branney and Kokelaar (2002).*

The transition from granular-fluid based currents to fully dilute currents has been observed at other tuff rings (e.g. Sohn and Chough, 1989; Chough and Sohn 1990; Colella and Hiscott, 1997; Brown et al., 2007). Single-surge depletive currents have a finite amount of tephra with which they are initiated with. This progressively diminishes with deposition and elutriation of fine-ash into a buoyant cloud during transport. Thus, some granular fluid-based currents can transition into fully dilute currents with a corresponding traction-dominated flow-boundary zone (Brown et al., 2007).

LFT 3 (mLT, bLT – mTacc, mT)

Downcurrent transitions from massive and bedded lapilli-tuffs to accretionary lapilli bearing massive tuffs records the evolution from granular flow-dominated flow-boundaries to fluid escape- to fall-out-dominated flow boundaries (LFT 3; Figure 5.4). Particle concentrations in the flow-boundary zone must have remained high enough to inhibit the penetration of turbulent eddies onto the substrate, even in distal regions (Brown et al., 2007).

LFT 4 (dblLT, lmLT – lbLT – bLT)

The lithofacies transition from diffuse-bedded and massive to bedded lapilli-tuffs records the deposition from granular fluid-based currents (LFT 4; Figure 5.5). Lithic-rich diffuse-bedded and massive lithofacies in proximal regions record fairly rapid aggradation from granular flow- to fluid escape-dominated flow boundaries. Diffuse-bedding is the result of current unsteadiness caused by high shear rates (Brown et al., 2007). Massive lithofacies are caused by lower shear rates and/or higher aggradation rates and represent a transition towards fluid escape- to granular flow-dominated flow boundaries (Branney and Kokelaar, 2002). The depletive flow results in the proximal deposition of the coarsest bedload. However, the depositional flow-boundary zone retained high clast concentrations, which inhibited winnowing in the lowermost zones. This suggests the flux of clasts to the flow-boundary zone was equal, or greater than, the flux of clasts lost by deposition (Brown et al., 2007). Thus, a large proportion of the load was likely carried as granular fluid (Branney and Kokelaar, 2002).

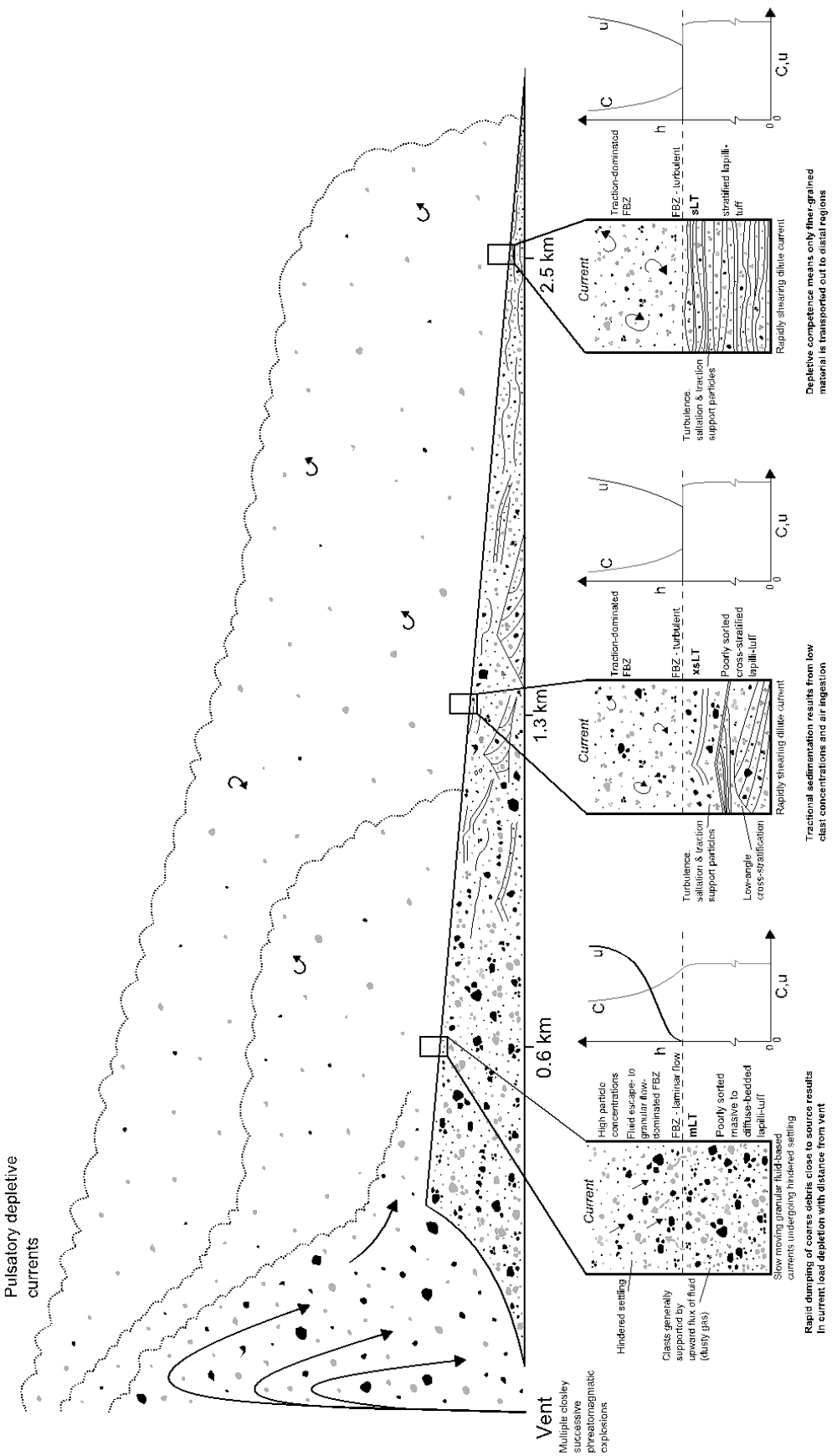

Figure 5.3 *Illustration showing the lateral downcurrent lithofacies changes inferred to have occurred in the single-surge, depletive pyroclastic density currents that deposited LFT 2. Progressive air ingestion and the proximal deposition of coarse bedload resulted in the lateral transition from fluid escape- to granular flow-dominated flow boundary zones to traction-dominated flow-boundary zones in medial and distal regions. The lithofacies record the downcurrent evolution from granular fluid-based currents to fully dilute currents. Flow boundary illustrations modified from Branney and Kokelaar (2002).*

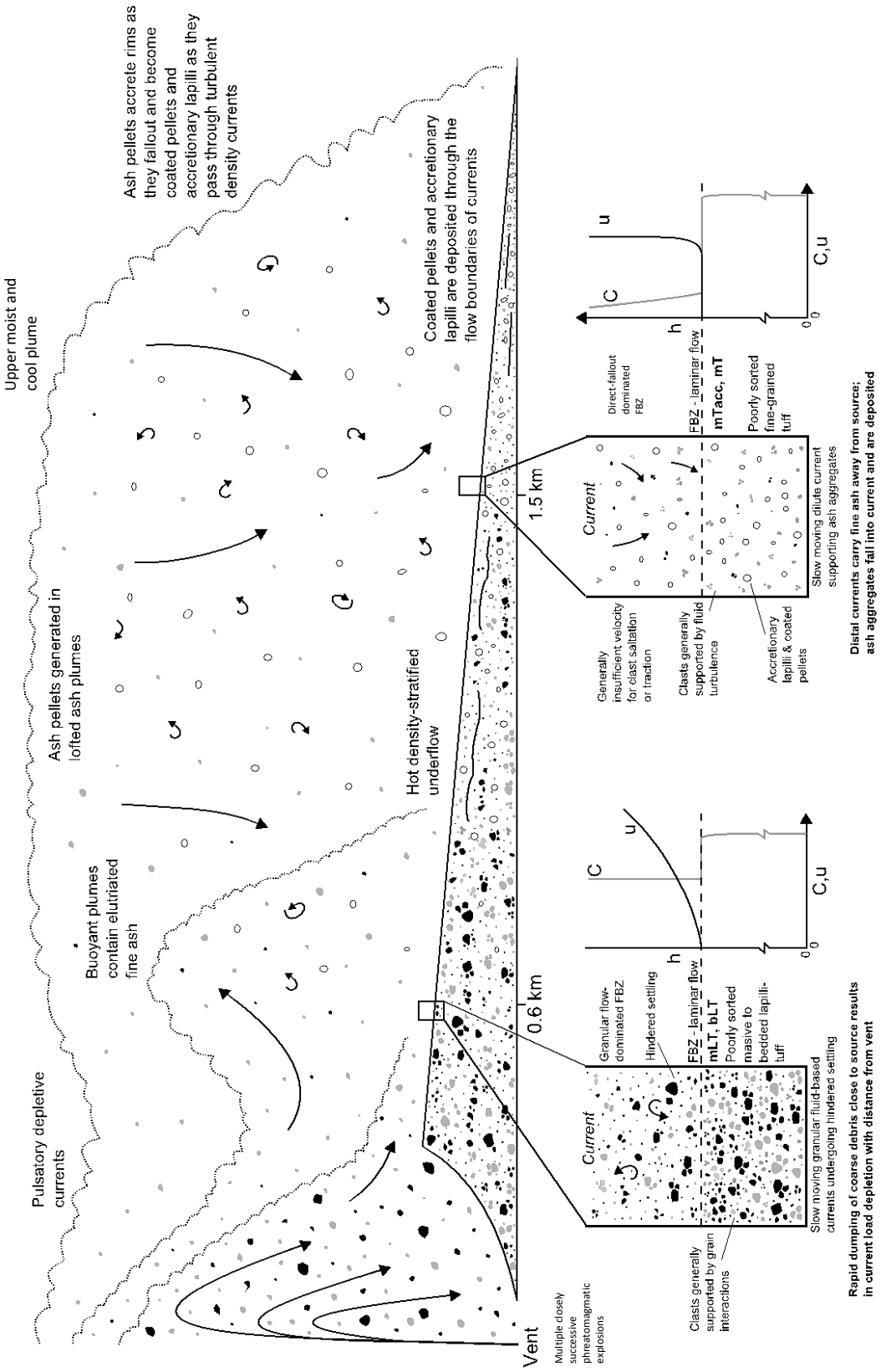

Figure 5.4 *Illustration showing the lateral downcurrent lithofacies changes inferred to have occurred in the single-surge, depletive pyroclastic density currents that deposited LFT 3. Transitioning from granular flow-dominated flow boundaries to fluid escape- to fall-out-dominated flow boundaries occurred as a result of depletive flow. Particle concentrations in the flow-boundary zone remained high. Ash aggregates formed in the lofted ash plumes and accreted rims as they passed through the successive density currents. Flow boundary illustrations modified from Branney and Kokelaar (2002).*

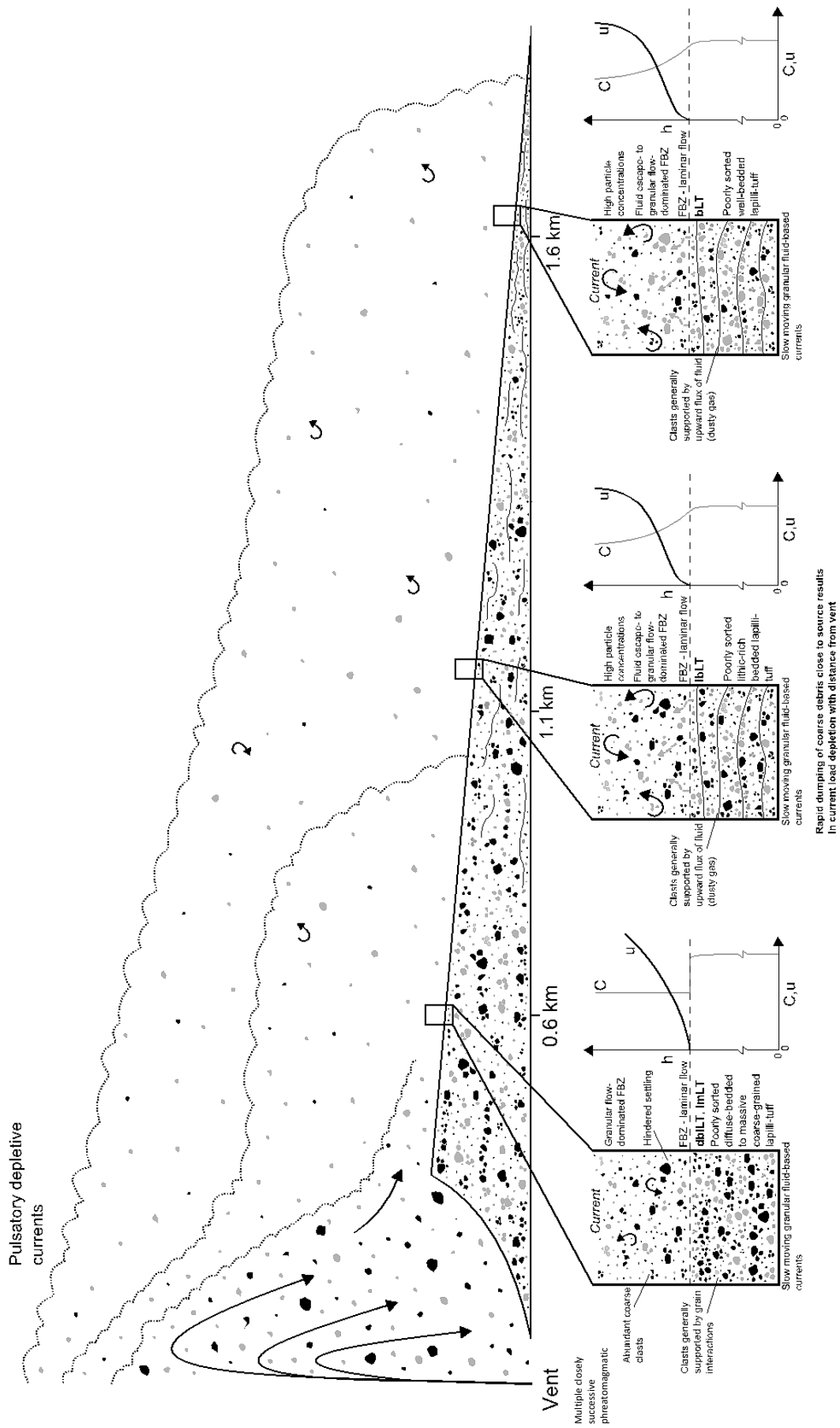

Figure 5.5 *Illustration showing the lateral downcurrent lithofacies cnanges inferred to have occurred in the single-surge, depletive pyroclastic density currents that deposited LFT 3. The lithofacies record the deposition from granular fluid-based currents with granular flow- to fluid escape-dominated flow boundaries. Flow boundary illustrations modified from Branney and Kokelaar (2002).*

LFT 5 (mT, dsLT, mTacc – mTacc, sT)

The lateral transition from massive, diffuse-stratified and ash aggregate bearing lithofacies into ash aggregate bearing and stratified lithofacies (LFT 5; Figure 5.6) records the downstream evolution from fully dilute currents. The proximal facies were deposited from mainly granular flow-dominated flow boundaries, whereas the medial and distal lithofacies were deposited from currents with fall-out- to traction-dominated flow boundaries.

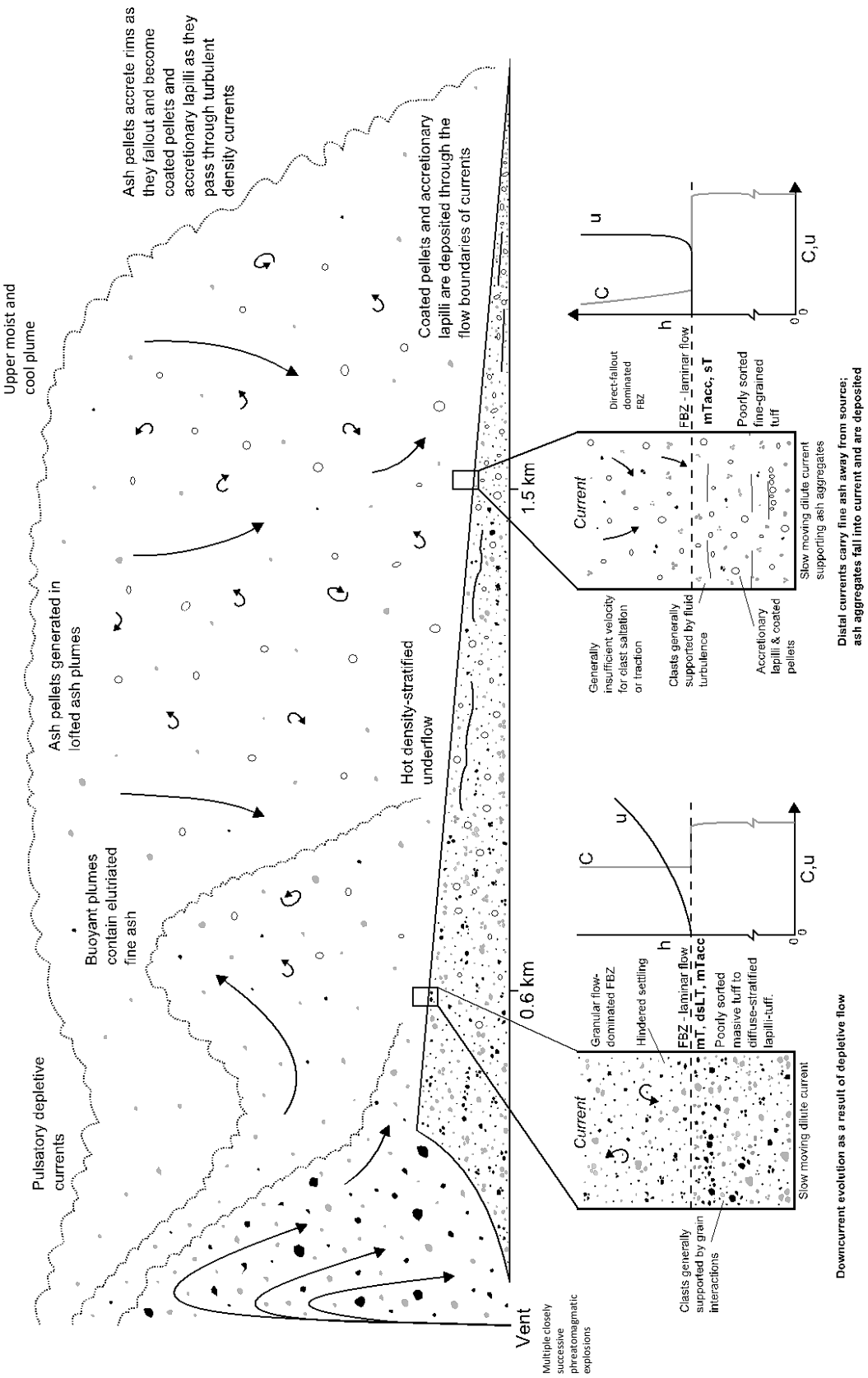

Figure 5.6 *Illustration showing the lateral downcurrent lithofacies changes inferred to have occurred in the single-surge, depletive pyroclastic density currents that deposited LFT 5. Fully dilute currents show a transition from mainly granular flow-dominated flow boundaries in proximal regions to fall-out- to traction-dominated flow boundaries in medial and distal regions. Ash aggregates formed in the lofted ash plumes and accreted rims as they passed through the successive density currents. Flow boundary illustrations modified from Branney and Kokelaar (2002).*

Chapter 6: Discussion

6.1 Eruption Dynamics

6.1.1 Tuff Ring and Maar Elements

Caldera del Rey has previous designations of both a maar (Paradas and Fernandez, 1984; Fuster et al., 1994; Martin and Nemeth, 2004) and a tuff ring (Dávila Harris, 2009). Tuff rings, by definition, are built above the pre-existing surface, with typically low-relief crater rims (Cas and Wright, 1987; Reading, 1996) (Figure 1.1). They are formed by explosive eruptions at or near the surface with typically shallow diatremes (Ross et al., 2017). Conversely, maars develop deep craters, that are situated below the pre-existing ground surface (Lorenz, 1973; Vespermann and Schmincke, 2000) and contain a high abundance of accidental lithic fragments that originated from the conduit and underling aquifer (Lorenz, 1986; Ross et al., 2017).

Caldera del Rey has elements of both tuff rings and maars. The dominance of one over the other alternates throughout the eruptions that produced Caldera del Rey. The evidence supporting a tuff ring interpretation is that the crater rims are predominantly built from material that was produced by the Caldera del Rey eruption and they sit above pre-existing ground surface.

The evidence supporting a maar interpretation includes: (i) the great depth of the northern crater, up to 100 m, is more typical of maar volcanoes. This value may in fact be an underestimate, given that the crater is filled with post-eruptive sediments and the actual depth of the crater could be much greater than this; (ii) the high abundance of lithic fragments is suggestive of a deep diatreme excavating into the country rock. Therefore, it is inferred that Caldera del Rey represents a hybrid model of the two transitional components (see following section).

6.1.2 Phreatomagmatic Phases

Phreatomagmatism is the dominant eruptive style at Caldera del Rey, producing Members B, D and E with the following features (Ross et al., 2017): (i) abundant lithic-fragments that signify efficient fragmentation of the country rock (Figure 3.25); (ii) the presence of abundant ash aggregates that indicate high amounts of water in the eruption column (Van Eaton et al., 2012, 2015; Mueller et al., 2016); (iii) bomb sags and soft-sediment deformation indicated water-rich deposits; (iv) dense and poorly vesicular juvenile clasts (Figure 3.26).

However, the Caldera del Rey deposits show changes in the degree of phreatomagmatic fragmentation. The transition from thick pumice fall deposits from quasi-subplinian eruption columns (Members A and C) to multiple closely spaced, pulsatory pyroclastic density currents that developed from semi-constant fountaining (Members B, D and E) is inferred to represent the downward migration of the eruption loci within a growing diatremes over time, resulting in an increased water content and vent widening (Kokelaar, 1986).

Furthermore, the units within Members B and D show abrupt vertical changes in the degree of fragmentation and the processes that produced them, suggesting rapid variations in the water:magma ratio (White and Ross, 2011; Austin-Erikson et al., 2011; Ross et al., 2017). Many of the deposits were produced by high levels of fragmentation during wet phreatomagmatic eruptions. However, some coarser-grained deposits contain large pumice clasts, and discontinuous pumice fall deposits, that likely resulted from drier phreatomagmatic eruptions (Zimanowski et al., 2015).

Alternations between phreatomagmatic and magmatic eruptions have been inferred at tuff rings and maars elsewhere (Lorenz, 1986; White and Ross, 2011). Rapid fluctuations between wetter and drier phases, evidenced by changes in the degree of phreatomagmatic fragmentation and the abundance of lithic fragments, are common (e.g. Ukinrek, Alaska, Self et al., 1980; Crater Hill, New Zealand, Houghton et al., 1996; Tepexitl, Mexico, Austin-Erikson et al., 2008, 2011).

Alternations in the water:magma ratio are dominantly controlled by the availability of groundwater. Drier phreatomagmatic deposits may represent a periods of groundwater depletion and temporary drying out of the aquifer (e.g. Lorenz, 1986). Periodic increases in mass flux can exert a strong control over the eruption style in phreatomagmatic eruptions (Houghton and Nairn, 1991; Houghton et al., 1996), and could have led to a decreased water:magma ratio, resulting in incomplete phreatomagmatic fragmentation (Brown et al., 2007). This is most feasible for the deposits of Member D that marks the climactic phase.

6.1.3 Waxing and Waning

Variations in the degree of phreatomagmatic fragmentation and runout distances indicates that the eruption intensity has undergone a waxing and waning evolution that is particularly evident in the phreatomagmatic beds. Similar evolutions are recorded in other tuff rings (e.g. Glaramara tuff ring, Brown et al., 2007). The units of Member B contained fine-grained beds produced by weak phreatomagmatic eruptions. These were predominantly deposited from currents with traction-dominated flow-boundaries and contained abundant ash aggregates.

As the eruption intensity waxed to its climax in Member D, PDCs were generated that were sufficiently more competent and able to transport lithic lapilli to greater distances. The waxing resulted in a progradation of facies away from the vent. Many of the deposits of Member D reflect a period of highly efficient mixing and heat exchange between the magma and water, with no excessive quenching. This added power in the fountain and currents accounts for the greater runout distances (Brown et al., 2007).

The eruption waning is evident in Member E with progressively weaker phreatomagmatic explosions. The deposits of Member E were produced by pyroclastic density currents with traction-dominated flow-boundary zones. The abundance of coated pellet-rich beds indicates prolonged pauses, possibly up to minutes, between currents that allowed the ash aggregates to settle (Brown et al., 2007). The short runout distances of these deposits is reflective of the weaker phreatomagmatic explosions.

6.2 Comparison with Felsic Tuff Rings and Maars

The Caldera del Rey volcano exhibits similarities with other silicic tuff rings, such as morphology, crater dimensions, ejecta ring structure, dominant lithofacies and inferred eruptive processes (e.g. Hoya de Estrada, Mexico, Cano-Cruz and Carrasco-Nunez, 2008, 2011; Tepexitl, Mexico, Austin-Erikson et al., 2011; Wau, Papua New Guinea, Sillitoe et al., 1984; Glaramara tuff ring, Brown et al., 2007; Ukinrek, Alaska, Self et al., 1980; Crater Hill, New Zealand, Houghton et al., 1996).

6.2.1 Pyroclastic Density Currents

The importance of dilute PDCs (base-surges) in the tephra ring deposits of hydrovolcanoes has been recognised since the seminal work of Moore et al. (1966) and Fisher and Waters (1970). The deposits from these dilute currents are found in great abundance at Caldera del Rey. Additionally, deposits from more concentrated PDCs are also observed at Caldera del Rey and elsewhere (e.g. White, 1991). It is, in fact, common for ejecta ring deposits to show deposition from both fully-dilute and granular fluid-based currents that may change from one to the other (Brown et al., 2007). Such transitions from from thick, structureless, and block-rich beds in proximal locations to well-developed crossbedding in medial locations and thin distal planar beds (Figure 5.3) are observed in deposits of Caldera del Rey and other tuff rings and maars (e.g. e.g. Yokoyama and Tokunaga, 1978; Sohn and Chough, 1989; White, 1991; Colella and Hiscott, 1997; Vasquez and Ort, 2006; Brown et al., 2007). This is because the currents are single-surge, depletive and as they decelerated away from the vent, they lost capacity and competence (Brown et al., 2007).

6.2.2 Late Stage Evolution

Silicic tuff rings and maars often show a late stage evolution towards lower water content phreatomagmatic eruptions, magmatic explosive eruptions and/or lava dome formation (e.g. Hoya de Estrada, Mexico, Cano-Cruz & Carrasco-Nunez, 2008; Tepexitl, Mexico, Austin-Erikson et al., 2011; Wau, Papua New Guinea, Sillitoe et al., 1984). The character of many of the upper parts of ejecta rings show a reduction in the number of

ballistic projectiles and impact sags, and lack fine fragmentation and soft-sediment deformation (Ross et al., 2017). This is interpreted as reflecting eruptions occurring in an exhausted aquifer or increased eruptive rates (Austin-Erickson et al., 2008, 2011; Brown et al., 2007).

Caldera del Rey differs from this model significantly. Whilst Member D shows alternations in the degree of phreatomagmatic fragmentation, Member E contrasts this model, with increased water content phreatomagmatic eruptions in the latter stages that have strongly modified what would normally be the dome forming stage (Figure 3.19). The setting of Caldera del Rey on Tenerife's southern coastline is suggestive that seawater incursion may have had a strong control on groundwater recharge (Elliot et al., 2015). This differentiates Caldera del Rey from other tuff rings where eruptions occur within unconnected aquifers and through surface water, which are more likely to become exhausted and therefore evolve to lower water content eruptions (Lorenz, 1986).

6.3 Ash Aggregates

There is no general pattern to the ash aggregates found in the Caldera del Rey formation and the deposits generally do not conform to the structure of other larger ignimbrites on Tenerife (e.g. Brown et al., 2010). Accretionary lapilli are variably distributed and matrix-supported throughout many of the tuff and lapilli-tuff deposits (Figure 3.5B). Thin beds of coated ash pellets are occasionally interbedded (Figure 3.5A).

Five beds, particularly found in Member D, show a complete vertical couplet sequence comprising a basal layer of matrix-supported accretionary lapilli in the upper parts that, with height, become smaller, closer-spaced, and grade up into coated ash pellets and finally into framework-supported ash pellets (Figure 3.5C). This sequence is present in many of the large ignimbrites on Tenerife (e.g. Adeje Formation, Dávila Harris, 2009; Poris ignimbrite, Brown et al., 2010) and elsewhere (Van Eaton et al., 2012). This records the formation of ash pellets in the upper levels of pyroclastic density currents that accrete rims and are deposited as accretionary lapilli through the flow-boundary zones of density currents. As the current begins to dissipate, coated pellets form as they fall

through the dusty moist air, and finally ash pellets fall through the clean air (Brown et al., 2010).

The variations from this couplet sequence most likely arose from the numerous, rapidly successive, short-lived density currents that tuff rings tend to generate (Moore et al., 1966; Moore, 1967; Sohn, 1996). Additionally, a semi-constant ash plume covering the tuff ring is inferred, similar to an 'Oruanui-like' scenario (Houghton et al., 2015). Therefore, it is likely that the deposition cycles were frequently interrupted by the next currents before the cycle was complete, and full sequences record quiescent intervals (Brown et al., 2010).

Chapter 7: Conclusions

This study has provided new insights into the explosive volcanism that produced the Caldera del Rey volcano, in southern Tenerife. The volcano is interpreted as a hybrid tuff ring constructed during periods of Taalian hydro-explosive activity and subplinian explosivity which produced pumice fall deposits, ash fall deposits and PDC deposits. The stratigraphy originally defined by Dávila Harris (2009) has been redefined and a total of five members (A-E) have been presented alongside a new geological map produced at member scale. Lithofacies associations in each eruption-member have been interpreted in terms of eruptive and emplacement processes.

The data collected over two field seasons reveals two major crater forming phases which exhibit broadly similar vertical lithofacies successions, involving subplinian pumice deposits fall deposits, overlain by massive, cross-stratified and stratified PDC deposits generated by phreatomagmatic explosions. Analysis of the architecture of the phreatomagmatic tuff deposits has revealed how the PDCs evolved and deposited in space and time. The lithofacies record deposition from single-surge, closely successive, depletive currents that decelerated and lost capacity and competence away from the vent. The currents show lateral transitions from granular-fluid based currents to fully dilute currents. The lateral and vertical lithofacies associations are similar to those documented at many modern tuff rings.

Abundant accretionary lapilli and coated ash pellets were generated during the eruptions, likely in ash plumes above the pyroclastic density currents. Many of the ash aggregates fell through the pyroclastic density currents and were deposited from the depositional flow-boundary. However, those found in thin fine-grained tuffs record deposition during quiescent intervals by fallout from these lofted plumes.

Volcanic ballistic projectiles, most common in Members B and D, show characteristics that are typical of phreatomagmatic eruptions. Blocks have a maximum size of 2.5 m in diameter and are found up to 1.6 km from the vent. Blocks as large as 70 cm in diameter

are observed 1 km from the vent. This highlight a potentially fatal hazard close to erupting vents.

The high explosivity of the eruptions is a result of the interaction of magma with groundwater. This is responsible for the creation of two large craters and the partial fragmentation of the underlying aquifer. The lithic fragment population changes upwards through the formation, with lithologies initially close to the surface found in the oldest members, and deeper lithologies more abundant in the youngest members. This reflects the downward migration of the locus of explosivity in the diatreme. The formation shows two repeating transitions from subplinian to phreatomagmatic activity, resulting from a substantial increase of water into the system, likely caused by diatreme growth and fracturing of the aquifer, and an increase in the mass flux rate of the magma. The last stage of the Caldera del Rey eruption involved a substantial ingress of water, resulting in finer-grained phreatomagmatic deposits, relative to the other phreatomagmatic phases.

Chapter 8: Bibliography

Ancochea, E., Fúster, J.M., Ibarrola, E., Cendrero, A., Coello, J., Hernán, F., Cantagrel, J.M., Jamond, C. (1990) Volcanic evolution of the Island of Tenerife (Canary Islands) in the light of new K-Ar data: *Journal of Volcanology and Geothermal Research*, v. 44, p. 231–249.

Ancochea, E., Huertas, M.J., Cantagrel, J.M., Coello, J., Fúster, J.M., Arnaud, N., and Ibarrola, E. (1999) Evolution of the Cañadas edifice and its implications for the origin of the Cañadas Caldera (Tenerife, Canary Islands): *Journal of Volcanology and Geothermal Research*, v. 88, p. 177–199.

Anderton, R. (1985) Clastic facies models and facies analysis. In: *Sedimentology: Recent Developments and Applied Aspects* (Ed. by P. J. Brenchley and B. P. J. Williams), Special Publication of the Geological Society of London, p. 31-47.

Araña, V., and Carracedo, J.L. (1979) Los volcanes de las Islas Canarias. *I Tenerife*. Ed. Rueda, Madrid, p. 481.

Araña, V., and López Ruiz, J. (1974) Volcanismo. Dinámica y Petrología de sus productos. Ed. Istmo, Madrid, p. 481.

Austin-Erickson, A., Büttner, R., Dellino, P., Ort, M.H., Zimanowski, B. (2008) Phreatomagmatic explosions of rhyolitic magma: experimental and field evidence. *J. Geophys. Res*. 113, paper B11201.

Austin-Erickson, A., Ort, M.H., Carrasco-Núñez, G. (2011) Rhyolitic phreatomagmatism explored: Tepexitl tuff ring (Eastern Mexican Volcanic Belt). *J. Volcanol. Geotherm. Res*. 201, p. 325-341.

Baumgartner, R., Fontboté, L., Spikings, R., Ovtcharova, M., Schaltegger, U., Schneider, J., Page, L., Gutjahr, M. (2009) Bracketing the age of magmatic-hydrothermal activity at the Cerro de Pasco epithermal polymetallic deposit, central Peru: a U-Pb and 40Ar/39Ar study. Econ. *Geol*. 104, p. 479-504.

Baumgartner, R., Fontboté, L., Vennemann, T. (2008) Mineral zoning and geochemistry of epithermal polymetallic Zn-Pb-Ag-Cu-Bi mineralization at Cerro de Pasco, Peru. Econ*. Geol*. 103, p. 493-537.

Bonadonna, C. and Costa, A. (2012) Estimating the volume of tephra deposits: a new simple strategy. Geology 40(5), p. 415–418

Bonadonna, C. and Houghton, B. (2005) Total grain-size distribution and volume of tephra-fall deposits. Bull Volcanol 67, p. 441–456

Branney, M.J. and Kokelaar, P. (2002) Sedimentation of ignimbrites from pyroclastic density currents: Special Publication of the Geological Society, London.

Brooker, M. (1991) Geology, alteration and mineralization of the Mount Rawdon diatreme-hosted gold deposit. MSc thesis, James Cook University of North Queensland, Australia,180 p.

Brooker, M., Jaireth, S. (1995) Mount Rawdon, Southeast Queensland, Australia; a diatreme-hosted gold-silver deposit. Econ. *Geol*. 90, p. 1799-1817.

Brooker, M.R., Houghton, B.F., Wilson, C.J.N. and Gamble, J.A. (1993) Pyroclastic phases of a rhyolitic dome-building eruption: Puketarata tuff ring, Taupo Volcanic Zone, New Zealand. *Bull. Volcanol*., 55, p. 395–406.

Brown, R., Branney, M., Maher, C. and Davila-Harris, P. (2010) Origin of accretionary lapilli within ground-hugging density currents: Evidence from pyroclastic couplets on Tenerife. *GSA Bulletin*, 122(1-2), p .305-320.

Brown, R.J. (2001) The eruption histories and depositional mechanisms of the Poris Ignimbrite of Tenerife and the Glaramara tuff of the English Lake District. PhD Thesis, University of Leicester, England, p. 171 (unpub.).

Brown, R.J., Barry, T.L., Branney, M.J., Pringle, M.S., Bryan, S.E. (2003) The Quaternary pyroclastic succession of southern Tenerife, Canary Islands: explosive eruptions, related caldera subsidence and sector collapse. *Geol Mag* 140, p. 265–288.

Brown, R.J., Kokelaar, B.P., Branney, M.J. (2007) Widespread transport of pyroclastic density currents from a large silicic tuff ring: the Glaramara tuff, Scafell caldera, English Lake District, UK. *Sedimentology*, 54, p. 1163–1189.

Bryan, S.E., Martí, J., Cas, R.A.F. (1998). Stratigraphy of the Bandas del Sur Formation: an extracaldera record of Quaternary phonolitic explosive volcanism from the Las Cañadas edifice, Tenerife (Canary Islands). *Geological Magazine,* 135, p. 605–636.

Buchel, G. and Lorenz, V. (1993) Syn- and post-eruptive mechanism of the alaskan Ukinrek maars in 1977. In: Negendank JFW, Zolitschka B (eds) Paleolimnology of European Maar Lakes, Lecture Notes in Earth Sciences 49, p. 15-60.

Bursik, M. and Sieh, K. (2013) Digital database of the Holocene Tephras of the Mono-Inyo Craters, California. U.S. Geological Survey Data Series 758.

Büttner, R., Dellino, P., La Volpe, L., Lorenz, V., Zimanowski, B. (2002) Thermohydraulic explosions in phreatomagmatic eruptions as evidenced by the comparison between pyroclasts and products from Molten Fuel Coolant Interaction experiments. *J. Geophys. Res*. 107 (B11), p. 2277–2290.

Büttner, R., Dellino, P., Zimanowski, B. (1999) Identifying modes of magma/water interaction from the surface features of ash particles. *Nature,* 401, p. 688–690.

Cano-Cruz, M., Carrasco-Núñez, G. (2008) Evolution of a rhyolitic explosion crater (maar): Hoya de Estrada, Valle de Santiago volcanic field, Guanajuato, Mexico. *Revista Mexicana de Ciencias Geologicas*, 25, p. 549-564.

Carey, s. and Sigurdsson, H. (1982) Influence of particle aggregation on deposition of distal tephra from the May 18, 1980, eruption of Mount St. Helens volcano. J Geophys Res Solid Earth (1978– 2012) 87(B8), p. 7061–7072

Carey, S. and Sigurdsson, H. (1987) Temporal variations in column height and magma discharge rate during the 79Ad eruption of Vesuvius. *Geol Soc Am Bull*, 99, p. 303–314.

Carracedo, J.C., Rodriguez Badiola, E., Guillou, H., Paterne, M., Scaillet, S., Pe.rez Torrado, F. J., Paris, R., Fra-Paleo, U. & Hansen, A. (2007). Eruptive and structural history of Teide volcano and rift zones of Tenerife, Canary Islands. *Geological Society of America Bulletin,* 119, p. 1027-1051.

Carracedo, J.C. (1999) Growth, structure, instability and collapse of Canarian volcanoes and comparisons with Hawaiian volcanoes: *Journal of Volcanology and Geothermal Research Special Issue*, v. 94, p. 1–19.

Carracedo, J.C., Day, S., Guillou, H., Rodríguez Badiola, E., Canas, J.A., and Pérez Torrado, F.J. (1998) Hotspot volcanism close to a passive continental margin: The Canary Islands. *Geological Magazine*, v. 135, p. 591–604.

Carrasco-Núñez, G. and Ort, M. (2012) Rhyolitic and basaltic maar volcanoes, a perspective from Mexican volcanism [extended abstract]. Forth International Maar Conference, Auckland, New Zealand, Abstract volume, p. 21-22.

Carrasco-Núñez, G., Ort, M., Romero, C. (2007) Evolution and hydrological conditions of a maar volcano (Atexcac crater, Eastern Mexico). *Journal of Volcanology and Geothermal Research*, 159, p. 179-197.

Cas, R.A.F., Wright, J.V. (1987) Volcanic successions, modern and ancient. Allen & Unwin, London, p. 528.

Cashman, K. (2004) Volatile Controls on Magma Ascent and Eruption. In: Haweksworth, C. and Sparks, R, The State of the Planet: Frontiers and Challenges in Geophysics.

Cashman, K., Rust, A. (2016) Volcanic Ash: Generation and Spatial Variations. In: Mackie, S., Cashman, K., Ricketts, H., Rust, A., Watson, M., Volcanic Ash, *Elsevier*, p. 5-22.

Cashman, K.V. and Mangan, M.T. (1994) Physical Aspects of Magmatic Degassing II. Constraints on Vesiculation Processes from Textural Studies of Eruptive Products. In: Carroll, M.R. and Holloway, J.R., Eds., Volatiles in Magmas, Mineralogical Society of America, Chantilly, p. 447-478.

Cashman, K.V. and Scheu, B. (2015) Magmatic fragmentation. In: Sigurdsson H, Houghton B, McNutt SR, Rymer H, Stix J (eds) Encyclopedia of Volcanoes, Second edition. Academic Press, London, p. 459-471.

Chough, S.K. and Sohn, Y.K. (1990) Depositional mechanics and sequences of base surges, Songaksan tuff ring, Cheju Island, Korea. *Sedimentology*, 37, p. 1115–1135.

Cioni, R., Pistolesi, M., Rosi, M. (2015) Plinain and Subplinian Eruptions. In: Sigurdsson H, Houghton B, McNutt SR, Rymer H, Stix J (eds) Encyclopedia of Volcanoes, Second edition. Academic Press, London, p. 518-536.

Colella, A. and Hiscott, R.N. (1997) Pyroclastic surges of the Pleistocene Monte Guardia sequence (Lipari Island, Italy): depositional process. Sedimentology, 44, 47–66.

Dávila Harris, P. (2009) Explosive ocean-island volcanism: the 1.8–0.7 Ma explosive eruption history of Cañadas volcano recorded by the pyroclastic successions around Adeje and Abona, southern Tenerife, Canary Islands [unpublished Ph.D. Thesis]: Leicester, University of Leicester, UK, p. 311.

De Novellis, V. and Luongo, G. (2006) Chapter 5 ballistics shower during Plinian scenario at Vesuvius. In: Dobran, F. Vesuvius.

de' Michieli Vitturi, M., Neri, A., Esposti Ongaro, T., Lo Savio, S., Boschi, E. (2010), Lagrangian modeling of large volcanic particles: Application to Vulcanian explosions, J. Geophys. Res., 115, B08206.

De Rita, D., Giordano, G., Esposito, A., Fabbri, M., Rodani, S. (2002) Large volume phreatomagmatic ignimbrites from the Colli Albani volcano (Middle Pleistocene, Italy). *J. Volcanol. Geotherm. Res.,* 118, p. 77–98.

Dellino, P., Isaia, R., La Volpe, L., Orsi, G. (2004) Interaction between particles transported by fallout and surge in the deposits of Agnano-Monte Spina eruption (Campi Flegrei, southern Italy). *J. Volcanol. Geotherm. Res*. 133, p. 193–210.

Elliot, H.A.L., Gernon, T.M., Roberts, S., Hewson, C. (2015) Basaltic maar-diatreme volcanism in the Lower Carboniferous of the Limerick Basin (SW Ireland). *Bull Volcanol,* 77: 37.

Engwell, S.L., Aspinall, W.P., Sparks, R.S.J. (2015) An objective method for the production of isopach maps and implications for the estimation of tephra deposit volumes and their uncertainties. *Bull Volcanol* 77: 61.

Fisher, R.V. and Schmincke, H.-U. (1984) Pyroclastic Rocks: Springer-Verlag, Berlin, p. 472.

Fisher, R.V. and Waters, A.C. (1970) Base surge forms in maar volcanoes. *Am. J. Sci*. 268, p. 157-180.

Fowler, A.C., Scheu, B., Lee, W.T., McGuinness, M.J. (2010) A theoretical model of the explosive fragmentation of vesicular magma. *Proc. R. Soc*. A 466, p. 731-752.

Francis, P.W. and Oppenheimer, C. (2004) Volcanoes. Oxford University Press, Oxford, UK.

Freda, C., Gaeta, M., Karner, D.B., Marra, F., Renne, P., Taddeucci, J., Scarlato, P., Christensen, J.N., Dallai, L. (2005) Eruptive history and petrologic evolution of the Albano multiple maar (Alban Hills, Central Italy). *Bull. Volcanol.*, 68, p. 567–591.

Fúster, J.M., Araña, V., Brandle, J.L., Navarro, M., Alonso, U., and Aparicio, A. (1968) Geología y volcanología de las Islas Canarias: Tenerife: Madrid, Instituta "Lucas Mallada", Consejo Superior de Investigaciones Cientificas, p. 218.

Fúster, J.M., Ibarrola, E., Snelling, N.J., Cantagrel, J.M., Huertas, M.J., Coello, J., Ancochea, E. (1994) Cronología K – Ar de la Formación Cañadas en el sector suroeste de Tenerife: Implicaciones de los episodios piroclásticos en la evolución volcánica. *Bol. R. Soc. Esp. Hist. Nat. (Sec. Geol.)*, 89, p. 25–41.

G. Kilgour, Manville, V., Della Pasqua, F., Graettinger, A., Hodgson, K.A., Jolly, G.E. (2010) The 25 September 2007 eruption of Mount Ruapehu, New Zealand: Directed ballistics, surtseyan jets, and ice-slurry lahars. *Journal of Volcanology and Geothermal Research*, V 191, Issues 1–2, p. 1-14.

Garcia Hernandez, J.E., Notario Del Pino, J.S., Gonzalez Martin, M.M., Hernan Regura, F., Rodriquez Losada, J.A. (1993) Zeolites in pyroclastic deposits in southeast Tenerife (Canary Islands). *Clays and Clay Minerals*, V 41, No. 5, p. 521-526.

Gardner, J.E., Thomas, R.M.E., Jaupart, C., Tait, S. (1996) Fragmentation of magma during Plinian volcanic eruptions. *Bull Volcanol*, 58, p. 144–162.

Hausen, H. (1956) Contributions to the Geology of Tenerife (Canary Islands). *Soc. Sci. Fennica comment. Phys-Math*, 18-1, p. 1-271.

Heiken, G.H. and Wohletz, K. (1987) Tephra deposits associated with silicic domes and lava flows. *Geol. Soc. Am. Spec.* Pap. 212, p. 55–76.

Hernández-Pacheco, E., Hernández-Pacheco, F., Alía, M., Vidal Box, C., Guinea, E. (1949) El Sahara Español, studio geológico, geográfico y botánico. *C.S.I.C., Instituto Estudios Africanos*, Madrid. P. 808.

Hooten, J.A. and Ort, M.H. (2002) Peperite as a record of early stage phreatomagmatic fragmentation processes: an example from the Hopi Buttes Volcanic Field, Navajo Nation, Arizona, USA. *J Volcanol. Geotherm. Res*. 114, p. 95–106.

Houghton, B.F. and Nairn, I.A. (1991) The 1976–1982 Strombolian and phreatomagmatic eruptions of White Island, New Zealand – eruptive and depositional mechanisms at a wet volcano. *Bull. Volcanol*., 54, p. 25–49.

Houghton, B.F. and Smith, R.T., (1993) Recycling of magmatic clasts during explosive eruptions; estimating the true juvenile content of phreatomagmatic volcanic deposits. *Bull. Volcanol*., 55 (6), p. 414–420.

Houghton, B.F. and Wilson, C.J.N. (1989) A vesicularity index for pyroclastic deposits. *Bull Volcanol*, 51, p. 451-462.

Houghton, B.F., Wilson, C.J.N., Rosenberg, M.D., Smith, I.E.M., Parker, R.J. (1996) Mixed deposits of complex magmatic and phreatomagmatic volcanism: an example from Crater Hill, Auckland, New Zealand. *Bull. Volcanol*., 58, p. 59–66.

Houghton, B.F., Wilson, C.J.N., Smith, I.E.M. (1999) Shallow-seated controls on styles of explosive basaltic volcanism: a case study from New Zealand. *J. Volcanol. Geotherm. Res.,* 91, p. 97–120.

Houghton, B.F., Wilson, C.J.N., Weaver, S.D. (1987) The Opo Bay tuff cone, Mayor Island; interaction between rising gas-poor pantelleritic magma and external water. *NZ Geol. Surv.,* 18, p. 79–85.

Houhgton, B., White, J.D.L., Van Eaton, A.R. (2015) Phreatomagmatic and Related Eruption Styles. In: Sigurdsson H, Houghton B, McNutt SR, Rymer H, Stix J (eds) Encyclopedia of Volcanoes, Second edition. Academic Press, London, p. 537-552.

Huertas, M.J., Arnaud, N.O., Ancochea, E., Cantagrel, J.M., Fúster, J.M. (2002) 40Ar/39Ar stratigraphy of pyroclastic units from the Cañadas Volcanic Edifice (Tenerife, Canary Islands) and their bearing on the structural evolution. *J Volcanol Geotherm Res,* 115, p. 36-351.

James, M.R., Gilbert, J.S. and Lane, S.J., (2002) Experimental investigation of volcanic particle aggregation in the absence of a liquid phase. *Journal of Geophysical Research: Solid Earth*, *107*(B9).

Kienle, J., Kyle, P.R., Self, S., Motyka, R.J. and Lorenz, V. (1980) Ukinrek maars, Alaska, 1. April 1977 eruption sequence, petrology and tectonic setting. *J. Volcanol. Geotherm. Res.*, 7, p. 11–37.

Klawonn, M., Houghton, B.F., Swanson, D.A., Fagents, S.A., Wessel, P., Wolfe, C.J. (2014) Constraining explosive volcanism: Subjective choices during estimates of eruption magnitude. *Bull Volcanol* 76(2):1–6.

Klug, C., Cashman, K., Bacon, C. (2002) Structure and physical characteristics of pumice from the climactic eruption of Mount Mazama (Crater Lake), Oregon. *Bull Volcanol,* 64, p. 486.

Kokelaar, B.P. (1983) The mechanism of Surtseyan volcanism*. J. Geolo. Soc. London,* 140, p. 939-944.

Kokelaar, B.P. (1986) Magma-water interactions in subaqueous and emergent basaltic volcanism. *Bull. Volcanol.*, 48, p. 275–289.

López-Rojas, M. and Carrasco-Núñez, G. (2015) Depositional facies and migration of the eruptive loci for Atexcac axalapazco (Central Mexico): Implications for the morphology of the crater. *Rev. Mex. Cienc. Geol.*, 32(3), p. 377–394.

Lorenz, V. and Kurszlaukis, S. (2007) Root zone processes in the phreatomagmatic pipe emplacement model and consequences for the evolution of maar-diatreme volcanoes. *J. Volcanol. Geotherm. Res.,* 159, p. 4-32.

Le Bas, M.J., Le Maitre, Streckeisen, A., Zanettin, B. (1986) A chemical classification of volcanic rocks based on the total alkali-silica diagram. *Journal of Petrology*, 27, p. 745-750.

Lorenz, V. (1970) Some aspects of the eruption mechanism of the Big Hole maar, Central Oregon. *Geol. Soc. Am. Bull.*, 81, p. 1823–1830.

Lorenz, V. (1973) On the formation of maars. *Bull. Volc*., 37, p. 183-204.

Lorenz, V. (1986) On the growth of maars and diatremes and its relevance to the formation of tuff rings. Bull. Volc. 48:265-274.

Martí, J., Mitjavila, J., Araña, V. (1994) Stratigraphy, structure and geochronology of the Las Cañadas caldera (Tenerife, Canary Islands). *Geological Magazine,* 131, p. 715–27.

Martin, U. and Nemeth, K. (2004) Quaternary phreatomagmatic volcanoes of Southern Tenerife, Spain: Montana Pelada tuff ring and Caldera del Rey maar. In: Second International Maar Conference, Hungary-Slovakia-Germany, Abstract volume, 203 p. 74.75.

Mastin, L.G. (2007) Generation of fine hydromagmatic ash by growth and disintegration of glassy rinds. *J. Geophys. Res*., 112, B02203.

Mastrolorenzo, G. (1994) Averno tuff ring in Campi Flegrei (south Italy). *Bull. Volcanol.*, 56, p. 561–572.

Mattsson, H.B., Höskuldsson, A., Hand, S. (2005) Crustal xenoliths in the 6220 BP Saefell tuff-cone, south Iceland: Evidence for a deep, diatreme-forming, Surtseyan eruption. *Journal of volcanology and geothermal research* 145, no. 3-4 (2005), p. 234-248.

McPhie, J. (1986) Primary and redeposited facies from a largemagnitude rhyolitic, phreatomagmatic eruption: Cana Creek tuff, Late Carboniferous, Australia. *J. Volcanol. Geotherm. Res.*, 28, p. 319–350.

Moore, J. G., Nakamura, K., Alcaraz., A. (1966) The 1965 eruption of Taal Volcano. *Science,* 151, p. 955–960.

Moore, J.G. (1967) Base surge in recent volcanic eruptions: *Bulletin Volcanologique*, v. 30, p. 337-363.

Moore, J.G. (1985) Structure and eruptive mechanism at Surtsey volcano, Iceland. *Geol. Mag.,* 122, p. 649-661.

Morrissey, M., Zimanowski, B., Wohletz, K.H., Büttner, R. (2000) Phreatomagmatic fragmentation. In: Sigurdsson, H. (Ed.), Encyclopedia of Volcanoes. Academic Press, San Diego, p. 431–446.

Mueller, S.B., Kueppers, U., Ayris, P.M., Jacob, M., Dingwell, D.B. (2016) Experimental volcanic ash aggregation: Internal structuring of accretionary lapilli and the role of liquid bonding. *Earth and Planetary Science Letters*, *433*, p. 232-240.

Nelson, B.K., Carracedo, J.C., Badiola, E.R., Hamilton, A., Guetschow, H. (2005) Spatial and temporal isotopic gradients in the Western Canary Islands. *American Geophysical Union Fall Meeting Abstracts*, p. 1471.

Németh, K. and Kereszturi, G. (2015) Monogenetic volcanism: personal views and discussion. *International Journal of Earth Sciences*, 104, p. 2131-2146.

Paradas Herrero, A. and Fernandez Santín, S. (1984) Estudio vulcanológico y geoquímico del maar de la Caldera del Rey, Tenerife (Canarias). *Estudios Geológicos,* 40, 285-313.

Patel, A., Manga, M., Carey, R.J., Degruyter, W. (2013) Effects of thermal quenching on mechanical properties of pyroclasts. *Journal of Volcanology and Geothermal Research*, 258, p. 24-30.

Pyle, D.M. (1989) The thickness, volume and grain size of tephra fall deposits. *Bull. Volcanol*., 51, p. 1-15.

Reading, H.G. (1996) Sedimentary Environments: Process, Facies and Stratigraphy (3rd edition): Oxford: Blackwell Science.

Rohlof, K.J. (1969) Analysis of the exterior ballistics of block ejecta at Nanwaksjiak Crater, Nunivak Island, Alaska. M.S. Thesis, Air Force Institute of Technology, Wright-Patterson AFB, Ohio (unpublished).

Ross, P.-S. and White, J.D.L. (2012) Quantification of vesicle characteristics in some diatreme-filling deposits, and the explosivity levels of magma-water interactions within diatremes. *J. Volcanol. Geotherm. Res.,* 245-246, p. 55-67.

Ross, P.-S., Carrasco-Núñez, G., Hayman, P. (2017) Felsic maar-diatreme volcanoes: a review. *Bull. Volc.,* 79, Article 20, p. 1-33.

Ross., P.-S., Delpit., S., Haller., MJ, Németh K, Corbella H (2011) Influence of the substrate on maar-diatreme volcanoes – an example of a mixed setting from the Pali Aike volcanic field, Argentina. *J. Volcanol. Geotherm. Res.,* 201, p. 253-271.

Rust, A.C., Cashman, K.V. (2011) Permeability controls on expansion and size distributions of pyroclasts. *J. Geophys. Res.,* p. 116.

Rust, A.C., Cashman, K.V., Wallace, P.J. (2004). Magma degassing buffered by vapor flow through brecciated conduit margins. *Geology,* 32 (4), p. 349–352.

Schumacher, R. and Schmincke, H.U. (1991) Internal structure and occurrence of accretionary lapilli—a case study at Laacher See Volcano. *Bulletin of Volcanology*, *53*(8), p. 612-634.

Schumacher, R. and Schmincke, H.U. (1995) Models for the origin of accretionary lapilli. *Bulletin of Volcanology*, *56*(8), p. 626-639.

Seifert, R., Malfait, W.J., Petitgirard, S., Sanchez-Valle, C. (2013) Density of phonolitic magmas and time scales of crystal fractionation in magma chambers. *Elsevier*, Earth and Planetary Science Letters, 381, p. 12-20.

Self, S., Kienle, J., Huot., J.-P. (1980) Ukinrek Maars, Alaska, II. Deposits and formation of the 1977 craters. *J. Volcanol. Geotherm. Res.*, 7, p. 39–65.

Sheridan, M.F. and Updike, R.G. (1975) Sugar Loaf Mountain Tephra - A Pleistocene rhyolitic deposit of base surge origin. *Geol. Soc. Am. Bull.*, 86, p. 571–581.

Sheridan, M.F., Wohletz, K.H., Dehn, J. (1987) Discrimination of grain-size subpopulations in pyroclastic deposits. Geology 15 (4), 367–370.

Sillitoe RH, Baker EM, Brook WA (1984) Gold deposits and hydrothermal eruption breccias associated with a maar volcano at Wau, Papua New Guinea. *Econ. Geol.,* 79, p. 638-655.

Sillitoe, R.H., Grauberger, G.L., Elliott, J.E. (1985) A diatreme-hosted gold deposit at Montana Tunnels, Montana. *Econ. Geol*., 80, p. 1707-1721.

Sohn, Y.K. (1996) Hydrovolcanic processes forming basaltic tuff rings and cones on Cheju Island, Korea. *Geol. Soc. Am. Bull.*, 108, p. 1199–1211.

Sohn, Y.K. and Chough, S.K. (1989) Depositional processes of the Suwolbong tuff ring, Cheju Island (Korea). *Sedimentology*, 40, p. 837–855.

Sottili, G., Palladino, D.M., Gaeta, M., Masotta, M. (2012), Origins and energetics of maar volcanoes: Examples from the ultrapotassic sabatini volcanic district (roman province, central Italy), *Bull. Volcanol.*, 74(1), p. 163–186.

Sparks, R., Meyer, P., Sigurdsson, H. (1980) Density variation amongst mid-ocean ridge basalts: Implications for magma mixing and the scarcity of primitive lavas. *Earth and Planetary Science Letters*, 46(3), p. 419-430.

Suthren, R.J. (1977) Volcanic and sedimentary facies of part of the Borrowdale Volcanic Group, Cumbria: Unpubl. Ph. D. thesis, University of Keele, U. K.

Taddeucci, J., Alatorre-Ibargüengoitia, M.A., Cruz-Vázquez, O., Del Bello, E., Scarlato, P., Ricci, T. (2017) In-flight dynamics of volcanic ballistic projectiles. *Rev. Geophys.,* 55, p. 675–718.

Thorarinsson, S. (1954) The eruptions of Hekla 1947 - 1948. In: The tephra fall from Hekla. Vis Islendinga, Reykjavik, 3(2):68.

Thorarinsson, S. (1967) Surtsey. The New Island in the North Atlantic. *The Viking Press*, New York, p. 47.

Tuffen, H., Dingwell, D.B., Pinkerton, H. (2003) Repeated fracture and healing of silicic magma generate flow banding and earthquakes? *Geology,* 31, p. 1089-1092.

Valentine, G.A., White, J.D.L. (2012) Revised conceptual model for maar-diatremes: subsurface processes, energetics, and eruptive products. *Geology*, 40, p. 1111-1114.

Valentine, G.A., White, J.D.L., Ross, P.-S., Graettinger, A.H., Sonder., I. (2017) Updates to Concepts on Phreatomagmatic Maar-Diatremes and Their Pyroclastic Deposits. *Front. Earth Sci*., 5, p. 68.

Van Eaton, A.R., Mastin, L.G., Herzog, M., Schwaiger, H.F., Schneider, D.J., Wallace, K.L. and Clarke, A.B. (2015) Hail formation triggers rapid ash aggregation in volcanic plumes. *Nature communications*, *6*.

Van Eaton, A.R., Muirhead, J.D., Wilson, C.J. and Cimarelli, C. (2012) Growth of volcanic ash aggregates in the presence of liquid water and ice: an experimental approach. *Bulletin of volcanology*, *74*(9), p. 1963-1984.

Varekamp, J.C. (1993) Some remarks on volcanic vent evolution during plinian eruptions. *Journal of Volcanology and Geothermal Research*, 54, Issues 3–4, p. 309-318.

Vazquez, J.A. and Ort, M.H. (2006) Facies variation of eruption units produced by the passage of single pyroclastic surge currents, Hopi Buttes volcanic field, USA. *J. Volcanol. Geotherm. Res.,* 154, p. 222–236.

Vespermann, D., Schminke, H.-U. (2000) Scoria cones and tuff rings. In: Sigurdsson, H., Houghton, B.F., McNutt, S.R., Rymer,H., Stix, J. (Eds.), Encyclopedia of Volcanoes. Academic Press, San Diego, p. 683-694.

Waitt, R.B., Mastin, L.G., Miller, T. P. (1995) Ballistic showers during crater peak eruptions of Mount Spurr volcano, summer 1992. *USGS Bulletin*, *2139*, p. 89-106.

Walker, G.P.L. (1980) The Taupo Pumice: Product of the most powerful known (ultra-plinian) eruption? *J Volcanol Geotherm Res* 8(1):69–94.

Walker, G.P.L. (1981) Generation and dispersal of fine ash and dust by volcanic eruptions. *Journal of Volcanology and Geothermal Research*, v. 11, p. 81-92.

Walker, G.P.L. (1984) Characteristics of dune-bedded pyroclastic surge bedsets. *J. Volcanol. Geotherm. Res.,* 20, p. 281–296.

Waters, A.C. and Fisher, R.V. (1971) Base surges and their deposits: Capelinhos and Taal volcanoes. J. Geophys. Res., 76, p. 5596–5614.

White, J.D.L. (1991) Maar-diatreme phreatomagmatism at Hopi Buttes, Navajo Nation (Arizona), USA. Bull. Volc. 53:239-258.

White, J.D.L. and Ross, P-S. (2011) Maar-diatreme volcanoes: a review. *J. Volcanol. Geotherm. Res.,* 201, p. 1-29.

White, J.D.L., Schmincke, H.-U. (1999) Phreatomagmatic eruptive and depositional processes during the 1949 eruption on La Palma (Canary Islands). *J. Volcanol. Geotherm. Res.,* 94, p. 283-304.

Williams, G.T., Kennedy, B.M., Wilson, T.M., Fitzgerald, R.H., Tsunematsu, K., Teissier, A. (2017) Buildings vs. ballistics: Quantifying the vulnerability of buildings to volcanic ballistic impacts using field studies and pneumatic cannon experiments. *Journal of Volcanology and Geothermal Research,* 343. p. 171-180.

Wohletz, K.H. and Sheridan, M.F. (1983) Hydrovolcanic explosions II: Evolution of basaltic tuff rings and tuff cones. *Am. J. Sci.*, 283, p. 385–413.

Yamagishi, Hiromitsu, Feebrey, C. (1994) Ballistic ejecta from the 1988–1989 andesitic Vulcanian eruptions of Tokachidake volcano, Japan: morphological features and genesis. *Journal of volcanology and geothermal research* 59, 4, p. 269-278.

Yamamoto, T., Soya, T., Suto, S., Uto, K., Takada, A., Sakaguchi, K. and Ono, K. (1991) The 1989 submarine eruption off eastern Izu Peninsula, Japan: ejecta and eruption mechanisms. *Bull. Volcanol.,* 53, p. 301–308.

Yokoyama, S., Tokunaga, T. (1978) Base-surge deposits of Mukaiyama volcano, Nii-jima, Izu Islands. *Bulletin of the Volcanological Society of Japan*, 23, p. 249-262.

Zimanowski B, Büttner R, Delino P, White JDL, Wohletz K. (2015) Magma-water interaction and phreatomagmatic fragmentation. In: Sigurdsson H, Houghton B, McNutt SR, Rymer H, Stix J (eds) Encyclopedia of Volcanoes, Second edition. Academic Press, London, p. 473-484.

Zimanowski, B. and Buttner, R. (2002) Dynamic mingling of magma and liquefied sediments. *J. Volcanol. Geotherm. Res.,* 114, p. 37-44.

Zimanowski, B. (1998) Phreatomagmatic explosions. In: Freundt, A., Rosi, M. (Eds.), From Magma to Tephra: Developments in Volcanology, 4. *Elsevier*, Amsterdam, p. 25–54.

Zimanowski, B., Büttner, R., Lorenz, V., Häfele, H.-G. (1997) Fragmentation of basaltic melt in the course of explosive volcanism. *J. Geophys. Res.,* 102, p. 803–814.

Zimanowski, B., Fröhlich, G., Lorenz, V. (1991) Quantitative experiments on phreatomagmatic explosions. *J. Volcanol. Geotherm. Res.,* 48, p. 341-358.